2019

Improved System for Fabrication and Characterization of Nanophotonic Devices by Multi-photon Lithography

Rashi Sharma
University of Central Florida

IMPROVED SYSTEM FOR FABRICATION AND CHARACTERIZATION OF NANOPHOTONIC DEVICES BY MULTI-PHOTON LITHOGRAPHY

by

RASHI SHARMA

BSc. Dr. Bhim Rao Ambedkar University 2004

MSc. Dayalbagh Educational Institute 2006

MS. University of Central Florida 2014

A dissertation submitted in the partial fulfillment of the requirements

for the degree of Doctor of Philosophy

in the Department of Chemistry

of the College of Sciences

at the University of Central Florida

Orlando, Florida

Fall Term

2018

Major Professor: Stephen M. Kuebler

ABSTRACT

A new system for multi-photon lithography (MPL) was developed and used to fabricate three-dimensional (3D) structures with higher aspect ratio, better resolution, improved fidelity, and reduced structural distortion relative to a conventional implementation of MPL.

A set of curved waveguides (R_{bend} = 19 μm, and 38 μm) and straight waveguides (length = 50 μm, $R_{bend} = \infty$) were fabricated in an epoxide photopolymer and optically characterized using light having a wavelength in vacuum of λ_0 = 2.94 μm. The optical performance of the waveguides was compared to novel spatially-variant photonic crystals (SVPCs) previously studied in the group. The waveguides were found to guide light with 90% lower efficiency, due to mode leakage. The study provides further evidence that SVPCs operate not through total internal reflection, but rather through self-collimation, as designed.

3D uniform-lattice photonic crystals (ULPCs) were fabricated by MPL using a commercial acrylate photopolymer. The ULPCs were optically characterized at λ_0 = 1.55 μm. A laser beam with adjustable bandwidth was used to measure the self-collimation in the ULPCs. For the low bandwidth beam, vertically polarized light was self-collimated, whereas horizontally polarized light diverged. The transmission efficiency of the ULPCs was also measured as a function of fill factor. The ULPC having a fill factor of 48% exhibited 80% transmission.

An etching process was also developed for non-destructively removing Au/Pd coatings that must be deposited onto structures to image them by scanning electron microscopy. The structural and optical integrity of the samples was found to be maintained despite etching. The sputter-coated sample sustained no structural damage when exposed to the λ_0 = 1.55 μm. However, the metal

coating resulted in diminished transmission efficiency due to the high reflection of the 1.55 μm beam by the metal coating.

To my husband Nishank, I dedicate this dissertation.

In the words of Kabir,

खुल खेलो संसार में, बाँधी ना सके कोय,

जाको राखे साईंयां, मारि ना सके कोय.

Be fearless

ACKNOWLEDGMENT

Eight years ago, when I came to United States, I never imagined I would be writing this acknowledgement. There are no words for me to describe how challenging, inspiring, and fun these seven years in UCF had been for me. However, there were so many incidents when I thought this work is beyond my capability and in those times I got the much needed support, that I was able to achieve my dream of finishing the PhD. First and foremost I want to thank God, for always being there for me, even when I was too busy to worship or visit the temple or celebrate any festivals. I worshiped in the form of hard work and know he understands that.

Nishank, my husband, I have known you for more then 20 years, but in the last 2 years you have supported me and our little family like a rock. I cannot thank you enough for what you have done for me. Thank you, for always motivating me to pursue my dreams, thank you for making me a better version of myself. You have stalled your career, so that we can live as a family and I can fulfill my dreams. I always knew you were the love of my life, and I cannot be happier about having you in my life. Thanking you would not have been complete without introducing our little monster Kabir. Kabir, I never knew I could love someone like this, before you came into my life. Thank you for making me you “mama”.

I am so thankful to my parents, who worked hard all their life and sacrificed so much, to make sure I get a good education. Thank you for teaching me that there is no alternative to hard work. I also want to thank my brother Harish, who has been more than a brother for me through-out my life. No matter what the problem is, I knew I can always rely on him. Thank you for talking to me whenever I had doubts, and thank you for being my oldest friend. Richa and Lori, thank you

for always supportive of my work. Lori, I know one day you will understand what your bhua did for seven years. But, thank you for filling our home with so much cuteness.

My supervisor, Dr. Kuebler and the nanophotonics materials (NPM) were such an important part of my journey here at UCF. Dr. Kuebler, thank you for teaching me everything I know about optics, and making me work outside of my comfort zone. I could not have done without your constant support and motivation. My labmates during my time in NPM group were my support system. Dr. Casey, Dr. Ping, Dr. Chris, Chun, Geng, Pooria, Nick, Hannah. Working with all of you had been so much fun. Chun, thank you for helping me with last minute experiments. Good luck with all your future endeavors.

I made some of my life's best friends during my time here at UCF. Casey, Yuly, Julie and Dom you guys have been amazing. Casey, you are not just my best friend, but also my second advisor. Thank you for teaching me, and helping me with the experiments and proof reading my writing. I could not have done this without you. Yuly, we met on the first day of graduate school, and I am so happy that we started talking right away. You are such a strong woman, and I am so glad to have known you. I wish all the best in life. Julie, you are such a positive personality, and I feel so good after talking to you. Our extra-long lunches with baby talks were sometimes the best parts of my day. Dom, what can I say about you. You are such a brave and amazing person, I wish you climb every mountain you set your mind too, and one day you can cook Indian food like me.

In the end, I want to thank my friends Deepti, Shubhra, Rajan, Dhiraj, Aparna and my darling cousin Bulbul. You guys live so far from me, but thank you for always being there for me.

TABLE OF CONTENTS

LIST OF FIGURES

LIST OF TABLES

LIST OF ABBREVIATIONS

1D	One dimensional
2D	Two dimensional
3D	Three dimensional
AFS	Amplified femtosecond laser
AOM	Acousto optic modulator
BOE	Buffered oxide etch
BS	Beam splitter
CCD	Charge coupled device
Cr	Chromium
DI	Deionized water
dB	Decible
E-beam	Electron beam
EM	Electromagnetic
FFT	Fast-fourier transform
FROG	Frequency –resolved optical grating
FDTD	Finite-difference time domain
FWHM	Full width half maxima

Au	Gold
HPC	High performance computers
IFC	Isofrequency contour
IPA	Isopropyl alcohol
IC	Integrated circuits
IO	Integrated optics
ILs	Ionic liquids
IR	Infrared
KOH	Potassium hydroxide
KI	Potassium iodide
MPL	Multi-photon lithography
MFD	Mode field diameter
mV	Millivolts
MEMS	Micro-electro mechanical system
Nd	Neodymium
NA	Numerical aperture
ND	Neutral density
OPGs	Optical parametric generators

PI	Physik Instrumente
Pd	Palladium
Pt	Platinum
PAGs	Photo-acid generators
PGMEA	Propylene glycol methyl ethyl ether
PD	Photodetector
SVPC	Spatially variant photonic crystals
SEM	Scanning electron microscopy
Si	Silicon
TIR	Total internal reflection
ULPC	Uniform lattice photonic crystals
UV	Ultraviolet
V	Voltage
VCSEL	Vertical-cavity surface emitting laser
YAG	Yttrium aluminum garnet

1. INTRODUCTION

1.1 Optical interconnects

With the current growth in the internet traffic, high performance computers (HPC) like super computers and data performance centers are in more demand right now than ever.[1] The performance of the top 500 computers has increased 10 fold every 4 years.[2] To be able to keep up on this path, future computers will have to be faster with higher bandwidth. One way to achieve higher bandwidth is to incorporate efficient interconnects for faster on-chip and chip-to-chip data transfer. Introduction of photonic components in the electronic circuits helps to overcome the limitations seen in devices with pure electrical circuits.[3] It is important to develop interconnects which are capable of high bandwidth, low optical loss, immunity to crosstalk as well as heat losses. Due to the inherent tendency of photons to interact weakly with each other when travelling through a medium, they are promising candidates to be used in the field of broadband communications and high capacity information storage.[4]

Silicon (Si) plays a major role in the development of high speed devices. But Si undergoes significant data loss due to high capacitance and resistance and because of this modern circuits have come to approach their limits. Optical interconnects, on the other hand, are free from any heat and capacitive losses because they use photons for data transfer. There has been significant progress in the field for chip-to-chip and on-chip optical interconnects.[5-6] To develop optoelectronic devices, which are capable of fast signal processing, we need to use optical interconnects capable of guiding light within the length scale of the wavelength.[7] Other than Si, materials that are currently used to fabricate optoelectronic devices are metals [8], glasses [9], polymers

[4] and composites.[10] There are caveats involved in using these materials, which include bending losses in metal interconnects[11], coupling loss between the Si and optical fibers[12], and crosstalk in waveguides fabricated via polymers.[4] The search for an efficient optical interconnect has been going on for decades.[13] Figure 1 illustrates an example of an inter-chip optical interconnect in which vertical-cavity surface-emitting laser (VCSEL) or photodetector (PD) and electronic integrated circuits (ICs) such as driver and receiver chips are integrated with a polymeric waveguide.[14]

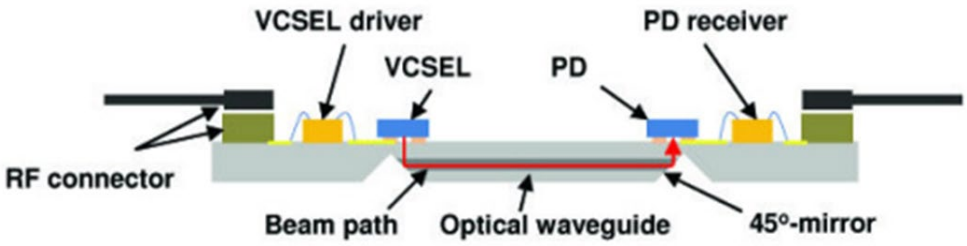

Figure 1. Illustrates an optical interconnection module such as VCSEL driver and PD devices directly integrated with a polymeric waveguide.[14]

Waveguides are one of the most commonly used optical interconnect. The first on-chip optical waveguide was fabricated by integrating an optical fiber with a VCSEL laser. Recent advances in lithography techniques made it possible to fabricate high density waveguides and their on–chip integration with light sources and detectors.[15-16] Waveguides not only offer substantial advantages in data transfer, but they are also used for developing lab-on-a-chip technology by enabling fluidic handling and optical analysis of samples onto a single chip. These integrated sensing devices are opening a new branch of high density biosensors that can provide rapid on-site results.[17]

1.2 Nanophotonic devices

Nanophotonics is a branch of nanoscience that deals with the study of light-matter interaction between incident light and nanometer scale two dimensional (2D), and three dimensional (3D) structures. The waveguides, and the photonic crystals (PhCs) are commonly used as nanophotonic devices such as optical interconnects in integrated circuits. Nanophotonic devices have recently generated much interest for their new applications in the field of biomedicine[18], metamaterials[18] and optical microelectromechanical systems (MEMS)[19]. The ever improving lithography techniques for the miniaturization of nanophotonic devices provides exciting new opportunities in the microelectronics industry and help to innovate and grow faster electro-opto-coupled devices.[20] Waveguides[21], photonic crystals (PhCs)[22] and spatially-varied photonic crystals (SVPCs)[23] are some of the examples of nanophotonic devices.

There are several commonly used lithography techniques like soft lithography, electron beam lithography (EBL) and multi-photon lithography (MPL) and many more, which are used to fabricate nanophotonic devices. Electrochemical deposition[24] and soft lithography[25] techniques are better suited to fabricate 2D nanophotonic devices. On the other hand, techniques like X-ray lithography,[26] EBL,[27] and multi-photon lithography (MPL)[28] are well suited for fabricating high resolution 3D nanophotonic devices. X-ray lithography and EBL provide structures with high resolution, but there are some drawbacks associated with these techniques. X-ray lithography not only takes a long time for fabrication, it also requires use of a mask, which makes it quite expensive to use. MPL on the other hand, is not only faster and more user friendly than its competitors, it is also cheaper to use because there is no need to create a mask for the desired 3D structures. This makes MPL highly attractive for fabricating complex 3D structures.

1.3 Multi-photon lithography (MPL)

MPL using photopolymers was first developed by Kodama[29] in 1981. In MPL highly complex 3D structures with sub-micron features are fabricated by using high intensity short laser pulses to initiate non-linear chemical responses in photoresists.[30] The laser pulses are focused on a volume of transparent photoresist using a high numerical aperture (NA) objective, which initiates local polymerization. By scanning the beam within the volume of the photoresist, any arbitrary 3D structure can be made.[31] The sample is washed in a solvent which dissolves the unexposed photoresist leaving behind a free-standing 3D structure.

The photopolymers used in MPL can be broadly classified as negative-tone and positive-tone photoresists. Negative tone photoresists are best suited for creating structures exactly similar to the desired photo-pattern[32] as shown in Fig. 2. The negative-tone photoresist consists of a mixture of a photo-initiator and monomer and it yields structures which are the same as those photo-patterned by laser. The photoresist polymerizes into solid only at the focal spot, and by scanning the focal spot within the volume, a complex structure can be photo-patterned. After photo-patterning the unexposed resist is washed away in a solvent leaving behind a free standing 3D structure.[33] A positive-tone photoresists consists of a photoactive compound, an organic solvent, and a base resin. After photo-patterning the laser-exposed pattern becomes more soluble and dissolves in the developer solvent leaving behind a structure that is the inverse of the photo-patterned design. These resins are useful for fabricating large monolithic blocks with well-defined voids.[34]

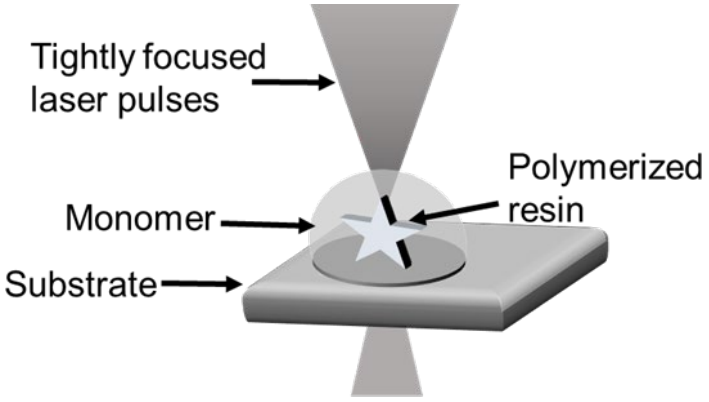

Figure 2. Illustration of the process of MPL. The structure is patterned in a photo-activatable material, such as a photopolymer, via point-by-point scanned exposure using tightly focused ultrashort laser pulses. After exposure, the sample is "developed" by immersing in a solvent that removes the unexposed material, leaving behind a free-standing 3D structure that is a replica of the photo-pattern.

A comparison between the characteristics of negative and positive tone photoresists is shown in Table 1. Some of the most common examples of photoresists used in MPL are poly(methyl methacrylate) (PMMA)[35], SU-8 (epoxy based)[23], Phenol formaldehyde resin (DNQ and Novalac)[36] and IP photoresists (IP-Dip, IP-L 780).[37]

Table 1. Comparison between negative and positive tone photoresists

Characteristics	**Negative-tone photoresists**	**Positive-tone photoresists**
Adhesion to Si	Good	Fair
Cost	Less expensive	More expensive
Minimum feature size	2.0 μm	0.5 μm and below
Solubility in developer	Exposed region is insoluble	Exposed region is soluble
Developer solvent	Organic	Aqueous

1.4 Mechanism and theory of MPL

Multi-photon absorption (MPA) is the fundamental process that enables multi-photon polymerization (MPP). MPA was originally proposed by Maria Göppert-Mayer in 1931 in her doctoral dissertation.[38] But, this prediction was not experimentally verified until the discovery of lasers in 1960s. It was first observed by Werner Kaiser in europium (Eu) doped crystals, while detecting two-photon excited fluorescence.[39]

MPA is a non-linear process in which a molecule absorbs one or more than one, lower energy photons and is promoted from its ground state to a higher energy excited state. Two-photon absorption (2PA) is one of the simplest and most common forms of MPA. However, some commercial photo-initiators used in MPL require three or more photons to bridge the gap between the ground state and first excited state. In that case MPL is initiated by a third- or higher-order process.[40]

An overview and comparison between 1PA and 2PA is shown in Fig. 3(a). 1PA is a linear process in which the initiator absorbs one photon and jumps to the next available excited state. However, in 2PA the initiator absorbs two photons to jump to the next available excited state. The absorption of two photons can be a sequential or a simultaneous process. In a sequential process the absorbing species is excited to a real intermediate state and then the second photon is absorbed. But, in a simultaneous process the absorbing species is excited to a virtual intermediate state. This state is not a true eigenstate of the molecule and has a lifetimes as short as few femtoseconds. The molecule can only undergo 2PA if both the photons arrive simultaneously.

This non-linear intensity dependence for 2PA is important for tightly focusing the laser beam in three dimensions. In MPL, the reaction between the laser beam and photo-initiators occurs at the voxel level. Therefore, the chemical and physical mechanisms involved may differ, when compared to the reactions that occur at the macroscopic levels. Because 2PA requires mediation through a virtual state, it is highly inefficient using an incoherent light source. Thus, ultrafast lasers with picosecond and femtosecond pulse duration are used to achieve high photon flux for 2PA. In a typical MPL system, output from a short-pulse laser such as amplified femtosecond laser is used to initiate MPA, and the laser beam is focused on the sample using a high NA objective lens.[41]

The most significant requirements for the photo-initiator and the monomers used in MPL are (i) they need to be transparent at the laser wavelength used to enable in-volume focusing, (ii) the photo-initiator should a have high two-photon cross-section and high radical quantum yield.[41] For MPL, there are two main classes of photo-initiators: radical initiators and cationic initiators.[42-44] Radical initiators are most commonly used. They generate reactive free radicals, which initiate polymerization of acrylates and vinyl ethers.[45] Most MPP reactions start by an initiating species (usually a free radical).These molecule then react with other monomer molecules and start the solidification process. Sometimes, due to extended laser exposure time or due to slow scan speeds the initiation and propagation steps can occur simultaneously. Therefore, choosing the laser exposure time and scan speed in MPL is always photoresist dependent. An example of TPP by free radical photo-initiators is shown in equations 1-3. The polymerization reactions are defined as initiation, propagation and termination, respectively. The cationic initiators on the other hand are mostly photoacid generators (PAGs), which generate carbocations upon laser exposure.[45] These carbocations initiate polymerization of epoxy-based photoresists. Triarylsulfonium salts,

diaryliodonium salts and ferrocene based salts are some of the most commonly used PAGs in photoresists.[46]

$$PI + 2h\nu \rightarrow PI^{*} \rightarrow R^{\cdot} + R^{\cdot} \quad (1)$$

$$R^{\cdot} + M \rightarrow RM^{\cdot} + M \rightarrow RMM^{\cdot} \ldots \rightarrow RM_{n}^{\cdot} \quad (2)$$

$$RM_{n}^{\cdot} + RM_{m}^{\cdot} \rightarrow RM_{n+m} \quad (3)$$

It is a well-known fact that in order to initiate a polymerization reaction, the incident laser beam must pass the threshold energy barrier for the polymerized structure to survive the washing step of the development process. Figure 3b shows the irradiance is maximum at the focal point and it drops rapidly with distance. The polymer only forms when the tightly confined laser beam reaches the polymerization threshold at the focal point in both axial and transverse directions. The region where the polymer is formed is tightly confined and is sometimes smaller than the focal spot. The irradiance distribution of the laser beam at the focal spot determines the height and diameter of the smallest exposed volume of photoresist described as a “voxel”. Therefore, by carefully controlling the laser power and the scanning conditioning, feature sizes as small as 23 nm have been achieved via MPL.[47]

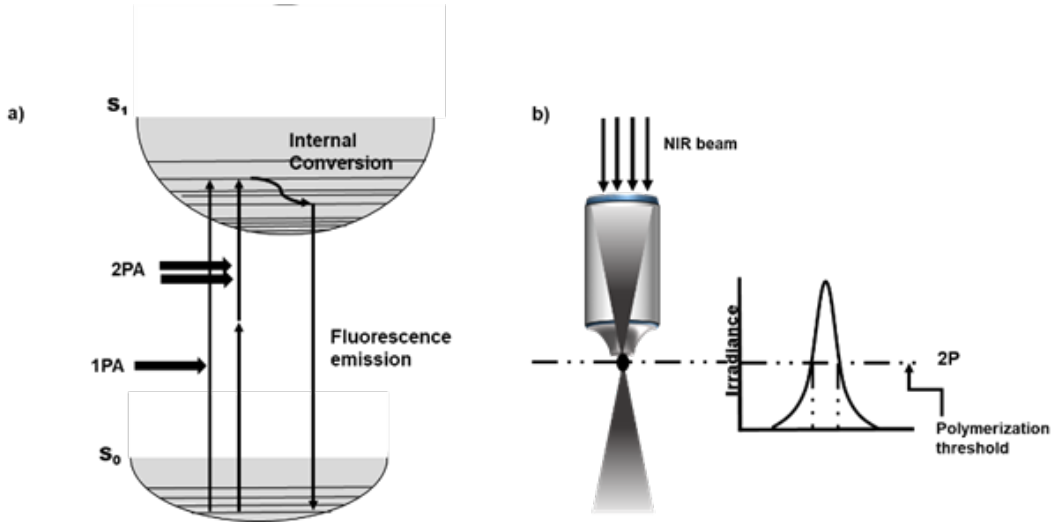

Figure 3. (a). During MPL, initiators in the photopolymer are activated by multi-photon absorption, the simplest case of which is 2PA. Due to the kinetics of polymerization, the degree of monomer conversion varies nonlinearly with local irradiance, which introduces a threshold for polymerization. (b) Monomer is converted to cross-linked polymer at points within the focal volume where the local irradiance exceeds the polymerization threshold. The dimensions of the polymerized volume element, or "voxel," are determined then by the size of the focal spot and the nonlinear response of the material to the irradiance profile in the focal volume.

1.5 Materials for MPL

In conventional MPL both negative and positive tone photoresists are commonly used. However, negative tone photoresists like acrylate[48] and epoxy[30] and methacrylate[49] based resists are more common due to their ease of use. Commercial acrylate photoresists include IP-Dip and IP-S (Nanoscribe). These photoresists can function both as a photoresist as well as an index matching immersion medium, enabling fabrication of complex structures with high resolution and high aspect ratio.[50]

New classes of hybrid materials with improved mechanical strength, good optical properties and increased spatial resolution are also being developed. New chemistries have also been explored via MPA by hydrosilylation of poly(dimethylsiloxane).[51] Hybrid sol-gel materials

like ORMOCERs (organically modified ceramics) have also been developed and used to fabricate functional optical devices.[52]

1.6 Thesis Overview

In this dissertation we have analyzed the source of the distortions observed in the fabricated structures and developed an in-house MPL system, which is free from distortions followed by fabrication and characterization of optical waveguides and uniform lattices. Chapter 1 describes the need for optical interconnects like Nanophotonic devices and details using MPL to fabricate these structure. Chapter 2 explains how the source of distortions in the fabricated structures was identified. Chapter 3 outlines the improvements done in the MPL to fabricate distortion free structures, and how the new MPL setup has improved the quality of the fabrication. Chapter 4 describes the theory of light propagation in 3D structures followed by experimental methods used to fabricate and optically characterize the waveguides and the uniform lattices in the MPL system. Chapter 5 outlines the characterization of waveguides using Er:YAG laser and uniform lattices using amplified femtosecond laser (AFS). Chapter 6 describes a method for etching of Au/Pd coating from the fabricated microstructures. Chapter 7 will offers concluding remarks and plans for future work.

2. ANALYSIS OF LINE DISTORTIONS IN THE FABRICATED STRUCTURES

2.1 Introduction

In commercial MPL systems complex 3D structures with feature sizes close to the diffraction limited spot can be fabricated. High intensity short laser pulses are focused on a volume of photoresist using a high NA objective. Photo-patterning in MPL is mostly done by keeping the laser beam fixed and moving the sample by using a three-axis piezostage (nanostage). For large scale fabrications of up to 100 $mm^2 \times 100\ mm^{2,}$ a combination of piezostage and galvano mirrors are used (Nanoscribe, Photonic professional GT).

Our in-house MPL system is equipped with a nanostage, which can move up to 300 μm in the *x*-, *y*- and, *z*-directions and a short pulsed Ti:sapphire laser as a fixed beam. The fabrication set-up is mounted atop an inverted microscope (Nikon Eclipse 2000). The laser beam is focused from below and the sample is placed upside down on the nanostage. The photo-patterning is done by scanning the laser beam in the volume of the photoresist. This set-up enabled us to view the fabricated structure even in the presence of unexposed monomer.[37] Figure 4 shows the optical setup for fabrication on top of the microscope stage.

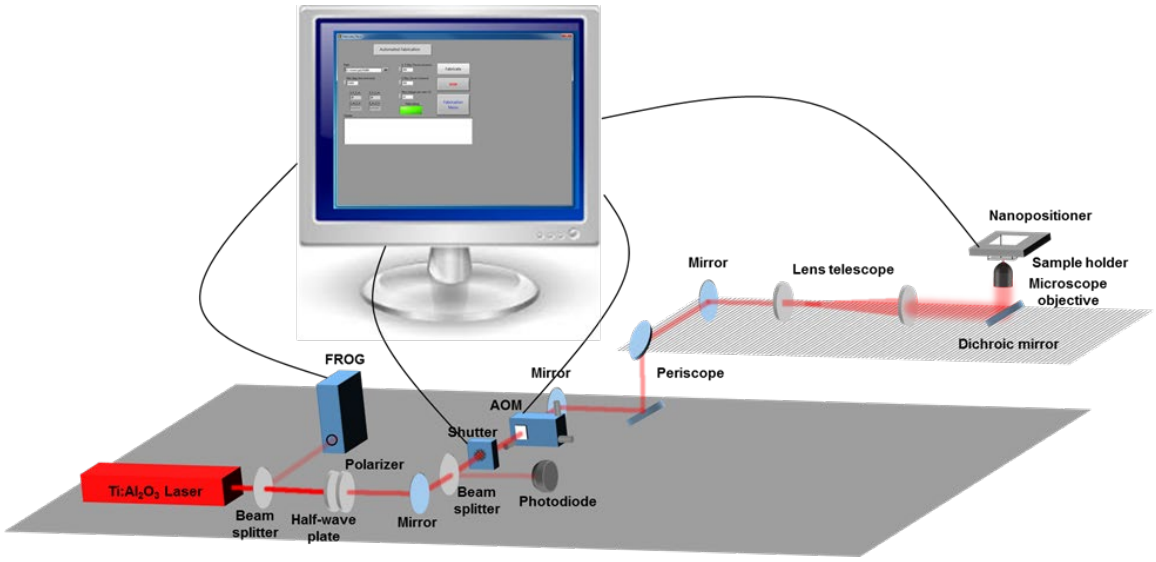

Figure 4. The old MPL setup in which the fabrication was done on top of a microscope and the laser beam was focused from the bottom and the sample was placed upside on the nanostage.[37]

The nanostage movements are controlled by a LabView (National instruments) software and the National Instruments cards. Desired structures are fabricated by commanding to move the nanostage from 0 µm -300 µm by using a "g-code." A "g-code" is a set of information which includes the coordinates at which the stage has to be moved at a specific scan speed and at what power to be used.

IP-Dip was chosen as the photoresist of choice for fabricating structures with better resolution. Since IP-Dip does not polymerize with PAGs, we were able to observe structural characteristics of the structures which were previously invisible to us. A standard structure with two bases and lines was fabricated in IP-Dip with a range of scan speeds of 50 µm/s and 100 µm/s and power ranging from 0.5 mW to 5.5 mW. Optical characterization of the fabricated structures via scanning electron microscopy (SEM) revealed that the fabricated lines in the final structures were not straight but they had distortions in them. Figure 5 shows a comparison between the

fabricated standard structure in the in–house MPL system and the professional grade Nanoscribe lithography system (Photonic professional GT).

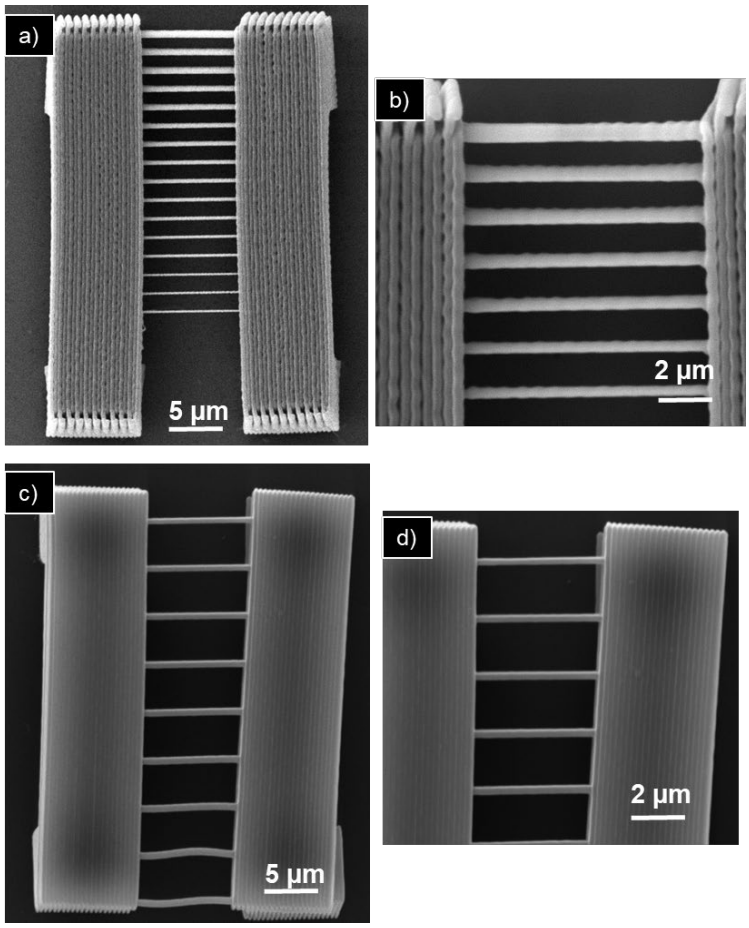

Figure 5. SEM images of the standard structures fabricated in IP-Dip photoresist. (a, b) in-house MPL system. (c, d) Nanoscribe professional GT system.

The in-house MPL system is expected to fabricate structures with smooth lines devoid of any distortions similar to the Nanoscribe professional GT system. This chapter outlines how we were able to not only pin point the source of these distortions, but also made improvements in the MPL system to fabricate structures with improved resolution and consistency.

2.2 Methods

The main components of a MPL system are (a) high intensity short pulsed laser, and (b) a nanostage (PI, Physik Instrumente). The wavelength (800 nm) and pulse duration (120 fs) of the laser were within range when measured via a spectrometer (Oceanoptics, USB4000) and frequency resolved optical grating (FROG, Swamp optics, Grenouille) respectively. Since the laser was stable through-out the fabrication, we can rule out the laser as the source of distortions. The nanostage on the other hand is a precise positioning and scanning tool which made it possible to fabricate sub-micron features via MPL. Besides the nanostage, the resonance in the electrical circuits or the mechanical vibrations in the lab may have been the source of these distortions. To pin-point the source we hypothesized that:

(i) The nanostage is not moving at a constant speed and reaching its intended position as specified via LabView. To confirm this hypothesis, a calibration standard was used and the nanostage movement was observed as shown in section 2.2.1.

(ii) The electrical circuits in the nanostage are in resonance with the devices in the building. This resonance is causing the nanostage to vibrate at a constant frequency of 60 Hz or the multiples of 60 Hz (120 Hz, or180 Hz). To confirm this hypothesis, we took two approaches. In the first approach we measured the frequency of the distortions in the fabricated lines in the second approach the frequency of the nanostage vibrations in *x*-, *y*-, and *z*- axes was measured by connecting the nanostage sensor-monitor to an oscilloscope as shown in section 2.2.2.

(iii) The mechanical vibrations in the lab are causing the vibrations in the nanostage during fabrication. The source of the mechanical vibrations could be attributed to the air

conditioning recirculators, or due to the positioning of the nanostage far from the floating table. To confirm this hypothesis, the vibrations were measured by moving the nanostage on different positions of the floating table and by turning the air conditioning recirculators off. The results for this measurements are shown in section 2.2.3.

The hypothesis were tested by using the sensor-monitor and monitoring the nanostage movements via an oscilloscope (Tektronix TDS 2014).

2.2.1 Monitoring the nanostage movement using the calibration standard

Several tests were done to determine if the nanostage was performing as specified. The first test was to simply ensure that the stage was moving approximately to the commanded positions. The nanostage movement had already been tested by PI and showed to move to the commanded position within 80 nm.[53] We used a calibration standard (Ted Pella, Metrochip microscope calibration target) to test the nanostage movement. The calibration standard has several different patterns, including one that is a grid of 50 μm squares. The nanostage was commanded to move in 50 μm increments and the movement was monitored by an optical microscope.

2.2.2 Monitoring the line distortions due to electrical resonance

To investigate the source of the line distortions, (a) a detailed structural analysis of the fabricated structures was done and the frequency, the time period and the distance of the distortions was measured, (b) the frequency of the nanostage vibrations was measured by oscilloscope.

a. A standard structure with two bases and lines connecting them was fabricated via MPL as shown in Fig 6. The rectangular bases were fabricated at 5 mW power and a scan speed of 150 µm/s in *x*- axis. In the top structure (Fig. 6a), the lines were drawn in the *y*-direction at 100 µm/s with power ranging from 5.5 mW – 0.5 mW However, in the bottom structure (Fig. 6d) the lines were drawn in the *y*-axis at 50 µm/s and power ranging from 5.5 mW – 0.5 mW. At 100 µm/s no lines were observed from 0.5 mW - 2 mW and the lines were merged with each other at 2.5 mW. However, at 50 µm/s no lines were observed from 0.5 mW - 1 mW.

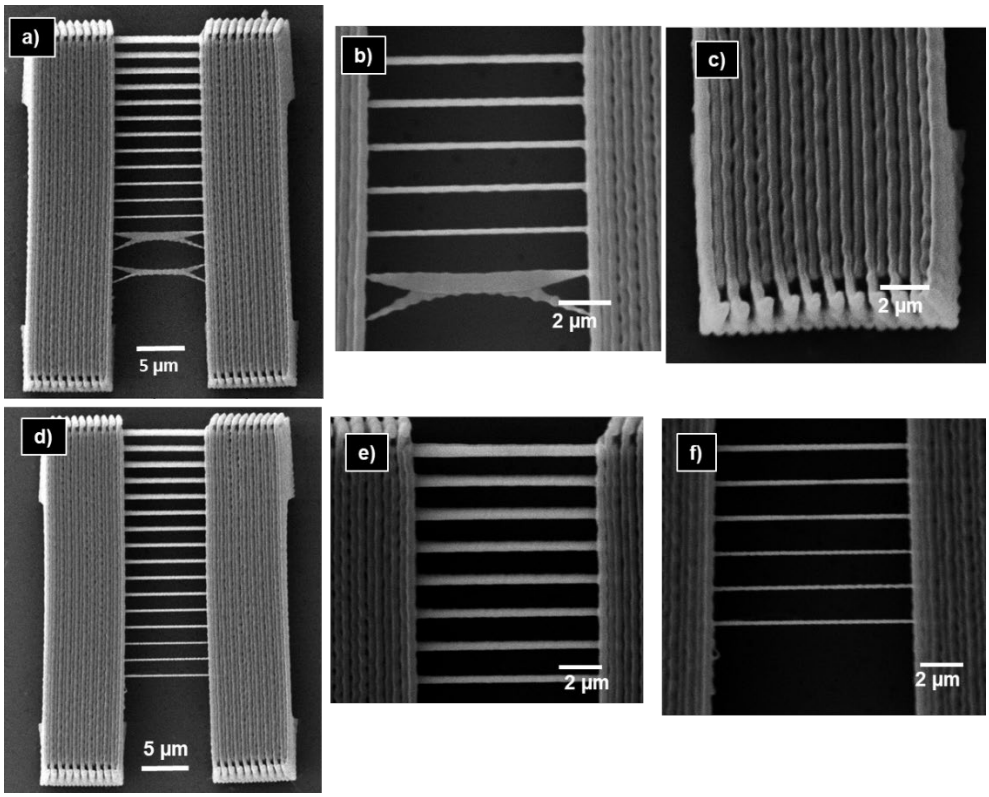

Figure 6. SEM images of the power array (a, d) standard structures with rectangular bases fabricated at 150 µm/s and 5 mW power. (b, c) magnified view of the structure a with lines drawn along *y*- axis at power ranging from 0.5 mW to 5.5 mW with 100 µm/s scan speed. (d, e) magnified view of the structure d with lines drawn along *y*- axis at power ranging from 0.5 mW to 5.5 mW with 50 µm/s scan speed.

b. The nanostage was anchored on the top of the microscope (which is the fabrication area) and the nanostage servo-controller was connected to an oscilloscope. The sensor-monitor was used to control the servo-systems which consists of a motor, and a feedback device. There are individual *x*-, *y*-, and z- axes switches in the sensor-monitor which gives us more control over the experiment. The vibrations in the nanostage were measured by an oscilloscope as peak-to-peak signals (V) with 2 mV signal per division for *x*-, *y*-, and *z*- axes. The frequency of the noise levels observed in each axis was measured individually by Fast-fourier transform (FFT) analysis. FFT converted the signal into the corresponding frequency domain, which made the analysis of the vibration easier. For each FFT measurement, the switch for only one axis was "on" while switches for other two axes were "off".

2.2.3 Vibration analysis at different fabrication positions

In this experiment the stage was placed at three different positions as shown in Fig 7. The aim for this experiment was to see if the floating table was able to dampen the vibrations felt by the nanostage as it moves away from the floating table. The nanostage was placed a) on the microscope, b) on the platform in between microscope and floating table, and c) directly on the floating table.

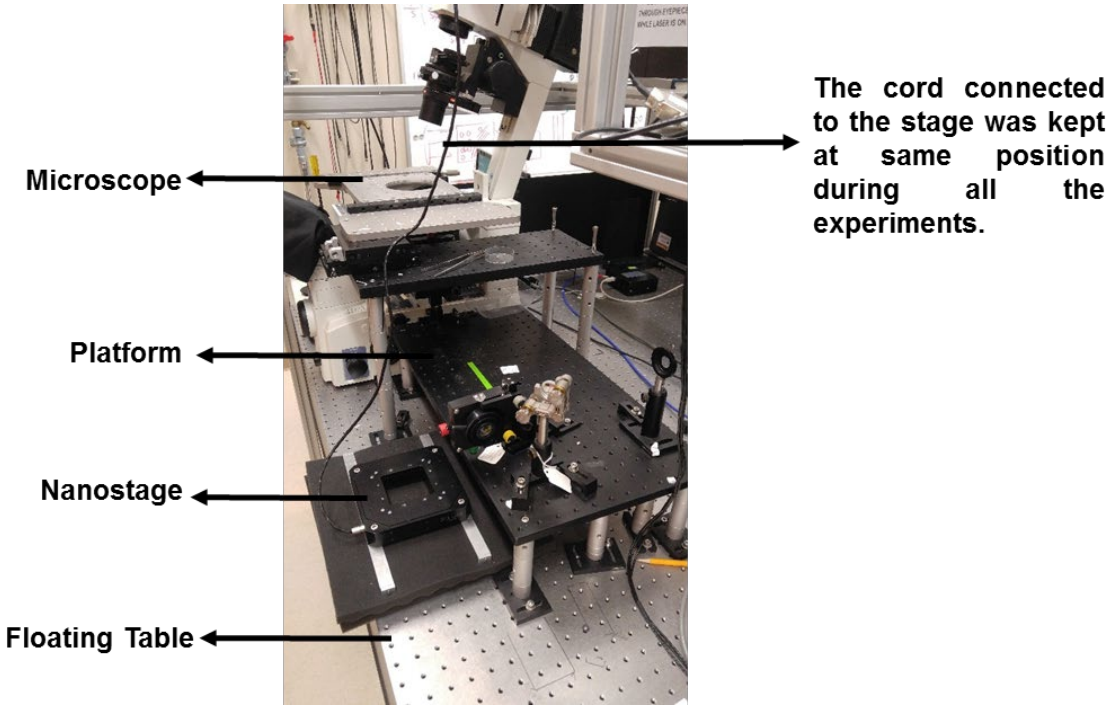

Figure 7. Shows the experimental set up to observe vibrations in the nanostage when placed at different positions in the lab. The cord connected to stage was kept at the same position in all the experiments. The servo controllers of the nanostage were connected to the oscilloscope and the vibrations were measured in terms of voltage.

For more precise measurement of stage movements, the nanostage was driven by LabView and the NI cards, and the sensor monitors were read using an oscilloscope. The stage was then commanded to move in 50 µm increments in the *x*- axis. To extract a voltage from the oscilloscope, the display average function was selected, which gives the average voltage reading for each channel over the specified time frame, which in this case was 25 ms per division. To get an exact measurement of the signal; peak-to-peak operation was selected with 2.00 mV signal per division.

The air-conditioning recirculators whose job is to circulate the air in the lab was located exactly above the fabrication setup in the ceiling. The circulator were turned off and the vibrations in the nanostage were measured via an oscilloscope. The FFT of the *x*-, *y*-, and *z*- axes were

measured. For each FFT measurement the switch for only one axis was on, while the other two were off.

2.3 Results and Discussion

Nanostage movements were observed using an objective (Nikon Plan-fluor 40x/0.72 WD). No images were taken using the microscope, but the observations were consistent with the nanostage behaving according to manufacturer's specifications. When commanded to move 50 μm in the *x*-direction (using LabView), the stage moved from the edge of one square to the edge of a square directly adjacent, signifying a 50 μm movement. When the nanostage was commanded to move 100 μm, the stage moved from the edge of one square, to the edge of a square 2 squares away, signifying a 100 μm travel. This was repeated for additional 50 μm increments as well as in for movements in the *y*- direction. All observations were consistent with the nanostage moving as specified.

The distance (nm), the amplitude (nm), and the frequency (Hz), of the distortions in the structures shown in Fig 6 were measured via MATLAB image processing tool. Each figure of merit was measured four times to get an average and standard deviation of the final values.

Table 2. Shows the distance, amplitude and frequency of the distortions shown in Fig.6.

Power (mW)	Scan speed (µm/s)	Distance (nm)	Amplitude (nm)	Frequency (Hz)
5.5	100	446 (± 23)	158.8 (± 18)	223
5.0	100	446.7 (± 32)	142.8 (± 12.9)	223
4.5	100	464 (± 22)	123.3 (± 20.3)	215
4.0	100	458.3 (± 6)	123.3 (± 11.2)	218
3.5 – 2.5	100	Cannot calculate	93.7 (± 22)	
5.5 – 2.5	50	Cannot calculate	106.0 (± 15)	
2.0	50	257 (± 15.9)	91.0 (± 0)	194
1.5	50	264 (± 12.9)	106.0 (± 26)	189
5.0	150	829 (± 23)	236.8 (± 45.8)	181

The distortions observed in a structure fabricated at two different scan speeds and at different powers is shown in Table 2. At 100 µm/s the distance of the distortions was in the range of 450 (± 23) nm. On the other hand, at 50 µm/s distance the distortions were in the range of 250 (± 13) nm. Only one data point was available for the scan sped at 150 µm/s, and in this case the distance of the distortions were 829 nm. The amplitude of the distortions also follow a pattern similar to the distance. The amplitude of the distortions increase with scan speed. However, within the lines fabricated at one scan speed, the amplitude remains unchanged. The amplitude was in the range of 100 (± 20) nm at 50 µm/s, 140 (± 20) nm at 100 µm/s and 236.8 (± 45.8) nm at 150 µm/s. This shows that the size and amplitude depends more on the scan speed than the laser power at which they were fabricated. The frequency of the distortions ranged from 190 Hz - 220 Hz, and they were also independent of the fabrication conditions. The results shown in this section confirm that the distortions observed in the fabricated structures were dependent on fabrication conditions (power and scan speed). Since, the distortion frequency was not in the range of the electrical

resonance frequency (60 Hz or multiples of 60 Hz) we can conclude that, the electrical resonance cannot be the source of these distortions.

To further prove our results, we measured the noise levels by an oscilloscope when it was stationary and there were no other sources of vibrations. We connected the nanostage sensor-monitor to an oscilloscope and measured the noise in the *x*- , *y*- , and *z*- axes. The oscilloscope was triggered on the *y*- axis and the peak-to-peak signal was measured at 2 mV per division scale.

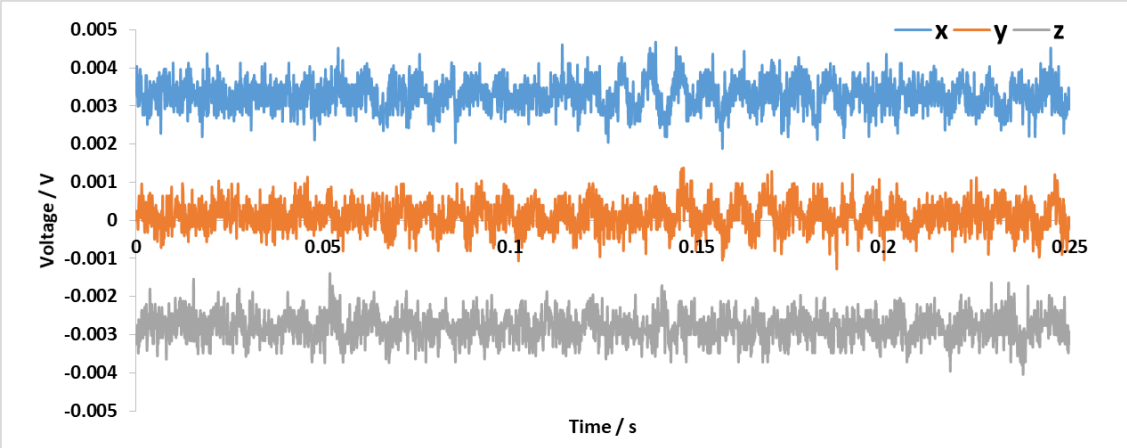

Figure 8. Oscilloscope traces of *x*- , *y*- , and *z*- axes when the stage was anchored to the microscope

The oscilloscope traces in Fig. 8 show that when the stage was stationary at 0 V the *x*- and the *z*- axes have an offset of 0.003 V. The peak-to-peak signal for *x*- , *y*- , and *z*- axes were 2.80 mV, 2.64 mV and 2.64 mV respectively. The frequency of the noise was measured by the FFT for each axis as shown in Fig. 9.

The *x*- , *y*- , and *z*- axes vibrate at 101 Hz, 145 Hz and 102 Hz respectively, which is not close to the electrical resonance frequency (60 Hz or multiples of 60 Hz). Therefore, the FFT

measurements confirm that the distortions observed in the nanostage are not due to the resonance between the nanostage circuits and other electrical devices in the building.

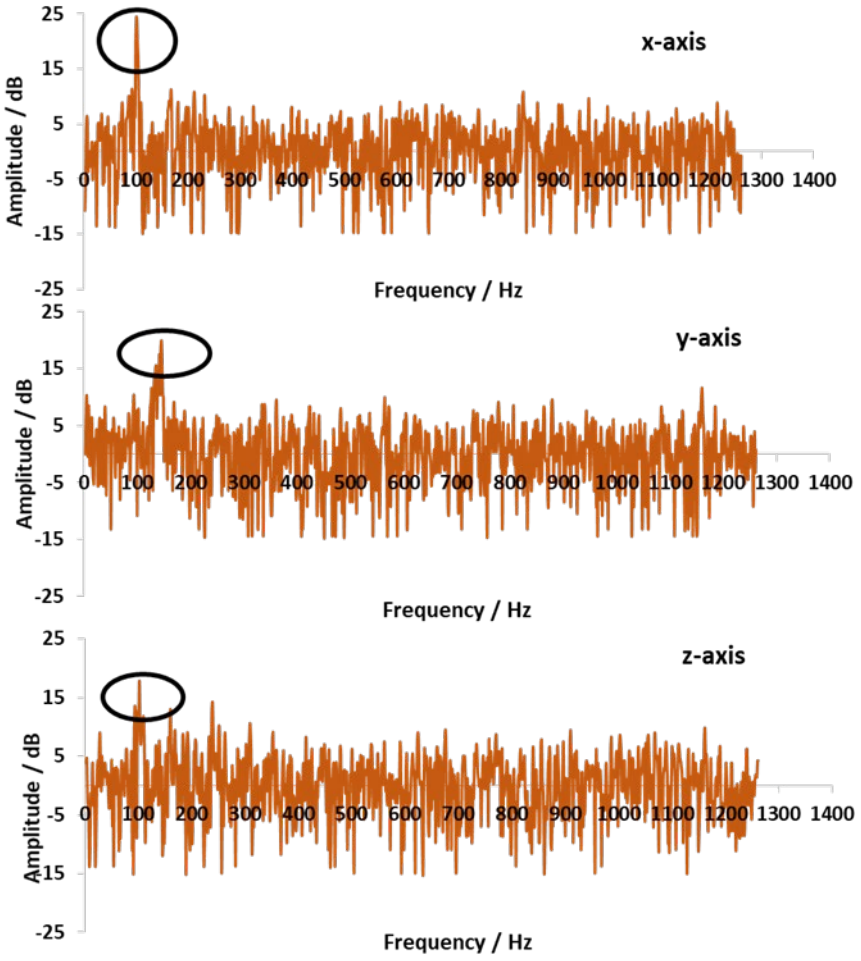

Figure 9. FFT plots for *x*-, *y*-, and *z* – axes when the nanostage was stationary and anchored on the microscope. The circle drawn in each plot shows the noise level in that particular axis.

The MPL setup was on the top of a microscope which was 64 cm above the floating table. To explore the effect of position on the vibrations, the stage was placed on different positions as shown in Fig.7 and the vibrations in the *x*- , *y*-, and *z*- axes were measured with an oscilloscope. In Fig 10, the blue trace is the *x*-axis source at which the oscilloscope was triggered and the peak-

to peak signal was measured. Yellow and pink traces are the *y* and *z*-axes traces, respectively. The average peak-to-peak signal strength when the nanostage was placed (a) on the microscope, (b) on the platform, (c) on the floating table was 2.38 mV, 1.67 mV and 0.6 mV, respectively. These results show that the floating table was able to completely dampen the vibrations observed by the nanostage, and the vibrations observed by the nanostage increase as it moves away from the floating table.

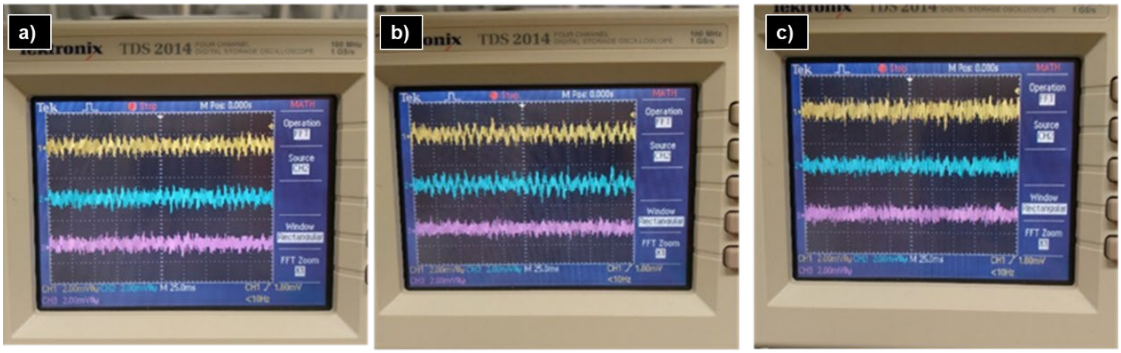

Figure 10. Oscilloscope traces when the nanostage was placed (a) on the microscope (b) on the platform (c) on the floating table. The oscilloscope was triggered with Ch2 (blue trace) and the stage was moved in *x*-axis. Yellow and pink traces show the noise levels in *y*- and *z*-axis respectively.

To find the best possible position for fabrication on the floating table some more tests were performed. All the experiments listed here were done on the floating table. In these experiments the nanostage was placed a) on top of four 4 inch aluminum columns, b) on top of a solid metal block, c) directly on the floating table, d) a temporary fabrication set up prepared by using four 6 inch aluminum columns and a metal base, and e) on top of four 6 inch steel columns. The nanostage was connected via servo controllers to the oscilloscope. The oscilloscope was set up to be triggered with Ch1 with a time frame of 25 ms per division and peak-to-peak operation was selected with

2.00 mV signal per division. The vibrations observed by the nanostage were measured via oscilloscope when it was commanded to move from point A to point B. Figure 11 shows a compilation of the oscilloscope traces with the nanostage position.

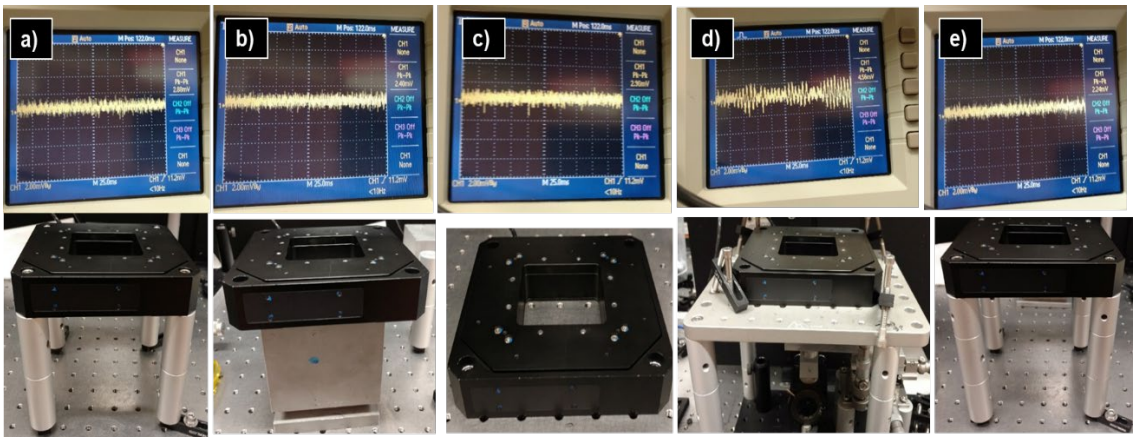

Figure 11. (Top) Oscilloscope traces show the vibration observed by the nanostage with respect to the corresponding (Bottom) stage position. (a) On top of four 4 inch aluminum columns, (b) on top of a solid metal block, (c) directly on the floating table, (d) a temporary fabrication set up prepared by using four 6 inch aluminum columns and a metal base, and (e) on top of four 6 inch steel columns

The oscilloscope traces show that the nanostage observed maximum vibration when it was place on top of the temporary fabrication set-up as shown in Fig. 11d and minimum when the stage was placed directly on the floating table as shown in Fig 11c. Comparison of the noise levels confirmed that greater the height of the stage from the floating table greater will be the vibrations observed.

The vibrations in the *x*- , *y*- , and *z*- axes were also measured via an oscilloscope when the air conditioning recirculators were turned off. The FFT of the oscilloscope traces shown in Fig. 12 revealed that the after turning off the recirculators and moving the nanostage on to the floating table resulted in signals free from any measureable vibrations.

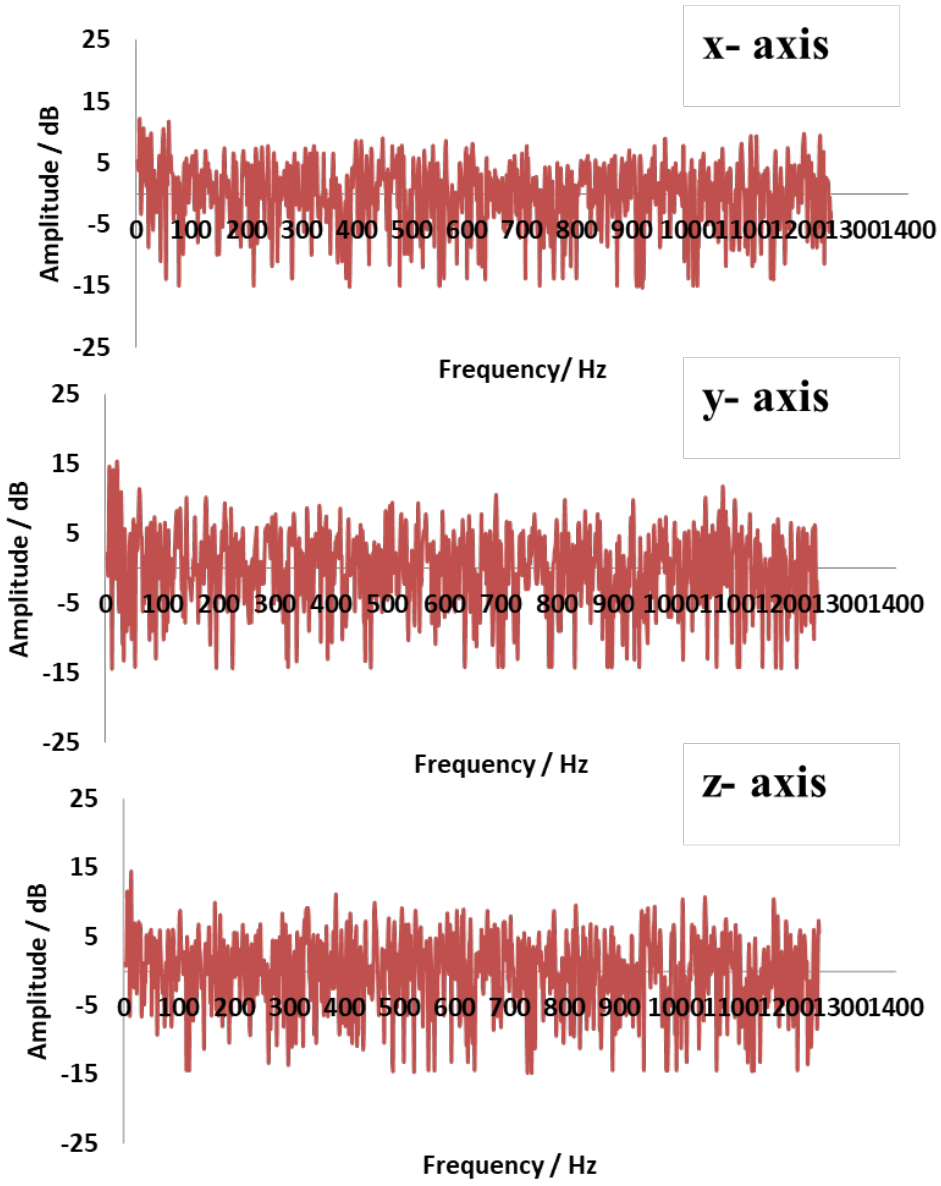

Figure 12. FFT plots for *x*-, *y*-, and *z* – axes when the nanostage was stationary and anchored on the floating table with air conditioning recirculators turned off.

2.4 Conclusion

The source of the distortions observed in the fabricated structures was identified. The nanostage was working according to the specifications when the stage movement was calibrated

with a standard. The frequency of the distortions in the fabricated structures was quantified by MATLAB, and the FFT was used to assess the vibrational frequency of the *x*-, *y*- and *z*-axes in the nanostage. The distortion frequency in the fabricated structure was 190 Hz – 220 Hz and it was independent of the fabrication conditions. However, the FFT measurements confirmed that the *x*-, *y*- and *z*-axes in the nanostage vibrate at 101 Hz, 145 Hz and 102 Hz, respectively which is not specific to the frequency of electrical resonance (60 Hz or multiple of 60 Hz). These results confirmed that the source of the distortions in the fabricated structures was not due to the electrical resonance in the nanostage circuits. In the end, it was proved that the source of the distortions was mechanical vibrations. The floating table was incapable of dampening the vibrations in the nanostage because it was placed on the microscope which was 60 cm above the floating table. By moving the nanostage closer to the floating table and by turning off the air-conditioning recirculators off, the vibrations observed in the oscilloscope were considerably reduced.

3. DEVELOPMENT OF NEW MPL SYSTEM

3.1 Development of new MPL optical setup

A new MPL set up was prepared using new optical elements which enabled us to keep the nanostage (Physik Instrumente 563.3 CD) on the floating table. The output of the mode-locked Ti:sapphire laser (Coherent-Mira, 800 nm center wavelength, 120 fs pulse duration, 76 MHz repetition rate) is used as a source for MPL. To measure the pulse-width of the input laser beam, a beam-splitter was placed after the laser output to direct a reference beam to a frequency resolved optical grating (FROG). The beam was then routed through a half-wave plate/polarizer combination, which makes the beam vertically polarized and also allows manual adjustment to control the power reaching the sample. A second beam splitter was placed after a half wave plate/polarizer to guide a portion of the beam to a photodiode (Thorlabs, Det210) to measure the average power of the input laser beam. The beam passing the shutter reached the acousto-optic modulator (AOM, Gooch and Housego) which enabled automation of power. The input beam was diffracted by the AOM. The zeroth order beam was selected for fabrication and the higher order beams were blocked by an aperture.

The attenuated beam passed through a periscope which adjusts the beam height. It was then passed through a lens telescope which consists of a beam expander (1” lens, f = 300 mm), a collimator (1” lens, f = 50 mm) and a beam splitter (Ø2" 10R:90T, Thorlabs,BSN17, UVFS Plate Beamsplitter, Coating: 700 - 1100 nm, thickness = 8 mm). The collimated beam was then reflected by a 45˚ silver coated prism (Right-Angle Prism Mirror, Protected Silver, L = 25.0 mm, Thorlabs MRA25-P01) on the objective and overfills the back of 60x/1.4 *NA* microscope objective (Nikon Type A oil, n =1.51 at 800 nm). The collimated laser beam was focused by the objective on the

sample which was placed on the nanostage. The average zeroth order beam reaching the sample was calibrated by using an integrating sphere. A third beam splitter was placed after the lens telescope assembly which guides a portion of the back reflected beam from the sample towards the lens (1" lens, f = 100 mm). A camera (Photometrics, Coolsnap CCD camera) was placed at the focal point of the lens. The IP-Dip/ SU-8 interface of the sample was located by monitoring the back reflected image on the camera, which was viewed on the computer. The optical set up of the new MPL system with nanostage on the floating table is shown in Fig. 13.

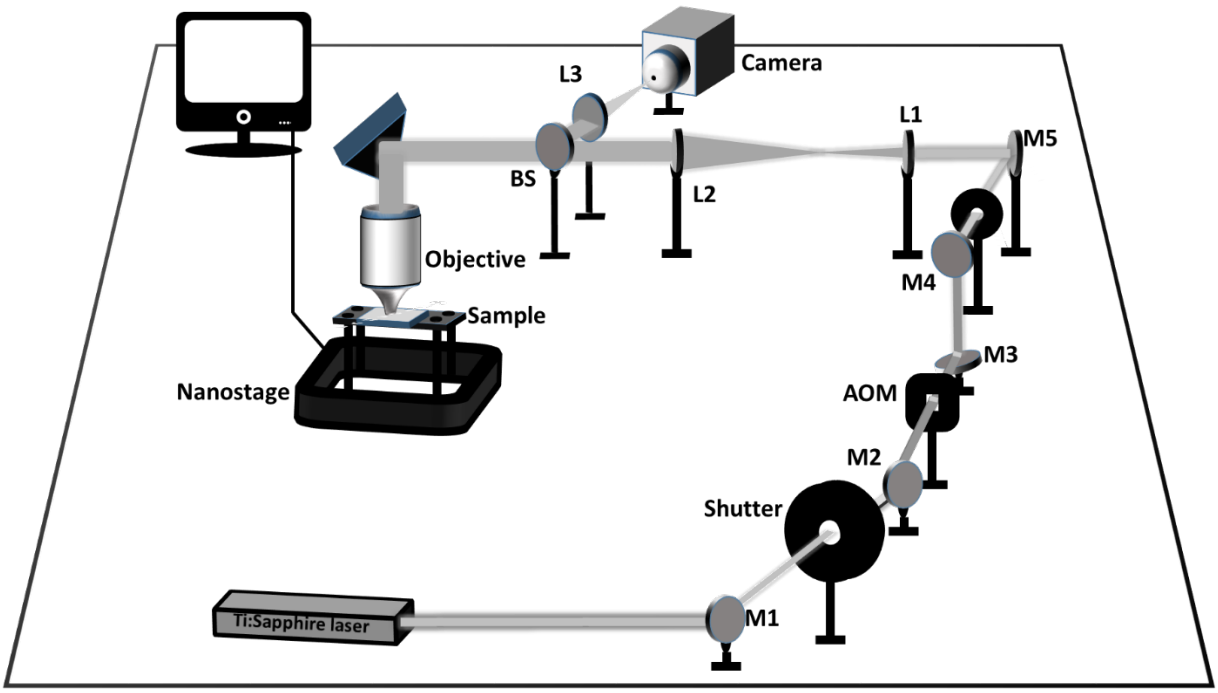

Figure 13. Perspective view of the new MPL on the floating table. The nanostage was kept closest to the floating table which can dampen vibrations due to stage movements. M: Mirror, L: Lens, BS: Beam splitter.

3.2 Calibration of the integrating sphere

In MPL, it is important to calibrate the integrating sphere using the input laser beam if any changes are made in the fabrication setup: for example, if any optics are changed in the laser, if the laser is realigned, or if the fabrication wavelength is different than 800 nm. The LabView and the AOM were used for the power automation required to fabricate via MPL. A calibration plot between the voltage (V) and the average laser power (mW) is performed prior to each fabrication so that by changing the voltage the AOM can control the power reaching the sample. This calibration plot is formed by using a LabView VI, which can fit the laser power in a plot between V and mW using the slope and intercept measured by calibration of the integrating sphere.

The integrating sphere was calibrated by using a photodiode (Newport Model 818 UV). The integrating sphere was connected to the computer and the OL test panel software was used to read current in Amperes. The photodiode was connected to the Newport power meter (1835C), which reads the power in mW. The optical setup for the calibration is shown in Fig 14. The integrating sphere was placed in between the two beam expanders and adjusted so that the full lateral extent of the beam is captured in the center of the detector. The photodiode was placed on a tilt mount in front of the integrating sphere and adjusted so that the beam is centered on both the photodiode and the integrating sphere.

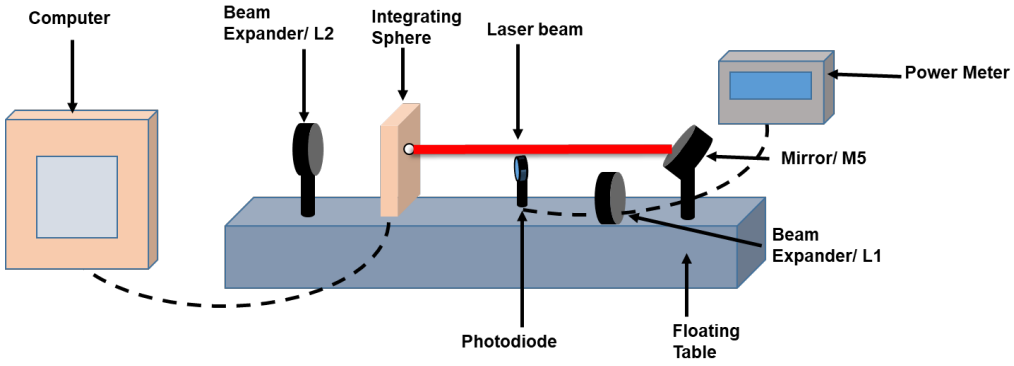

Figure 14. Optical setup for integrating sphere calibration using a photodiode. The integrating sphere was connected to the computer and current (A) was read using OL panel software, the photodiode was connected to a power meter and power (mW) was read at 800 nm.

This measurement is done in dark as ambient light is detected by the photodiode and it can result in false readings. A set of neutral density (ND) filters were used to prevent saturation of the detectors. The half-wave plate/polarizer combination was used to adjust voltage from 0.15 V - 2.15 V. At each point the photodiode power (mW) and the integrating sphere current in amperes (A) were measured and plotted as shown in Fig 15. The slope 109211 ± 271.45 mW/A and *y*-intercept 0.0393 mW were extracted with linear regression (R^2) 0.999. The value of slope and intercept were used to fit a calibration curve for AOM power automation in the LabView software.

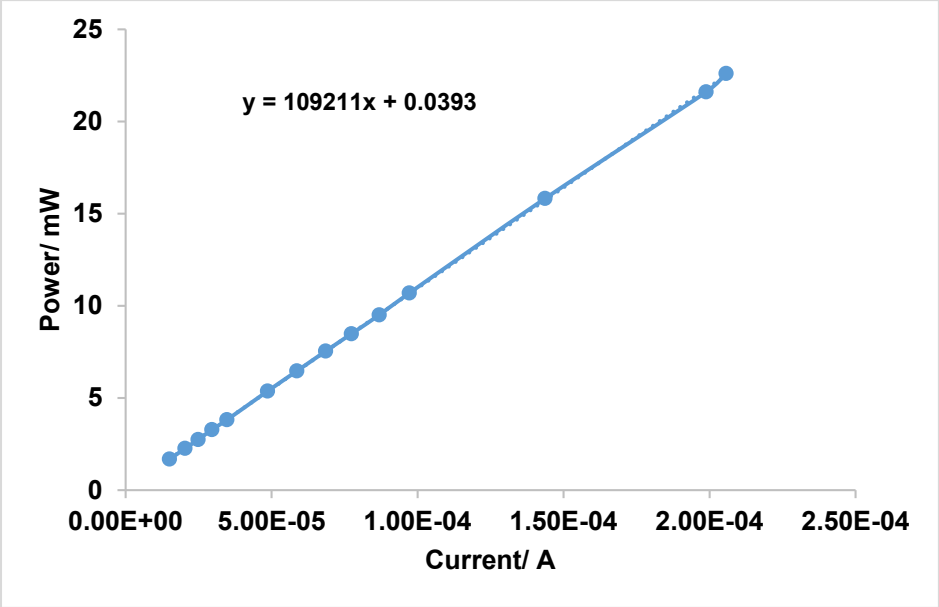

Figure 15. Shows calibration curve of integrating sphere (A) and photodiode (mW). The slope and intercept from this plot are used to make calibration curve for AOM power automation in MPL.

3.3 Installation of a new RF driver in the acousto-optic modulator (AOM)

An acousto-optic modulator (AOM) was used to control the intensity of the laser beam based on the acousto-optic effect. An acousto-optic effect is the modification of refractive index of a crystal by sound waves. A schematic illustration of the AOM is shown in Fig. 16. In the AOM a piezoelectric transducer is attached to the transparent crystal (TeO_2, crystalline quartz or fused silica). The transducer is used to excite sound waves of 80 MHz, which results in creating a diffraction grating by changing the refractive index of the crystal.

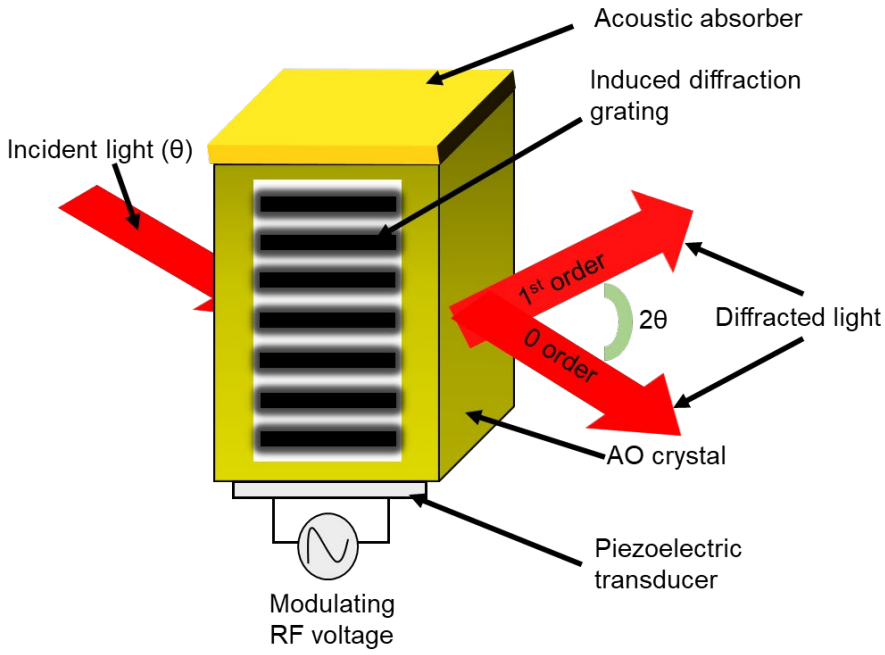

Figure 16. Schematic illustration of the principles of AOM.

In the MPL system, an AOM is used to automate power reaching the sample during fabrication. An in-house voltage divider box was made using the RF driver with output power 2 W. Its function is to take a low current (< 1 mA) output of 0 V - 10 V and convert it to a higher current output of 20 mA, by stepping down the voltage linearly to the range of 0 V - 1 V. The input to the RF driver is max at 1 V, whereas the NI cards are max 10V, so we need to step down the voltage, as well as buffer the current up to 20 mA. The higher current is needed because the RF driver presents a load of 50 Ohm, so whatever drives it must be able to provide at least 20 mA.

Figure 17 (a, and c) show the AOM voltage divider box with the lid on and off respectively. Figure 17 (b) shows the AOM used in the fabrication set up. The laser power diffracts into the first order, and the transmitted zeroth order was used in fabrication. The zeroth order beam was used for fabrication because it was circular with pulse duration of *ca* 120 fs which was required for 2PP. The first order beam on the other hand was blocked from reaching the fabrication set-up because

it was elliptical in shape with a pulse duration *ca* 200 fs, which makes it challenging to overfill the back side of the objective

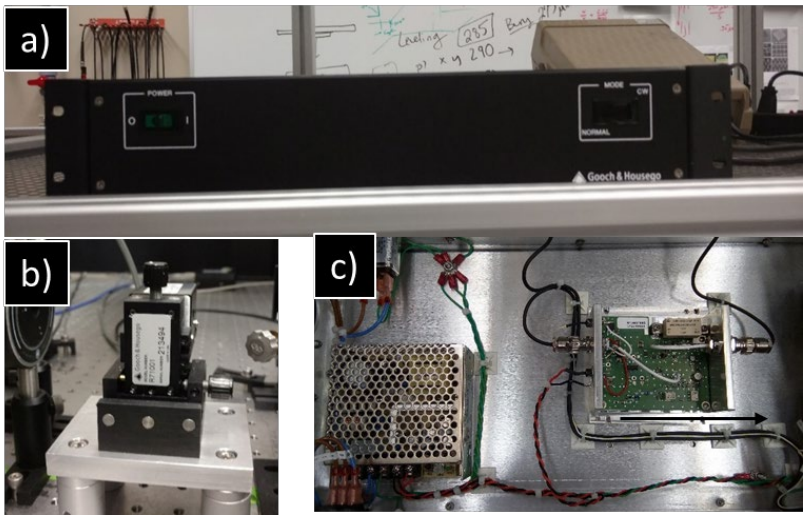

Figure 17. (a). In-house voltage divider box whose major components are a fan and a RF driver, (b) the AOM was placed in the beam path, and (c) Inside of the line divider box.

The voltage range at which the RF driver works is 0 V- 10 V. At 10 V command from LabView results in maximum diffraction of the laser beam and minimum diffraction for 0 V for from the crystal. A calibration plot was made between V versus average laser power <P> in the units of mW (using the integrating sphere) by fitting the slope and intercept values measured in section 2.3.2 in calibration of integrating sphere. The RF driver has to work with maximum power and frequency for maximum diffraction of the laser beam.

The output power of the RF driver is the one of the most critical factors controlling the diffraction efficiency of the AOM crystal. According to the manufacturer, the RF driver has a maximum power output of 2 W. To confirm that we measured the power output of the RF driver. By using a T-BNC connector the AOM was connected to the line driver box on one end and to the oscilloscope on the other end. The AOM was connected to the oscilloscope with a second T-

connector, a 50 Ω terminator was used on the other end of the second T connector. The AOM extracts current from the line driver box for normal diffraction, if the AOM was connected to the oscilloscope directly without a terminator it will extract current from the main circuit. This may overload the AOM and in-turn burn the TeO_2 crystal. Therefore, a 50 Ω terminator was used at the oscilloscope to prevent the AOM from burning itself. The LabView was used to command voltage (0 V – 10 V) to the line driver and the voltage at the AOM was measured via oscilloscope in the form of V_{RMS}. Equation 4 was used to convert V_{RMS} to power.

$$< P >= \frac{V_{RMS}^2}{R} \tag{4}$$

where <P> is the average power in the units of mW at which the RF driver is working, V_{RMS} is the AOM voltage trace measured via oscilloscope and R is the resistance which is 50 Ω. By using equation 4 the maximum power output power from the RF driver (installed in 2014) was measured again in 2017. The maximum was slashed to 0.793 W in 2017 from 1.37 W in 2014.

A new RF driver was installed in the AOM power source, and calibration was done to align the laser beam for maximum diffraction at the Bragg angle. A comparison between the old and new RF driver efficiency is shown in Fig. 18 as a plot between the average laser power <P> in the units of W versus LabView commanded voltage (V). At 10V (maximum diffraction) in the old RF driver has the maximum power of 0.793W, but the new driver was working at 1.2 W.

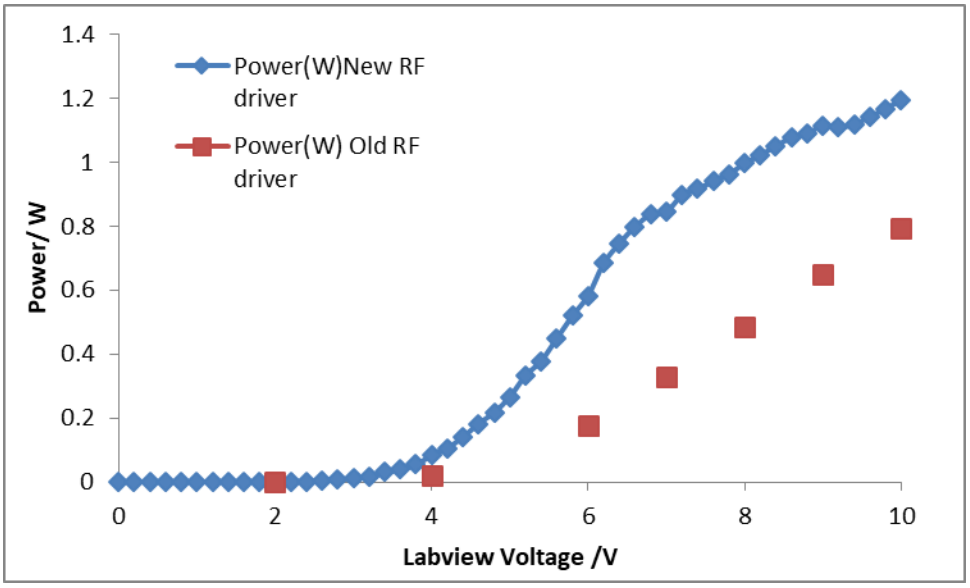

Figure 18. Output power by the old and new RF driver with respect to the LabView commanded voltage range from 0 V to 10 V.

The diffraction efficiency of the AOM was measured using the detector with respect to the commanded LabView voltage by using the equation 5. A diffraction efficiency of 89.5% was measured using the new RF driver. The diffraction efficiency of the new RF driver was within the manufacturer's specifications (> 70% for 700 nm - 1000 nm).

$$Diffraction\ efficiency = \frac{First\ order\ Power\ (diffracted)}{Zero\ Order\ Power\ (undiffracted)} \quad (5)$$

A relationship between the first - and zero-order diffracted power with respect to the commanded LabView voltage is shown in Fig 19. The diffracted power was measured by using a detector (OL 731) and the power was read by Newport power meter (1835C). Minimum diffraction was seen at 0 V with maximum power in the zero-order undiffracted beam and minimum power in first order diffracted beam. At voltage below 3 V and above 8.5 V, the diffraction curve was flat. Thus, using the calibration curve for fabrication, a range of 3 V to 8.8 V was selected.

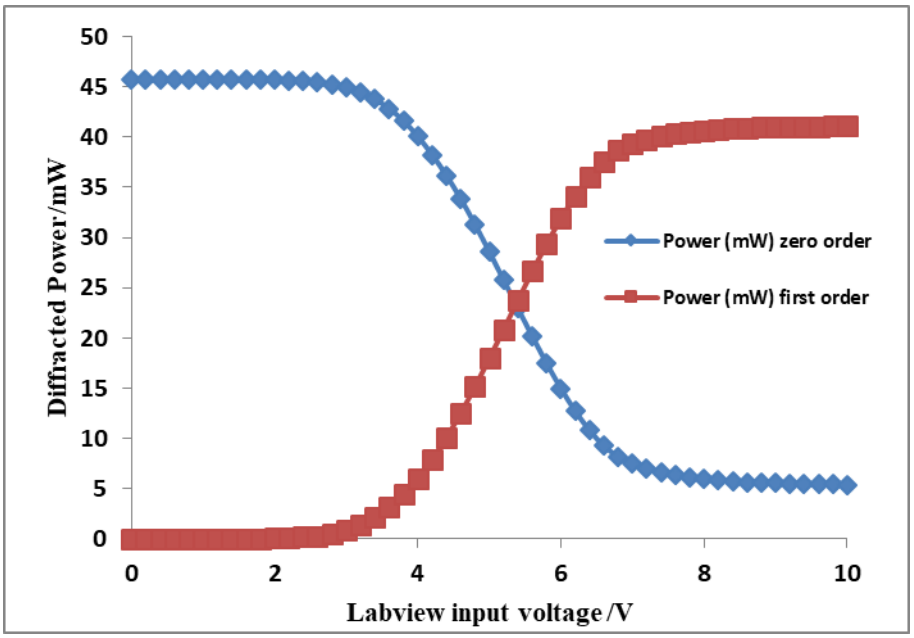

Figure 19. Zero order and first order diffracted power was measured with detector and the output power was observed using a power meter with the range of labview input voltage ranging from 0 V to 10 V.

When the laser beam was aligned at Bragg angle on the AOM crystal 89% of the input beam is diffracted to the first order. The first order beam was blocked but zero order beam was allowed to reach the fabrication setup. The zero order beam was calibrated within a range of 3 V - 8.8 V. LabView commanded voltage by overfilling the back side of a high NA objective and focused onto the integrating sphere. The calibration curve at the integrating sphere had a diffraction range of 0.44% as compared to 11.5% at the detector. This was explained by observing the beam profile as shown in Fig. 20a.

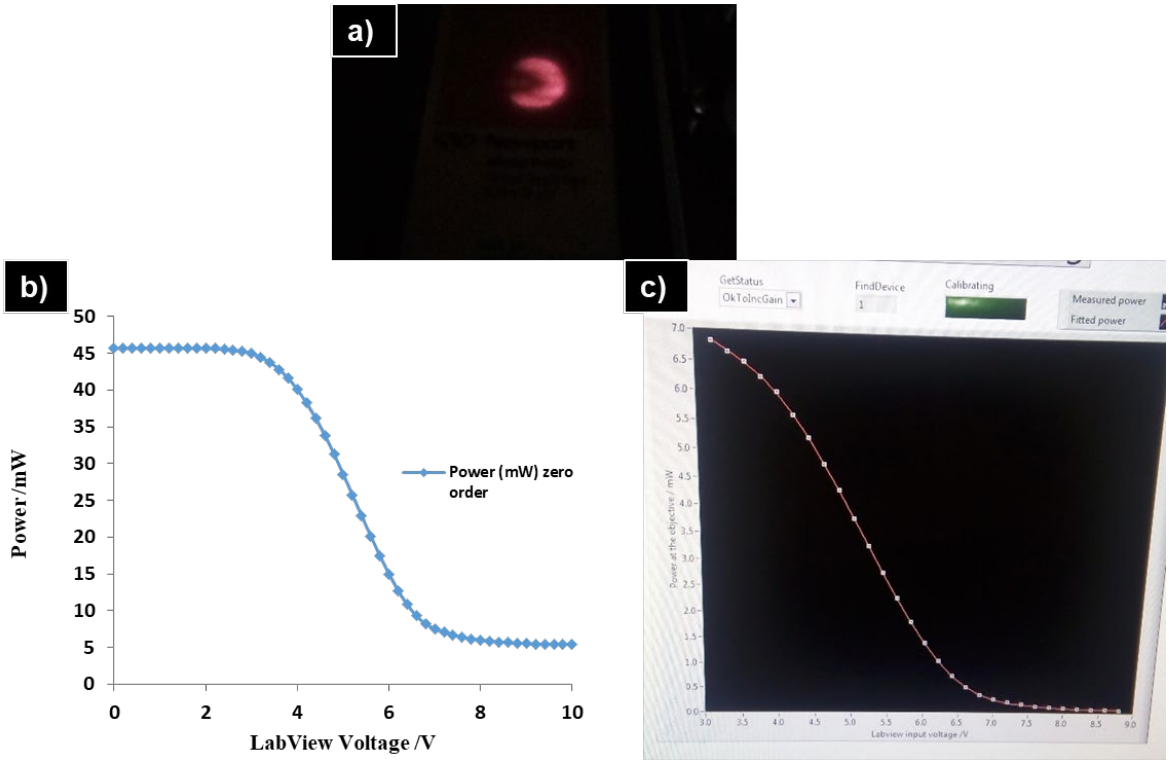

Figure 20. (a). Beam profile of the zero order laser beam filling the back of the objective, (b) Plot between average laser power <P> in units of mW versus LabView commanded voltage for the zero order beam measured at the AOM, (c) calibration plot between average laser power <P> in units of mW versus LabView commanded voltage for the zero order beam measured at the integrating sphere.

The circular zero order beam reaching the objective did not have a uniform profile. There was a dark spot in the middle due to diffraction by the crystal in the AOM. Due to this dark spot the power reaching the objective was low, resulting a 0.44% diffraction range. Figures 20b and 20c shows average laser power <P> in the units of mW versus LabView (V) plots at the detector and at the integrating sphere respectively. Experiments were done to confirm any effect of the dark spot on the fabricated structure. However, it was proved that the fabrication setup was immune to the dark spot.

3.4 Analysis of the fabrication using new MPL system

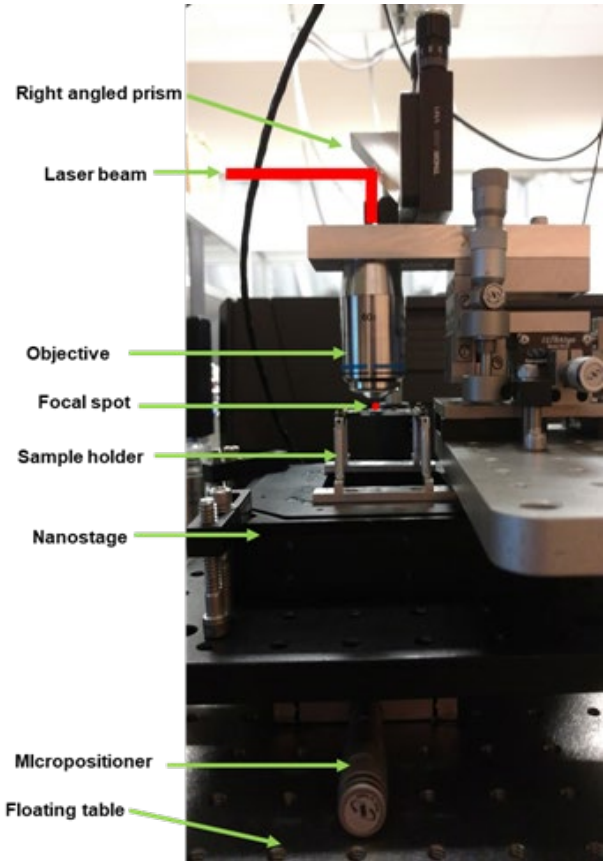

Figure 21. An overall view if the new fabrication setup in which the nanostage was placed closest to the floating table and laser beam was focused on the sample from above.

A close-up view of the new fabrication set-up in which laser beam is focused from the top and stage is close to the floating table is shown in Fig 21. A right angles prism was used to reflect the collimated laser beam at a 90 degree, which will overfill the back of the high NA objective. The objective focuses the beam on the volume of a transparent photoresist. The nanostage was moved in all three axes by using the LabView software which will result in photo patterning of a desired shape. The stage was placed on a *xy* micopositioner, which gives one freedom to move the

sample with respect to the objective. In this section, the first test structure using a IP-Dip photoresist was fabricated and characterized.

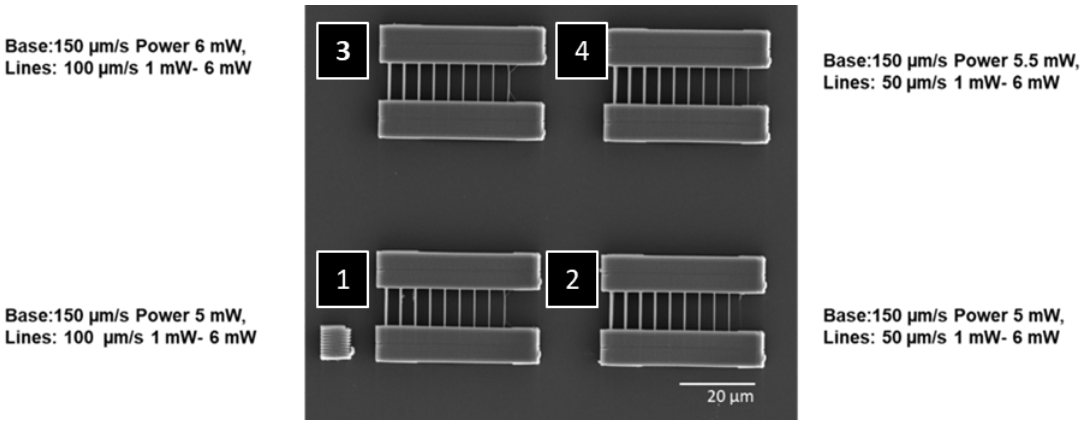

Figure 22. SEM image of the overall test structures fabricated using new MPL system. The fabrication conditions for the structures are specified in the box next to the structures.

Four test structures were fabricated in IP-Dip using the new MPL system. The structures are shown schematically in Fig. 22 Each structure consist of two support blocks with lines drawn in between. The lines span between the structures are used to assess the size and quality of features that can be fabricated as a function of power and scan speed. As these lines are sub-micron in size, they are fabricated between large, robust bases having a base area of 10 µm × 10 µm that holds the lines suspended above the substrate and anchor the entire structure firmly to the supporting substrate. The bases in structures 1 and 2 were fabricated at the scan speed of 150 µm/s and power 5 mW. Followed by bases in the third and fourth structures were also fabricated at a scan speed of 150 µm/s and power 5.5 mW and 6 mW respectively. Thin lines were fabricated at a scan speed 50 µm/s in structures 1 and 3 and at100 µm/s in structures 2 and 4 using power ranging from 1 mW - 6 mW with a gradual increment of 0.5 mW. The lines were 250 nm apart in the *y*-axis and 500 nm in the *z*-axis.

Structures 1 and 2 are in the bottom with a marker on the left and structures 3 and 4 are on the top. In the old MPL setup distortions with 450 nm amplitude were seen in the structures fabricated at 100 µm/s scan speed and 5 mW power. However, in the new MPL the magnified image of a structure shown in Fig. 23 fabricated at 100 µm/s scan speed and 5 mW power show that the lines were fabricated without any distortions in both *x*- and *y*- axes.

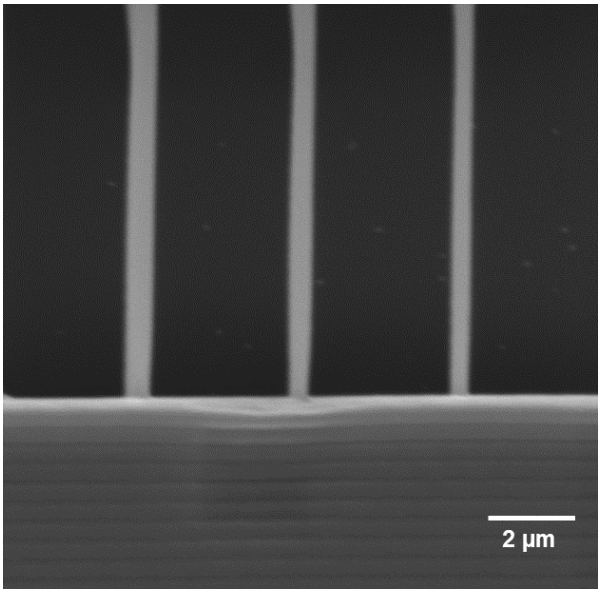

Figure 23. A high resolution SEM image of the first test structure in which the base of fabricated at a scan speed of 150 µm/s and power 5 mW. The lines were fabricated at a scan speed of 50 µm/s and power ranging from 1 mW - 6 mW.

3.5 Improvements with new MPL system

3.5.1 Improvement of resolution

The resulting structures fabricated from the setup described in Section 3.1 were not only wiggle free but they also had better resolution as compared to the old MPL setup. The comparison between the standard structure fabricated in old and new MPL setup is shown in Fig. 24. In the old

MPL setup, the lines at the threshold power (1.5 mW) merge with each other due to uneven shrinkage in the structures. At 2 mW first stable line suspended between the two bases was fabricated with an aspect ratio of 3.26. However, in the new MPL setup at 1.5 mW threshold power stable suspended lines were fabricated with an aspect ratio of 2.62.

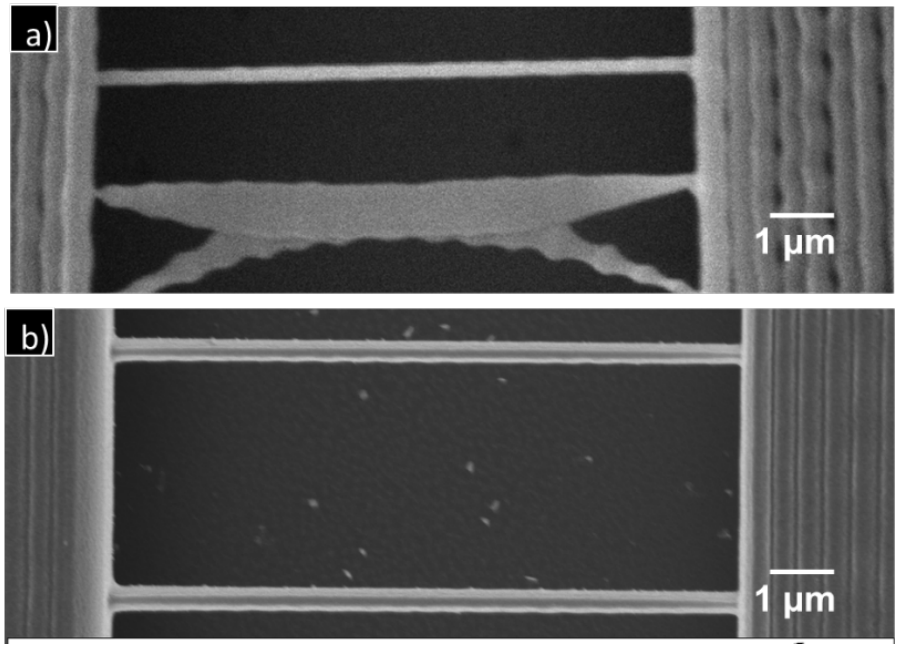

Figure 24. SEM image of the standard structure with lines fabricated at 50 µm/s and 1.5 mW power. (a) The lines at 1.5 mW merged with each other, but the line at 2 mW was successfully fabricated in the old MPL setup, (b) both the lines were fabricated in the new MPL setup

In the new MPL setup the measurement of line height and line width was done by fabricating a set of standard structures as shown in Fig. 25. The lines were fabricated at powers ranging from 1.5 mW to 5 mW with scan speeds of 50 µm/s and 100 µm/s.

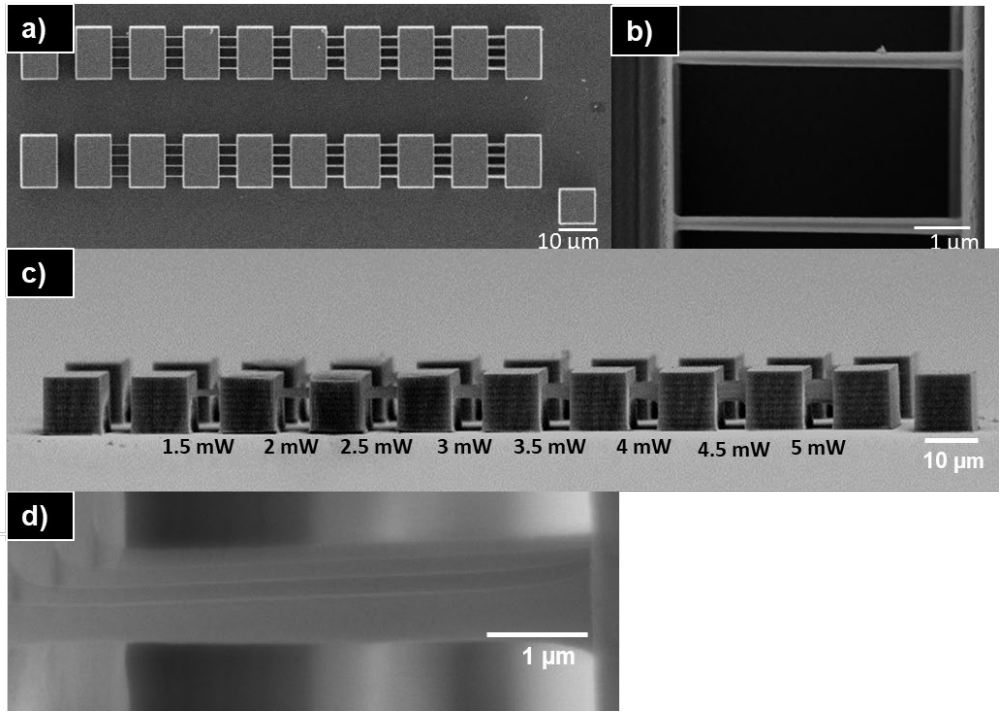

Figure 25. SEM image of the standard structure fabricated to measure the resolution and aspect ratio in the MPL setup, (a) Top view of the lines in between the blocks were fabricated at varying power between 1 mW - 5 mW at a scan speed of 50 µm/s and 100 µm/s, (c) Side view of the fabricated structure, (b, & d) magnified view showing the top and side of the single line.

The thickness and width of the lines were measured using MATLAB image processing tool. Each line was measured at four locations along its length and width and the average and standard deviation was obtained. A summary of the line width and line height of Fig. 25 is shown in Table 3.

Lines up to 150 nm width and ~ 400 nm height were fabricated with an aspect ratio of 2.62 at the threshold power of 1.5 mW. Figure 26 outlines a plot showing the change in line and width thickness versus average laser power <P> in units of mW. All the structures were fabricated at a constant scan speed of 50 µm/s.

Table 3. Shows the line width (µm), the line height (µm) and the aspect ratio of the lines fabricated in IP-Dip at 50 µm/s.

Power (mW)	Line width (µm)	Line height (µm)	Aspect ratio
1.5	0.150 (± 0.008)	0.394 (± 0.064)	2.62
2.0	0.263 (± 0.016)	0.800 (± 0.076)	3.03
2.5	0.323 (± 0.016)	1.01 (± 0.092)	3.14
3.0	0.360 (± 0.021)	1.26 (± 0.102)	3.51
3.5	0.403 (± 0.016)	1.39 (± 0.043)	3.71
4.0	0.446 (± 0.012)	1.49 (± 0.138)	3.52
4.5	0.5 (± 0.016)	1.81 (± 0.143)	4.32
5.0	0.65 (± 0.024)	2.23 (± 0.192)	4.96

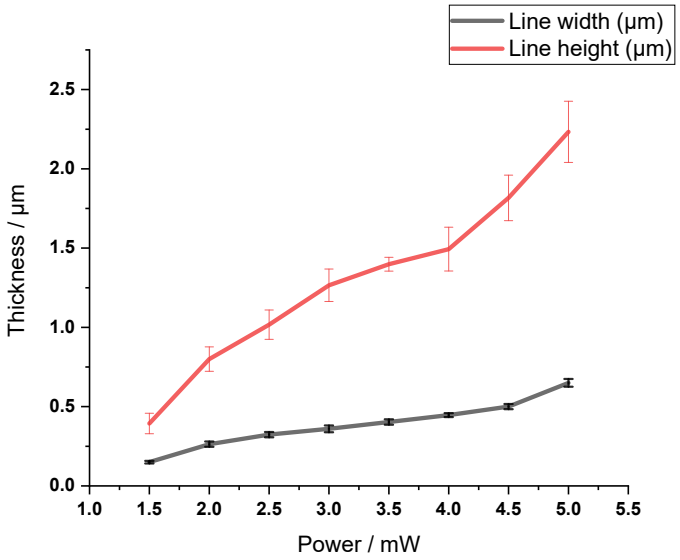

Figure 26. A plot of the line thickness (µm) and the line width (µm) versus average laser power <P> in units of mW for the fabrication at 50 µm/s.

3.5.2 Improvements in consistency of fabrication

In comparison with the old MPL setup, the fabrications in the new MPL setup are also improved in terms of the fabrication consistency. The lines fabricated in the old setup suffered shrinkage of ~ 10% - 17% due to the distortions in the structures. Because, the distortion frequency was always random, it was difficult to achieve day to day or same day consistency in the structures.

The repeatability of the line dimension in the new MPL setup was characterized by taking measurements of a three line array. Each array was fabricated in the same scan speeds and power combinations (50 μm/s, and 1.5 mW – 5 mW). Four line width and four line height measurements were performed on each line set and the average of the line widths and line height was obtained. For a given scan speed and power combination, the maximum variance in the line width and line height were found be in variances of 30 nm and 100 nm, respectively.

The run to run repeatability was confirmed over three different fabrications, performed with the same scan speed (50 μm/s) and power range (1.5 mW – 5 mW), but on different days. The plots in Fig. 27 show the average line width and line height of the structures fabricated in the old MPL setup and the new MPL setup over several days. The line-set averages at one power was further averaged over the three arrays measured in three different samples fabricated on different days. The error bars in the measurements represent the variations in the line dimension on different days. The variations in the line width and line height fabrications in the new MPL were much lower as compared to the old MPL setup. This variation can be seen by the size of the error bars in Fig. 27.

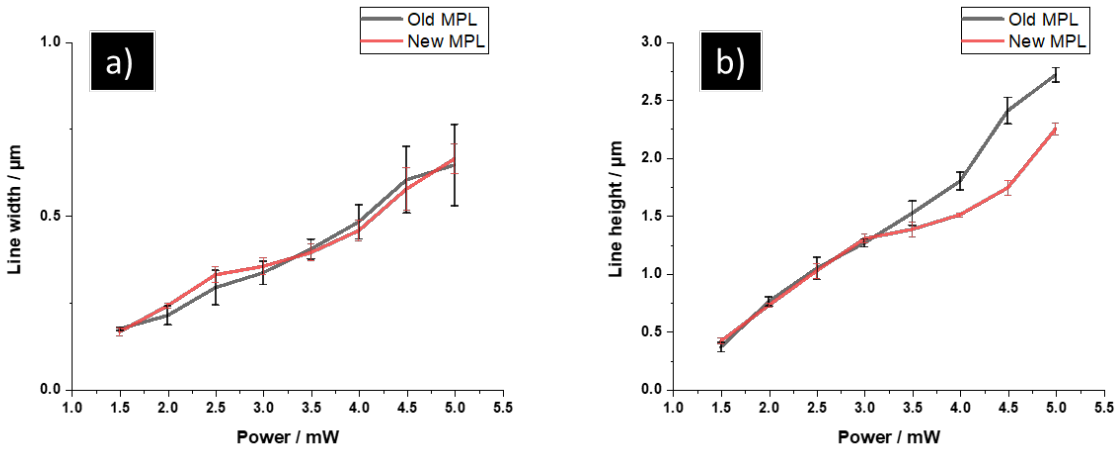

Figure 27. A comparison between the repeatability of the fabrications done in same conditions on three different days using the old MPL setup and the new MPL setup. (a) The line width (µm) versus average laser power <P> in units of mW, (b) The line height (µm) versus average laser power <P> in units of mW.

3.6 Conclusion

In the old MPL system, the nanostage used to be placed on top of the microscope and the sample was placed upside down on the sample holder. This setup was prone to distortions in the structures due to vibrations. Therefore, a new MPL setup was developed. In the new MPL system the whole fabrication set-up was moved 8 cm above the floating table which helped dampen these vibrations. Figure 28 shows the improvements in the fabricated structure by using the new MPL setup.

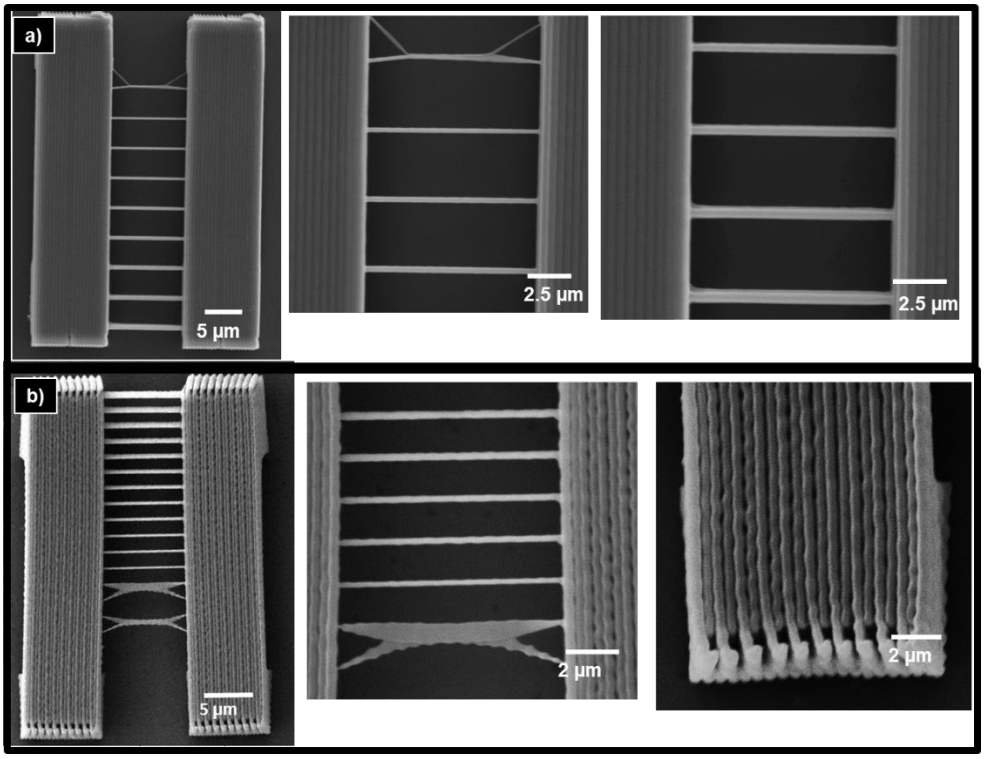

Figure 28. SEM images showing a comparison between structures fabricated via new and old MPL setups. (a) Test structure fabricated with new MPL setup on the floating table. (b) Test structure fabricated with old MPL set up on the microscope.

The resolution of the lines fabricated in the new MPL setup has also been improved. The threshold power at which stable lines were fabricated was reduced from 2.5 mW in the old MPL setup to 1.5 mW in the new MPL setup, which resulted in lines with aspect ratio of 2.62. The consistency in the fabrication was also improved in the new MPL as measured by comparing the lines fabricated on different days.

4. THEORY AND EXPERIMENTAL

4.1 Introduction

Engineering the optical properties of a material is a relatively new field, which has recently evolved due to the use of new techniques and technologies. The ability to design and fabricate materials, whose properties can be varied with the change in the wavelength of incident light opens up an enormous range of technological advancements.[54-55] The propagation of waves through a periodic structure was first studied by Floquet in1884 and Bloch in 1928. In the 1970s, structures were proposed, which can modulate the properties of the light by controlling the spontaneous emission using photonic band gaps.[56] The terms photonic band gap and photonic crystals (PhCs) were first coined by Yablonovich in 1987, when he explored the inhibited spontaneous emissions in solid state physics.[57]

The development of fiber optics has already revolutionized the telecommunication industry. The propagation of light in an optical material with periodicity of the order of optical wavelength is analogous to the propagation of electrons in a periodic lattice. One of the purest examples of any structure which can modulate light propagation is a periodic crystal. However, in the presence of a defect (point or line defect) scattering may occur. The lattice can inhibit propagation of certain waves in some directions, but when the lattice potential difference is strong, it results in the formation of a complete band gap which means photons are forbidden to travel in that region.[58] In order to manipulate light propagation of certain wavelength, PhCs with specific photonic band gaps can be fabricated.

4.2 Wave propagation in photonic crystals

Yablonovich first studied the phenomenon of electromagnetic waves propagating in periodic lattices called PhCs.[57] The initial research explored the possibility of controlling light and wave propagation in simple periodic structures. Nowadays, wave propagation has been studied in more diverse and complex structures like one-dimensional (1D), two-dimensional (2D), and three-dimensional (3D) PhCs shown in Fig. 29.

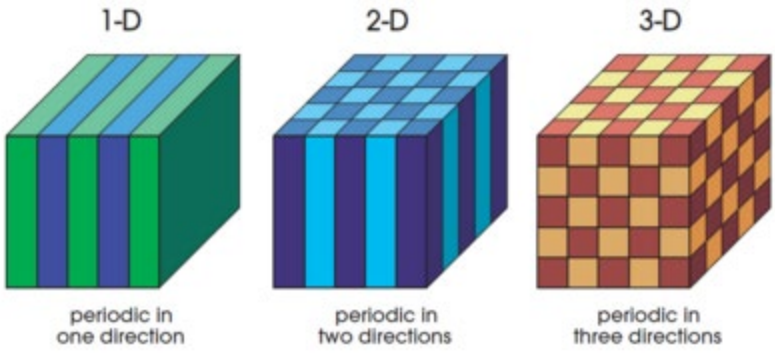

Figure 29. Illustration of 1D, 2D and 3D photonic crystals [59].

The 1D PhC is one of the most straightforward periodic structures in nature. This structure is composed of two materials of different dielectric constants alternatively stacked on top of each other. 1D PhCs can act as a mirror (Bragg mirror) for the light of specific wavelength and the presence of defects in the crystal can result in formation of localized light modes. These properties make 1D PhCs a great candidate to be used in dielectric mirrors and optical filters.[60] It took almost a century to explore the second dimension in PhCs. A 2D PhC is consists of a periodic plane in two dimensions and non-periodic in the third dimension. Many periodic 2D PhCs have been constructed with important applications in guiding and manipulating light.[61-63] 2D PhCs have a photonic band gap in the *xy* plane and it can prevent light propagation in any direction along this plane. The electromagnetic field in a 2D PhC can be divided into TM (transverse magnetic) mode

in which the electric field is in the *xy* plane, and magnetic field is in the *z* plane and TE (transverse electric) mode in which the magnetic field is in the *xy* plane and electric field is in the *z* plane.[64] The band structures of TE and TM modes can be completely different which makes it possible to create a polarization selective bandgap.[59] Light propagation in 3D PhCs is not only most complicated to understand, but they are also most challenging to fabricate via known fabrication techniques. The first design of a 3D PhC consists of diamond lattices positioned on the vertices of a diamond lattice. For 3D PhCs it is difficult to achieve complete photonic band gap. However, some 3D PhCs have been discovered that give significant portions of photonic band gaps. Yablonovite is a PhC structure that has an inverse cylindrical holes arranged in a diamond lattice. Yablonovite was the first complete band gap 3D PhC that was realized in a lab.[65] A micron-scale woodpile structure was the first 3D PhC fabricated in the lab for light at infrared (IR) wavelengths using E-beam lithography.[66]

Wave propagation in a PhC always depends on the length scale of its periodicity, which is proportional to the wavelength of incident light. The study of wave propagation was pioneered by Bloch in 1928. Bloch hypothesized that the electrons in a medium scatter only in the presence of imperfections and defects in the medium. He explained the wave propagation in PhCs (1D, 2D, and 3D) always depends on the four Maxwell equations 4-7,

$$\nabla . \boldsymbol{B} = 0 \tag{6}$$

$$\nabla \times \boldsymbol{E} + \frac{\partial B}{\partial t} = 0 \tag{7}$$

$$\nabla . \boldsymbol{D} = \rho \tag{8}$$

$$\nabla \times \boldsymbol{H} + \frac{\partial D}{\partial t} = J \tag{9}$$

where $\boldsymbol{E}$ and $\boldsymbol{H}$ are macroscopic electric and magnetic fields, $\boldsymbol{D}$ and $\boldsymbol{B}$ are displacement and magnetic field, and ρ and J are the free charge and current densities, respectively.[59] For a linear, isotropic medium, the macroscopic quantities $\boldsymbol{E}$ and $\boldsymbol{H}$ are related to $\boldsymbol{D}$ and $\boldsymbol{B}$, respectively as shown in equations 10 and 11,

$$\boldsymbol{D} = \varepsilon_r \varepsilon_0 \boldsymbol{E} \tag{10}$$

$$\boldsymbol{B} = \mu_r \mu_0 \boldsymbol{H} \tag{11}$$

where μ_0 and ε_0 are the permeability and permittivity of free space and μ_r and ε_r are relative permeability and permittivity of the material. By substituting equations 10 and 11 in Maxwell's equations (6-10) and solving for the wave equation, we can get a simplified version of the wave equation shown in equation 12.[67]

$$\nabla^2 \boldsymbol{E} = \frac{1}{v^2} \frac{\partial^2 \boldsymbol{E}}{\partial^2 t} \tag{12}$$

where ∇ is the eigen operator and v is the speed of wave propagation in the medium. This wave equation is devoid of a length scale. Changing the size of the PhCs does not affect the solution, but it will change the frequencies by a certain factor, this phenomenon is called the principle of electromagnetic scalability.

4.3 Self-collimation and spatially varied lattices

Self-collimation in PhCs is a phenomenon in which the wave propagates in the crystal without any diffraction.[68-69] Witzens in 2002 performed the first theoretical investigation of self-collimation in planar PhCs.[70] During self-collimation, sudden changes in wave propagation can be

observed in PhCs fabricated by ordinary isotropic materials. The extent of self-collimation in a crystal was measured via isofrequency contours (IFCs).

IFCs are dispersion surfaces in *k*-space which give the magnitude of the wave vector |**k**| as a function of direction through the lattice.[71] IFCs are a cross-section of the dispersion surface, which provides essential information about the PhC behavior at a specific frequency. In a PhC, the IFCs usually take the shape of the Brillouin zone, which is mostly non-ellipsoidal. Analysis of IFCs can help predict important relationships between phase and power in a crystal. To observe self-collimation in a crystal, a flat IFC is important because the waves can only propagate normal to the surface in the flat region of IFC. Figure 30 shows a schematic illustration of an IFC in which the self-collimation is observed when the incoming beam frequency matches the flat IFC frequency. SVPCs are a class of aperiodic lattice, in this case the orientation of the unit cells is spatially varied, forcing light to turn through 90 degrees via self-collimation.[72]

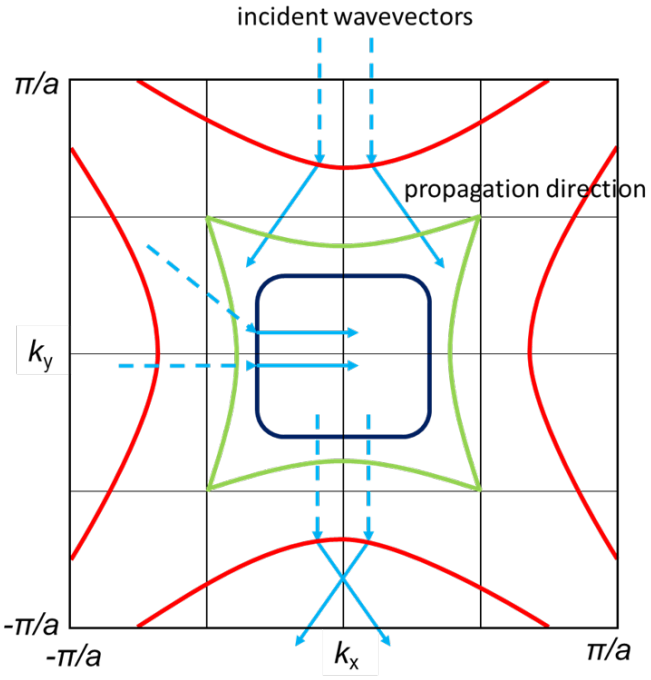

Figure 30. Schematic illustration of an isofrequency contour showing the direction of beam propagation (*solid arrow*) in real space depending on the curvature of the isofrequency contour where the incoming wave vector (*dashed arrow*) is incident.[37]

Rumpf *et al.* first demonstrated the theoretical calculations for the spatial variations of the unit cell in a PhC.[72-73] The IFC of the unit cell was calculated via the plane wave expansion method by defining the lattice spacing, the refractive index of the medium, the refractive index of the surroundings, and the angular orientation of the unit cells. The unit cell was decomposed into spatial harmonics, which were composed of three planar gratings shown in equations 12-14,

$$\boldsymbol{K}_x = \frac{2\pi}{\Lambda_x}\,\boldsymbol{x} \tag{12}$$

$$\boldsymbol{K}_y = \frac{2\pi}{\Lambda_y}\,\boldsymbol{y} \tag{13}$$

$$\boldsymbol{K}_z = \frac{2\pi}{\Lambda_z}\,\boldsymbol{z} \tag{14}$$

and the complex amplitude shown in equation 15,

$$a_{pqz} = FFT_{3D}[\varepsilon_{uc}(x, y, z)] \tag{15}$$

where Λ is the lattice spacing in x-, y-, and z- direction. By varying the individual spatial harmonics of each unit cell in the uniform crystal, the light was forced to turn 90-degrees. A calculated IFC showing beam collimation in the flat region with a unit cell with 30% fill factor and a 3D SVPC is shown in Fig. 31. Rumpf *et al.* first fabricated a SVPC by 3D printing (Stratasys FDM 400 mc).[73] They used a polycarbonate-ABS blend material with a dielectric constant of ε = 2.45 at 15 GHz and fabricated SVPC by using fused deposition modeling.

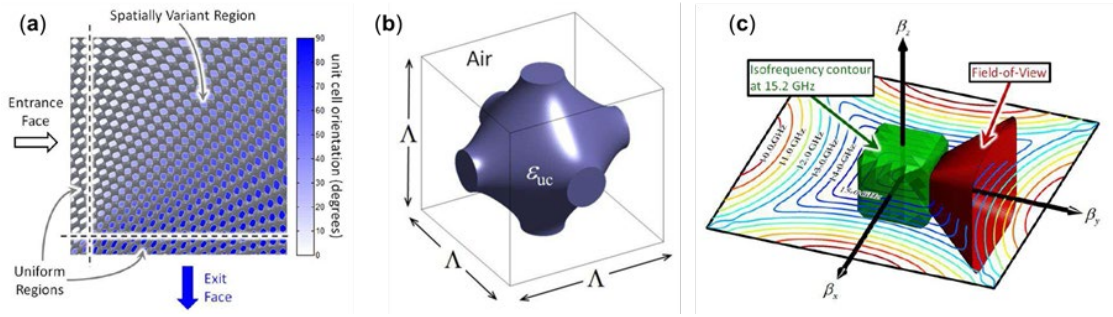

Figure 31. a). Synthesized 3D SVPC that bends light at 90 degrees in the microwave region superimposed on top its orientation function, (b) its corresponding unit cell with 30% fill-factor, and (c) the isofrequency contour (IFC) of the unit cell with superimposed field-of-view.[74]

The field of view (FOV) in the k-space is the region where the k-vectors are parallel to within 8.7 degree. In Fig. 31c the square cone enclosing the IFC represents the FOV, which was 52.5 degree. In order to experimentally measure the beam bending, the SVPC was illuminated by a standard gain horn antenna (12 GHz – 18 GHz) on the input side. The output from the SVPC was measured on the three sides of the crystal by scanning a small monopole antenna around the

perimeter of the device and monitoring the signal. From the measurement, it was shown that the 3D printed SVPC was bending the beam with 6.5% fractional bandwidth with a 20 dB fluctuation in the bent beam side. The characterization setup of the SVPC and the field profile measurement is shown in Fig. 32.

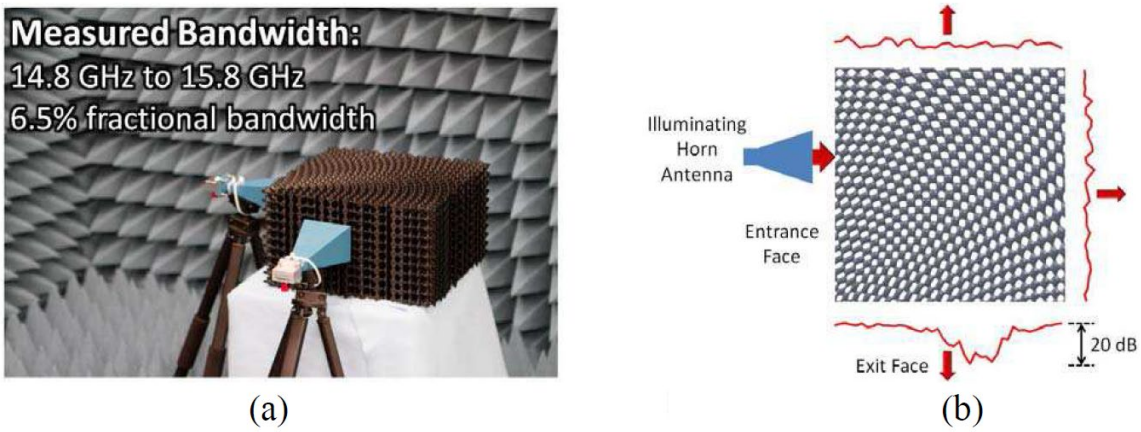

Figure 32. (a) The experimental setup and the SVPC fabricated via 3D printing for measurement at 15 GHz with the corresponding (b) field profile result around the SVPC.[74]

To explore the beam bending at optical frequencies in SVPCs, the lattice spacing and the spatial orientation of the unit cell were scaled down based on the low refractive index materials used for fabrication. The first SVPC using a low refractive index photoresist SU-8 2075 was fabricated by MPL.[23] The SVPC was characterized by using an Er:YAG laser at 2.94 μm. The laser beam was shined on the input face using an optical fiber (Thorlabs, 1550BHP, 9 μm core) and the output was measured on the three sides by scanning the optical fibers and detecting the signal using PbSe detectors (Thorlabs, PDA20H). The experimental characterization shows that a SVPC with a 50% fill factor was able to bend light with a power efficiency of 8%. The beam profile of the SVPC characterization is shown in Fig. 33.

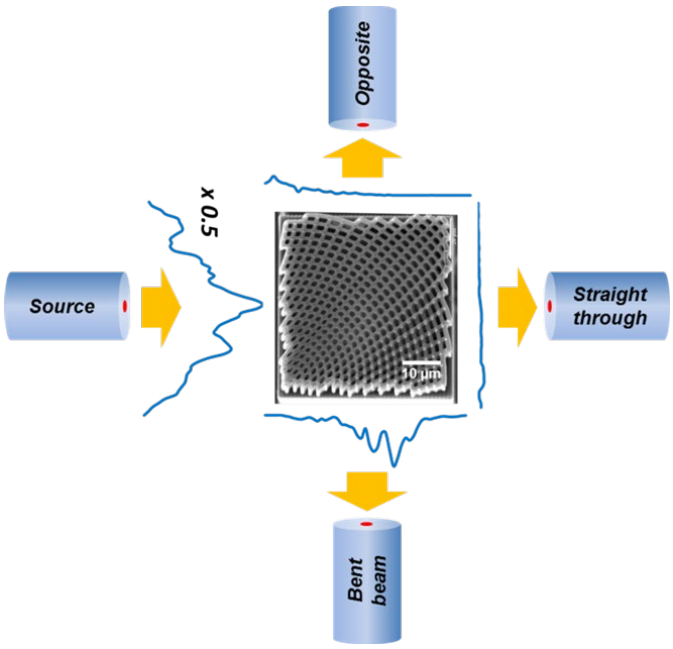

Figure 33. Beam profile of SVPC characterized by at 2.94 µm. Source fiber is the input beam, and the signal at the three faces was measured by a PbSe detector.[37]

4.4 Experimental Methods

4.4.1 Substrate preparation

Careful MPL sample preparation is necessary to achieve functional PhCs. One of the most critical steps is the preparation of a clean substrate (borosilicate microscope slide, Thermo-scientific). A thoroughly cleaned substrate leads to consistent and repeatable fabrications. The Steps for cleaning are as follows:

1. Cut the glass slide to the required dimension (approx. 19 mm by 19 mm).
2. Sonicate the glass slides for 30 minutes in water at 50 °C.
3. Rinse the slide with deionized (DI) water.

4. Soak the glass slides in 1 M aqueous potassium hydroxide (KOH) for 30 minutes.
5. Rinse the glass slides with DI water and dry in air for 30 minutes.
6. Dry in oven at 100 °C until used.

4.4.2 Preparation of adhesion layer

The SU-8 2075 (MicroChem, 73.5 wt% solid) is an epoxy-based negative photoresist consisting of an epoxide-functionalized bisphenol A oligomer (SU-8, CAS 28906-96-9), two photoacid generators triarylsulfonium hexafluoroantimonate, (CAS 89452-37-9) and 4-thiophenyl phenyl diphenyl sulfonium hexafluoroantimonate (CAS 71449-78-0) in a solvent comprised of cyclopentanone (CAS 120-92-3), and a plasticizer propylene carbonate (CAS 108-32-7).

An adhesion layer was spin coated on the substrate using a diluted SU-8 2075 solution. The photoresist SU-8 (73.5 wt% solid) was diluted by cyclopentanone (CAS 120-92-3) to make a 52 wt% solution using equation 15.

$$W_c = \frac{W_0(S_0 - S_1)}{S_1} \tag{15}$$

where W_c is the weight of the cyclopentanone, W_0 is the weight of the SU-8 2075, S_1 is the final wt% of the diluted SU-8 and S_0 is the initial wt% of the SU-8 2075. The SU-8 2075 and cyclopentanone were added in a scintillation vial and mixed until all the SU-8 dissolved in cyclopentanone. The diluted SU-8 solution (~ 1 mL) was spin coated (Specialty Coating System G3P-8) on a clean glass substrate by using the procedure outlined in Table 4. The spin coating resulted in a 5 μm – 8 μm thick layer of SU-8. The sample was pre-baked for 1 minute at 65 °C followed by 6 minutes at 95 °C. The sample was exposed to ultraviolet (UV) radiation using a

flood exposure assembly (Loctite ZETA 7411-5, 400 W metal halide lamp, 315 nm – 400 nm) for 2 minutes. Next, the sample was post-baked for 1 minute at 65 °C followed by 9 minutes at 95 °C. The entire procedure was performed in a dark room.

Table 4. Spin coating recipe in SCS-G3P to create a thin layer for MPL.

Step no.	**Ramp-time / s**	**Revolution / min**	**Dwell-time / s**
0	0	0	0
1	5	500	5
2	20	6000	10

4.4.3 Sample preparation for SU-8 waveguides

To provide a medium in which the waveguides will be fabricated, a thick layer of SU-8 2075 (150 µm – 170 µm) was spin coated on the pre-coated adhesion layer. Undiluted SU-8 2075 was dispensed (1 mL) on the substrate and spin-coated using recipe shown in Table 5. The layer was pre-baked for 5 minutes at 65 °C and 40 minutes at 95 °C. The sample was cooled for at least 30 minutes before laser exposure.

Table 5. Spin coating recipe in SCS-G3P to create a thick layer of SU-8 for MPL.

Step no.	**Ramp-time / s**	**Revolution / min**	**Dwell-time / s**
0	0	0	0
1	5	500	5
2	4.7	1400	26

4.4.4 Fabrication of SU-8 waveguides by Old MPL setup

Using the old MPL setup, curved and straight waveguides were fabricated in SU-8 2075. The output from a Ti:sapphire laser was routed to the sample by using the optical set up shown in Fig. 4. The beam was passed through a beam splitter (BS) and then a half-wave plate/polarizer combination, which changes the polarization of the beam from horizontal to vertical and also acts as an attenuator to adjust the optical power reaching the sample. A portion of the beam was directed to a frequency resolved optical grating to measure the pulse duration of the beam. The transmitted beam from the BS is detected by a photodiode (PD, Thorlabs Det210), which reads the attenuated signal from the half wave plate/ polarizer combination. The reflected beam then passes through an AOM, which automates the power control during fabrication. The beam then passes through the periscope and then expanded and collimated by using a lens telescope system. The collimated beam overfills the back of the objective 60x / 1.4 NA objective (Nikon Type A oil, n = 1.51 at 800 nm) and focuses the beam on the sample.

The sample with a 160 μm thick layer of SU-8 was fixed on the sample holder using a double-sided carbon tape. A drop of index matching oil (Nikon immersion oil type A, n = 1.51) was placed on the center of the objective. The microscope objective was then raised up until the oil just touched the SU-8 surface. A cross section of the irradiance profile of the laser beam was observed via back-reflected light from the SU-8/oil interface. The back-reflected beam was observed via CCD camera on the computer using ImagePro software. The objective was raised further using the fine tuning knob until a sharp focus was observed. At the sharpest focus, the SU-8/glass interface is in the focal plane of the laser beam. A stage leveling program (LabView VI) was used for further adjustment. In this VI, the stage was moved in the z-axis until maximum pixel intensities were observed by CCD camera. For consistent fabrication results, the laser beam was buried 3 μm in the SU-8/glass interface. For fabrication, the AOM power was calibrated using an integrating sphere between 0.3 mW – 5.2 mW and the waveguides were fabricated on top of a 100 μm tall pillar also fabricated by SU-8.

The polymerization in SU-8 photoresist continues even after the laser exposure stops. Since, the SU-8 polymerizes by diffusion of PAGs, the sample was post-baked for10 minutes at 65 ºC followed by 30 minutes at 95 ºC on a hotplate. After post-baking the sample was placed in a beaker and immersed in Propylene glycol monomethyl ether acetate (PGMEA), which dissolved all the unexposed SU-8 resist. Washing with PGMEA was performed four times (30 min each wash) to ensure all the unreacted resist is dissolved. After that the sample was immersed in isopropyl alcohol (IPA) once for 5 minutes, then the sample was immersed in DI water once for 5 minutes. Finally, the sample was left in the air to dry. Figure 34 shows the optical transmission images of the fabricated curved waveguides of R_{bend} (19 μm and 38 μm) and the straight 50 μm long waveguide.

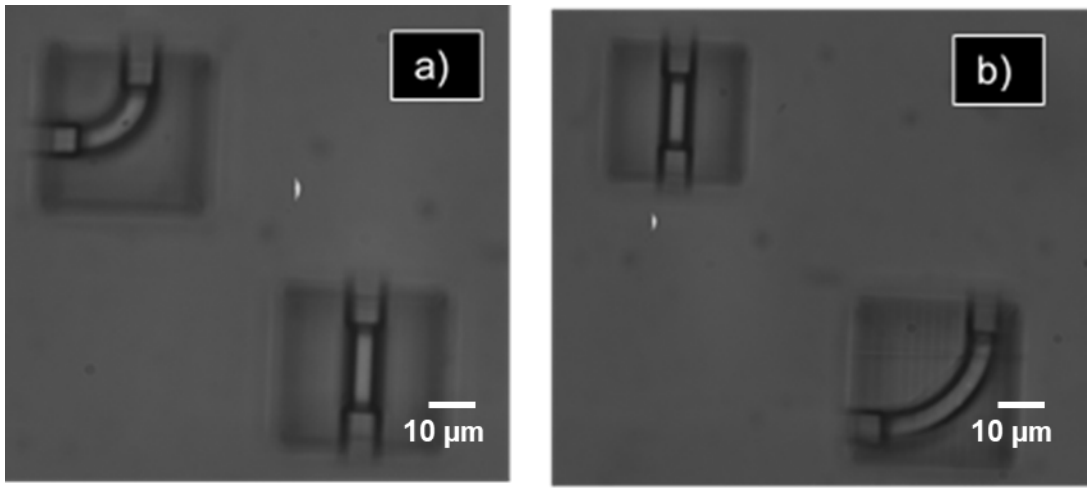

Figure 34. An optical transmission image of (a) a 19 µm curved (upper left) and a 50 µm straight (lower right) waveguide, (b) the exact same 50 µm straight waveguide with a 38 µm curved waveguide.

4.4.5 Fabrication of uniform lattices in IP-Dip using the modified MPL setup

The glass slide (19 mm × 19 mm) coated with thin layer of adhesion SU-8 was used as a substrate for uniform lattice fabrication using IP-Dip photoresist. Uniform lattices were fabricated using the modified MPL setup, where the nanostage was placed close to the floating table to avoid wiggle formation present in previous fabrications. The optical setup is shown in Fig. 10 was used for fabrication in IP-Dip.

IP-Dip is a high-resolution photoresist with a refractive index of 1.51. It serves both as a photoresist and an index matching liquid during fabrication. The substrate was attached to the sample holder with double-sided carbon tape and placed on the nanostage. A drop of IP-Dip was placed on the tip of the objective, and it was screwed upside down on the nanostage. A close-up

of the real-time fabrication assembly is shown in Fig. 21. The laser beam overfilled the back of the 60x / 1.4 NA objective (Nikon Type A oil, n= 1.51 at 800 nm).

The objective was moved down using the micro-positioner until the IP-Dip just touches the SU-8 adhesion layer and the back-reflected light was viewed on the computer via CCD camera. The objective was moved further down by slowly using the nanostage until a sharp focus was visible. At this point, the LabView sub VI was used to move the stage up and down to reach a position where the pixel intensity is maximum. The CCD saturates at the pixel intensity of 4095 therefore neutral density (ND) filters were placed in front of the camera to achieve the highest pixel intensity at a given point. The fabrication begins at the SU-8/IP-Dip interface, when the objective was moved downwards towards the sample. The uniform lattices were also fabricated on top of 100 μm tall pillar with a 10 μm central post supporting the crystal.

After laser exposure, the sample was removed from the fabrication setup and placed in the development assembly shown in Fig. 35. The sample was placed in the center of the funnel and the filled with PGMEA. The sample was immersed in PGMEA for 30 minutes (repeated four times), followed by IPA wash for 5 minutes, and lastly washed with DI water for 5 minutes.

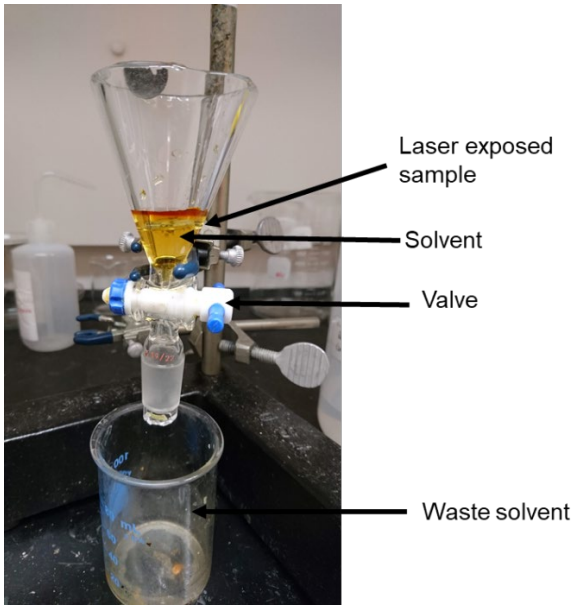

Figure 35. MPL development assembly.

4.5 Optical characterization

4.5.1 Optical fibers cleaving and etching

When optically characterizing waveguides and uniform lattices, optical fibers were used to shine light on the input face of the structures. These fibers were first etched to reduce the cladding diameter in relation to the size of the waveguide or uniform lattice. The steps involved in cleaving the ends of the fiber are described below.

i. Approximately 30 cm of fiber was cut from the spool. The two ends of the fiber (~2 cm) were soaked in acetone for 5 minutes. Acetone results in swelling of the acrylate jacket which was then pulled off carefully by hand.

ii. The stripped end of the fiber was taped on the workbench leaving few mm unexposed. By stretching the loose end of the fiber, the secured end was scribed with a fiber cleaver with just enough force to cleave it without breaking.

iii. A drop of water was placed on the scribed area and the fiber was pulled by pressing the scribed end with a finger.

iv. The cleaved fiber was inspected using a Nikon microscope.

v. The other end of the fiber was also cleaved following the steps (ii-iv).

To etch the diameter of the cladding to reach approximately the same size as the structure the fiber was treated with buffered oxide etch (BOE, J. T. Baker). The center of the 30 cm fiber was again submerged in acetone (~ 3 cm) for 5 minutes and the jacket was carefully removed from the center of the fiber. The exposed part of the fiber was then placed in an etching tube (6 cm) created by cutting a hole in a plastic pipette. The fiber was inserted in the tube such that the stripped center of the fiber is aligned under the hole of the tube. The fiber ends on both sides were secured with tape to prevent any shift in fiber position during etching. The tube was filled with 2-3 drops BOE so that stripped section of the fiber was submerged in BOE as shown in Fig. 36. The fiber was left in BOE for 8 hrs. After etching, the fiber was pulled out of the tube and rinsed with a drop of water. The fiber was placed in a fiber cleaver made in-house by Digaum[37] as shown in Fig. 36c and d.

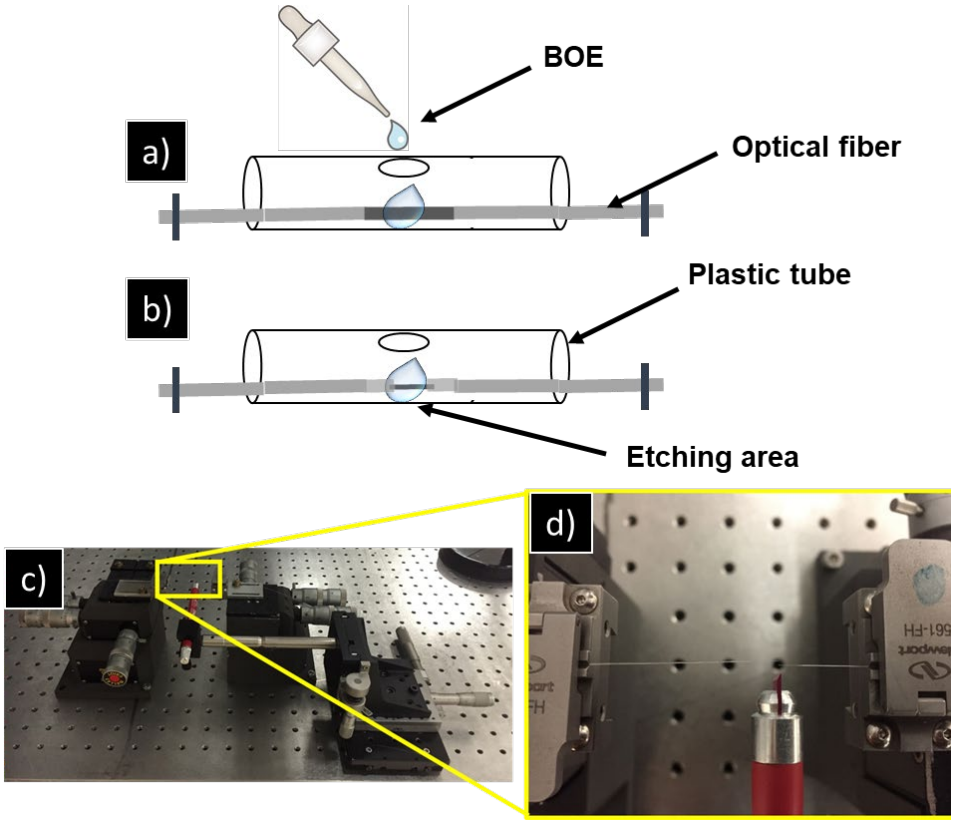

Figure 36. The etching of an optical fiber. (a) The optical fiber was stripped at-the center and placed in a plastic tube with the stripped part directly under the opening, (b) the etched fiber after 8 hrs, (c) the in house setup made for cleaving fiber, and the (d) magnified view of the fiber cleaving system with an etched fiber in position.

The etched fiber was placed in the fiber cleaving setup. Tension was applied from both the sides by translating the stages in *x*-axis. When the fiber was stretched the cleaver was brought closer to the fiber in *y*- axis and then moved up and down until the fiber cleaves. The SEM images of the front and side view of the cleave fiber is shown in Fig. 37.

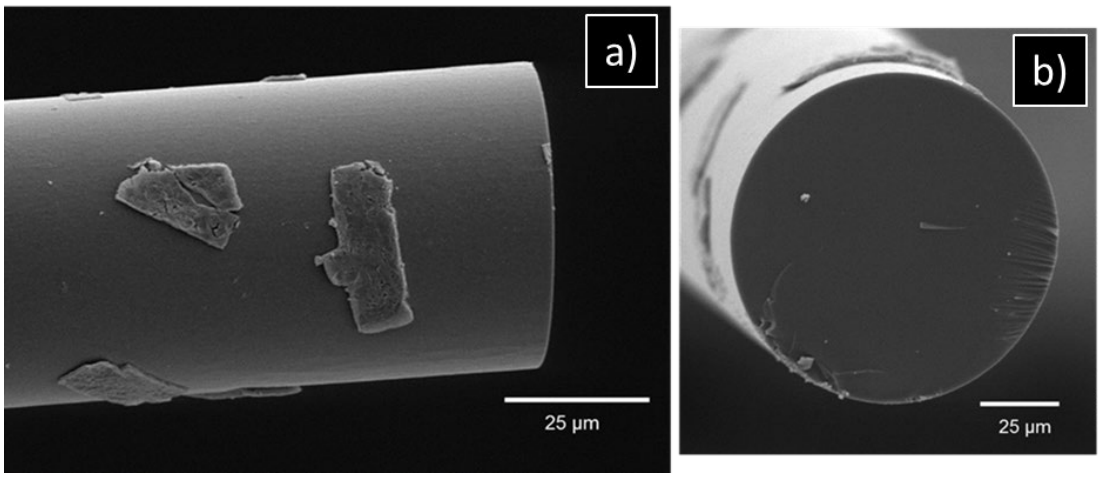

Figure 37. SEM image of the (a) Side view, (b) front view of the etched and cleaved fiber. [23].

4.5.2 Characterization of waveguides using Er:YAG laser

An Er:YAG laser (Premier Laser, $\lambda_0 =$ 2.94 µm, 15 mJ/pulses, 10 Hz repetition rate, and 170 µs pulse duration) was used to characterize curved and straight waveguides. The output of the laser beam was vertically polarized using a wire grid polarizer (Specac GS57010, BaF_2 substrate). The laser beam was defined to be vertically polarized when the electric field was perpendicular to the optical table. The vertically polarized beam was coupled directly into the source fiber using a coupling objective. The optical behavior of the waveguides was compared to the beam bending in SVPC, which can bend vertically polarized beam but not the horizontally polarized beam as shown in Fig. 33. Thus, the waveguides were optically characterized only with vertically polarized beam and the output intensity was measured with the bent fiber in curved waveguides and straight fiber in straight waveguide. In the optical setup shown in Fig. 38, the Er:YAG laser beam was aligned directly into the coupling objective and the waveguides were characterized using the straight and

bent fibers. For shot to shot fluctuations the signal measured at the straight and bent fiber was normalized with the reference detector.

4.5.3 Characterization of uniform lattices

The optical behavior of the uniform lattices fabricated via MPL was measured using an in-house optical characterization setup shown in Fig. 38. An amplified femtosecond laser (AFS) was used to characterize the uniform lattices at λ_0 = 1.55 μm. The system consists of a femtosecond laser amplifier (Coherent legend) which pumps two optical parametric generators (OPGs). The laser output was tunable from 250 nm – 10 μm. Only one of the OPGs was used for this measurement. The laser beam was routed through an optical filter which blocks all the wavelengths less than 1 μm to the optical setup. This setup was designed to guide three beams (i) the main laser beam, (ii) the zero order diffracted beam and (iii) the first order diffracted beam to mirror M9 where they follow the same path and are coupled into the objective.

i. **Main beam** - The AFS laser beam was routed through an aperture to Mirror M1 which was mounted on a flip mount and guided to M2, M3 and finally reaching M9. The main beam was used as a standard for optical alignment and a reference for maximum output measured by a straight fiber.
ii. **Zero order diffracted beam** - M1 was moved out of the way using the flip mount and the laser beam was routed to an optical grating (groove density = 300 g/mm, blaze = 30 μm). The zero order diffracted beam from the grating was routed to M5, M6 (flip mount) and then to M9. The zero order beam was used for broad bandwidth characterization of structures, since it was not widely dispersed.

iii. **First order diffracted beam** - The first order diffracted beam from the grating was routed to M4 and reflected back to the grating, which resulted in further dispersion of the beam. The dispersed beam was passed through an aperture and reaches M7, M8 (flip mount) and then to M9. The aperture and M7 were mounted on an *x*-axis translational stage, which was moved to select wavelength and reduce the bandwidth to 10 nm. To measure the bandwidth, the laser beam was scattered using a beam block and detected by a NIR spectrometer (Oceanoptics, NIRQuest512-2.2 NIR).

The laser beam was routed from M9 through a half waveplate (Thorlabs, Ø1" Multi-Order Half-Wave Plate, SM1-Threaded Mount, 1550 nm) and next through a polarizer to control the polarization and power of the laser beam reaching the sample. A glass slide (Corning) was used as a beam splitter, and a fraction of laser beam was reflected towards the reference detector. The transmitted beam was coupled into the objective. One end of the source optical fiber was aligned at the focus of the coupling objective, while the other end, which was etched to match the size of the structure was placed near the input end of the structure. The fibers were held in place by using a teflon lined chuck mounted on a three axis translation stage. The laser beam coupled into the source fiber was shined on the structure, which was placed on a three-axis translation stage. Etched output fibers were connected on two sides of the structure and the output signal was measured by PbSe detectors. The output end of the fiber was connected to the detector by a fiber connector (SMA 905), which provided consistency in the measurements. The output signal from the IR detector was displayed on an oscilloscope (1 MΩ input impedance). The signal was normalized against that from the reference detector to remove shot-to-shot fluctuations from the laser.

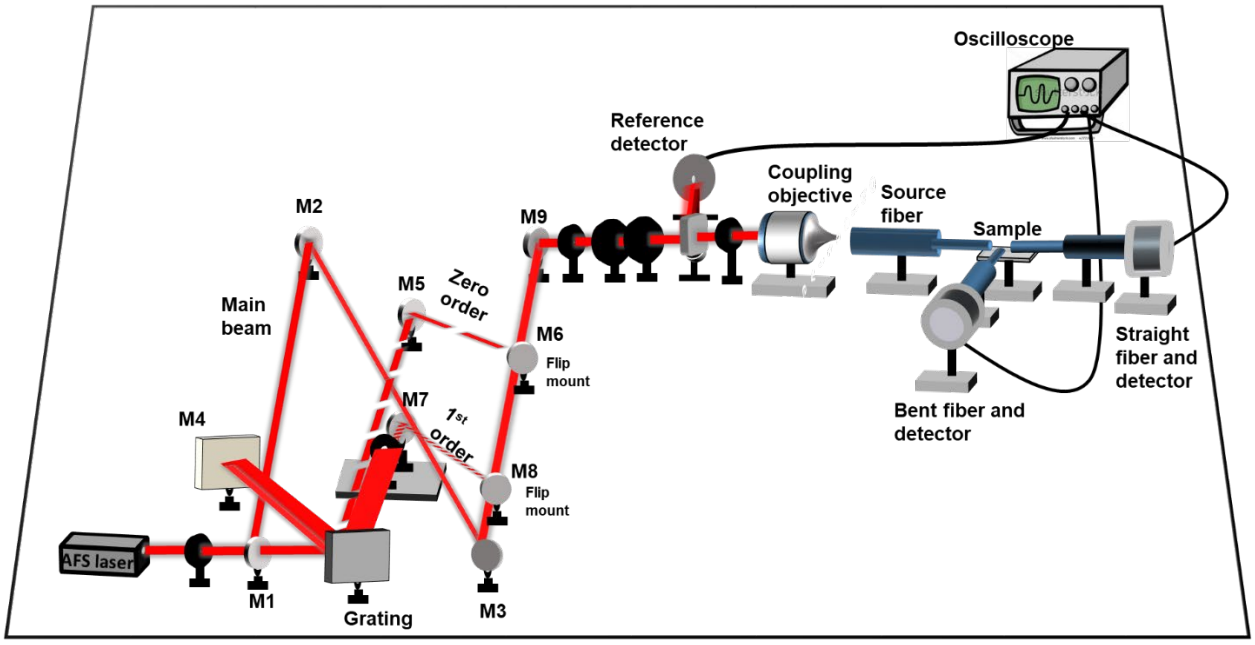

Figure 38. Characterization setup developed to measure the optical behavior of uniform lattices at $\lambda_0 = 1.55$ µm. For the characterization of waveguides at $\lambda_0 = 2.94$ µm, the laser beam was coupled directly into the coupling objective with a different optical setup between the laser and the coupling objective.

4.5.4 Calibration of PbSe detectors

In the optical characterization setup, three IR detectors were used (i) as reference detector (Ref.) before the beam enters the coupling objective, (ii) a straight detector (Det. 2) which is connected to the straight fiber and (iii) a bent beam detector (Det. 3) connected to the bent beam fiber for beam bending measurements in waveguides. These detectors were calibrated with respect to each other using the optical setup shown in the Fig. 39.

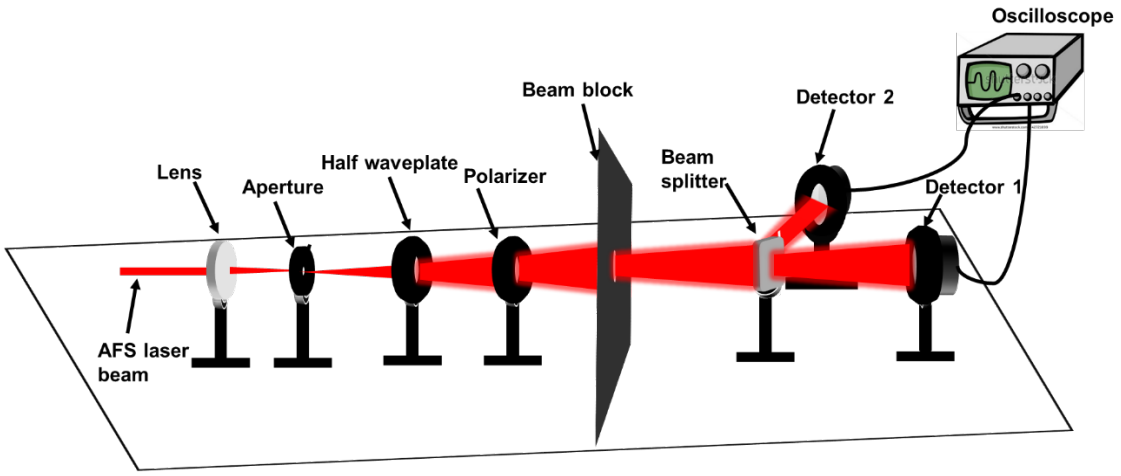

Figure 39. The optical set up to calculate the sensitivity factor of the IR detectors (PbSe) for the optical characterization of 3D structures with AFS laser.

The AFS laser beam (λ_0 = 1.55 μm) was guided through a concave lens (f = 150 mm) and an aperture, which was placed at its focus to control the size of the beam. After the beam passes through the pinhole it started to diverge and the center of the diverged beam was passed through a half waveplate/polarizer combination. The half waveplate/polarizer combination was used to control the polarization and power reaching the detector. A beam block made with black paper was placed at the end of the half waveplate/polarizer combination in order to prevent the scattered beam reaching the detectors. A piece of glass (borosilicate glass from Corning) was used as a beam splitter (BS) and placed at center of the diverged beam. A detector was placed on a three-axis translational stage at the center of the transmitted beam, a second detector was also placed on another three-axis translational stage at the center of the reflected beam. Both the detectors were placed exactly the same distance from the BS, and the position of the detectors was fixed by fine tuning the three-axis translation stage until no change in signal was observed by the detectors. To measure the signal in voltage (V), the detectors were

connected to an oscilloscope. The power reaching the detectors was controlled by rotating the polarizer from 0 degree to 90 degree. The splitting ratio of the BS is given by equation 16,

$$Splitting\ ratio = \frac{B}{A} \tag{16}$$

where A is the percentage of light transmitted towards Det. 1 and B is percentage of the light reflected towards Det.2. The splitting ratio of the BS was used to calculate the calibration factor for the detectors with equation 17,

$$C_1 = \frac{Bb}{Aa} \tag{17}$$

where a and b are the sensitivity factors for Det. 1 and Det. 2 respectively. After measuring C_1, the positions of the detectors were switched with one another. In this case, Det. 2 was placed in the path of the transmitted beam and Det. 1 was placed in the path of the reflected beam. The signal was measured in the two detectors by rotating the polarizer from 0° to 90° and C_2 was calculated by using equation 18.

$$C_2 = \frac{Ba}{Ab} \tag{18}$$

The ratio between equations 17 and 18 gives the calibration ratio between Det. 1 and Det.2 given by equation 19.

$$\sqrt{\frac{C_1}{C_2}} = \frac{b}{a} \tag{19}$$

The relationship between (i) Ref. and Det. 2, (ii) Ref. and Det. 3 and (iii) Det. 2 and Det.3, three sets of experiments were performed using the setup shown in Fig. 39. The signal voltage (V) observed by the detectors was plotted as shown in Fig. 40. The two plots show a linear relationship between Ref. and Det. 3 before and after switching the position of the detectors between the transmitted and reflected beams. The sensitivity ratio (b/a) of Ref. and Det. 3 was calculated using equation 19 where C_1 and C_2 are the slopes of the plots shown in Fig. 40. The sensitivity ratio between Ref.: Det. 2 and Det. 2: Det.3 was also calculated by repeating the procedure. The final results show that both Det. 2 and Det. 3 are equally sensitive to each other but Ref. was 4 times less sensitive than both Det. 2 and Det. 3.

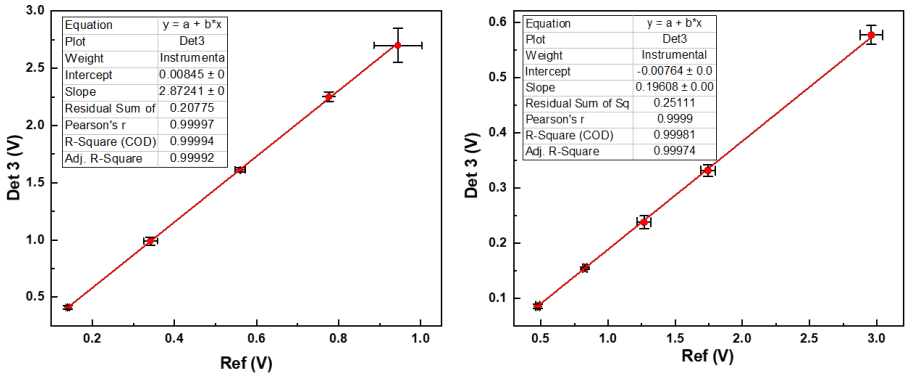

Figure 40. Plots are showing a relationship between the Ref. and Det. 3. The straight line in the plot shows a gradual increase in signal when the half waveplate is fixed and the power is controlled by moving the polarizer from 0° to 90°.

Optical fibers that were used in the characterization set up were cleaved and etched to be at the same scale as the structure.[37] We also calibrated the losses observed in the measurement if a fiber has to be changed in the middle of the experiment. To measure insertion losses observed we took a 30 cm fiber and cleaved it in two equal length fibers. The two ends of the fibers were

cut smoothly using our in-house fiber cleaving assembly.[37] One end of both the fibers was connected to the two IR detectors as shown in Fig. 41a.

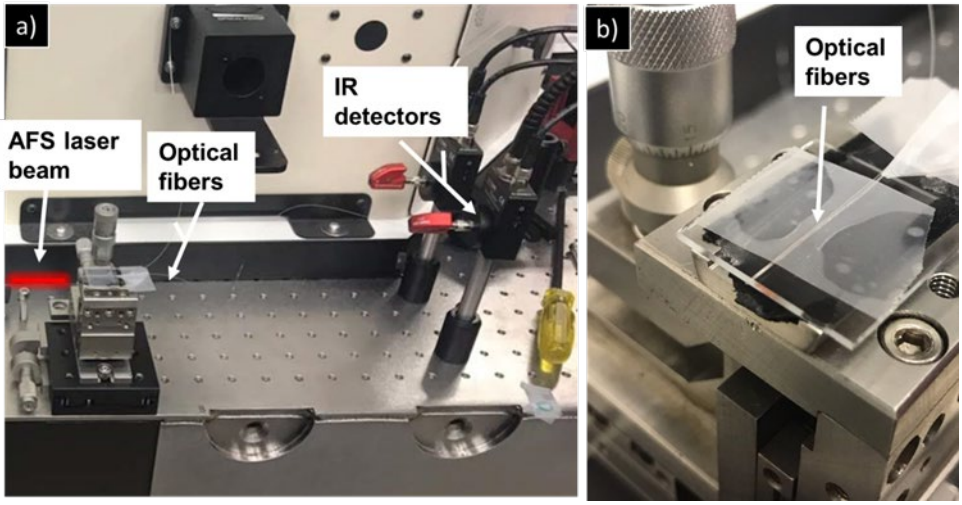

Figure 41. Experimental setup for the measurement of differences observed in the signal when using two optical fibers cleaved using in-house system. (a) The setup showing optical fibers in the path of AFS input laser beam and (b) magnified view of the input end of the two optical fibers side by side taped on a glass slide.

The other end of both the fibers was gently taped on a glass slide with the exposed end extending in the air as shown in Fig. 41b. The glass slide was fixed with a double sided carbon tape on a three-axis positioner. The optical fibers were placed in the path of the AFS laser beam and the three-axis positioner was translated in *xy* and *z*- directions until no change in the signal was observed. The position of the fiber was fixed at this point. The two IR detectors were connected to the oscilloscope and the signal observed by the optical fibers was measured as V in oscilloscope. Figure 42 shows a plot between the oscilloscope signals versus the number of times the measurement was done. The line plots between Det. 1 and Det.2 follow similar pattern and the difference between the two measurements had a maximum error of 8.7%.

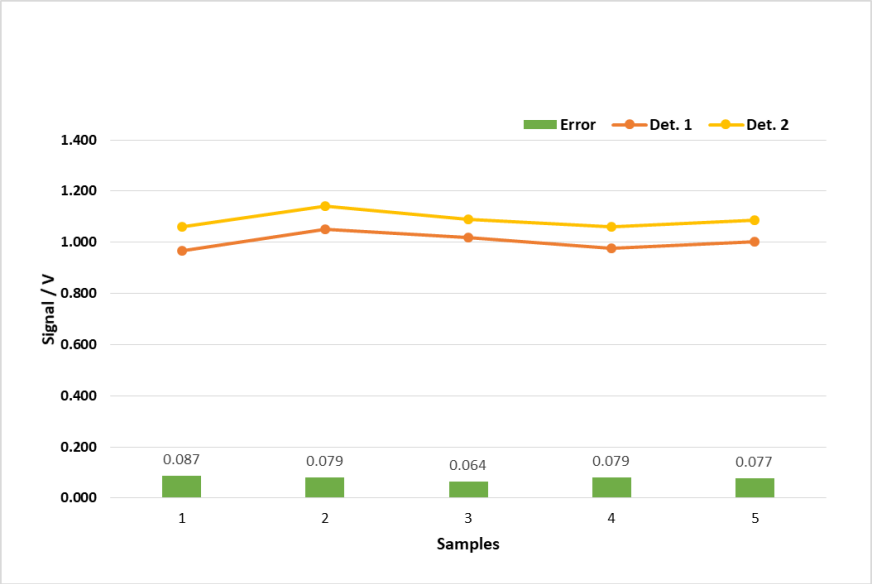

Figure 42. Plot between oscilloscope signal and sample measurements showing the voltage measured by the two fiber-detector combinations. The error between the two measurements is shown in green bar graph which varied between 6% - 9%.

4.6 Structural Characterization

4.6.1 Scanning electron microscopy (SEM) imaging

The waveguides and uniform lattices were structurally characterized using SEM imaging. The imaging was used to identify any structural distortion, the unreacted residue on the structures and shrinkage in the final structures. For SEM imaging the structures were sputter coated with Au/Pd for 6 minutes (Emitech K675X). During first 2 minutes the sample was coated from the top and then it was tilted at an angle and coated for 2 minutes at each angle 50 degrees. SEM imaging was done at different magnification and with different perspectives. These images were used to measure the unit cell dimensions, lattice spacing and fill factor of the uniform lattice.

4.6.2 Calculation of fill factor

The fill factor of the uniform lattice was measured by a MatLab image processing tool. The SEM image was converted into a binary image, which was then used to measure the dimensions of the uniform lattice using a caliper method. These measurements were used to calculate the volumetric fill factor using the formula in equation 20.[37] The position of the terms used in the formula is shown in Fig. 43,

$$FF = \frac{([(L+l)(W+w)-lw]H)+T^2h}{(L+l)(W+w)(H+h)} \tag{20}$$

where L and *l* are the widths and the space in between the *y*- axis lines, W and *w* are the widths and the space in between the lines in *x*- axis, H and *h* are the thickness of the structure in *z*- axis when viewed from the side and T is the thickness of the columns.

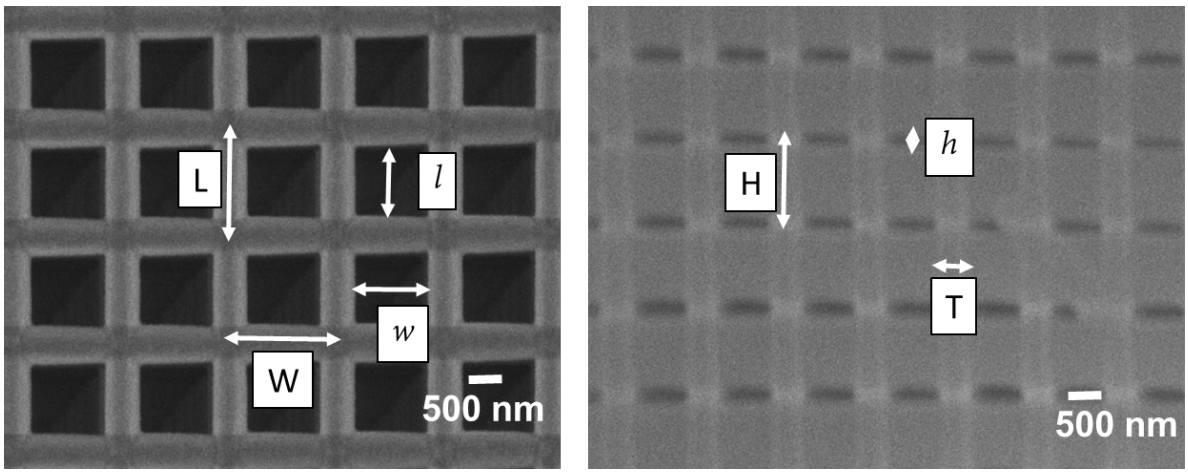

Figure 43. Magnified view of the uniform lattice (left) top view with the positions of lengths and widths marked, (right) side view with the positions of height and thickness marked.

The errors in the measurements were propagated using the standard error propagation equation 21,

$$\delta FF = FF\sqrt{\sum\left(\frac{x}{\delta x}\right)^2} \tag{21}$$

where δFF is the error in the fill factor and x and δx are any measured value and its uncertainty.

4.6.3 Calculation of the transmission efficiency

The transmission efficiency is used as a scale to characterize the optical behavior of light in uniform lattices and waveguides. Transmission efficiency is the ratio of light measured by the output detector, when the structure was placed in between the source and straight fibers to the light measured by the detector when the source and straight fibers were 35 μm apart in air. The transmission efficiency of the waveguides and uniform lattice was calculated using equation 22

$$Transmission\text{-}efficiency = \frac{I_{output}^{Peak}}{I_{air}^{Peak}} \times 100\% \tag{22}$$

where I_{output}^{Peak} is the intensity of the beam measured at the output face of the structures and I_{air}^{Peak} is the peak intensity measured without the structure with the straight through fiber scanned at a distance of 35 μm from the source fiber. The intensity measured is the convolution of the irradiance distribution in space in *y*- and z- axis for a given detector-fiber combination.

5. OPTICAL AND STRUCTURAL CHARACTERIZATION OF WAVEGUIDES AND UNIFORM LATTICES

5.1 Introduction

SVPCs are a powerful addition to the toolbox of devices for integrated optics (IO). Because SVPCs can be structured to control the propagation of light through sharp turns, they can be form the basis for a wide range of useful devices, such as interconnects and out-of-plane beam benders that are essential for densely packed optical circuits. In SVPCs, the propagation of light is controlled by the self-collimation effect. Light moving between unit cells in a lattice is forced to travel in directions that are normal to the IFC. A unit cell can be designed so that the corresponding IFCs are flat, in which case, diffraction is suppressed, and the direction in which light moves through the lattice is determined by the spatial orientation of the unit cells.[23, 73] An SVPC can be designed then as a lattice of self-collimating unit cells that are spatially vary in orientation to force light to propagate without diffraction along an arbitrary curved path. Like SVPC, optical waveguides also carry light from one point to another. However, an optical waveguide works on the principle of total internal reflection (TIR), which makes sharp turns inefficient due to bending losses. To steer light through a turn without significant mode leakage, a waveguide must have a curve radius that is at least one hundred times the vacuum wavelength.[75] To prove this point, curved and straight waveguides were fabricated via MPL in SU-8 and optically characterized for their beam bending efficiency using an Er:YAG laser λ_0 = 2.94 μm. The beam bending efficiency of the curved waveguides was then compared to that of SVPCs.

In contrast to SVPCs, uniform-lattice photonic crystal (ULPCs) are simply periodic dielectric lattices comprised of a single unit cell that repeat throughout the volume of the structure.

Self-collimation of light propagating in ULPCs having high refractive index ($n > 3.4$) has been explored by Federer *et al.*[76] In our work, we fabricated and characterized some optical properties of ULPCs with a lattice spacing of $a = 1.05$ μm created by MPL using IP-Dip photoresist. IP-Dip is a cross-linkable acrylate, with a refractive index before polymerization of 1.52 at $\lambda_0 = 800$ nm[77], therefore the UPLCs reported here have low refractive index relative to previous related work. The ULPCs were fabricated with different fill factors, and polarization dependent self-collimation in the crystals was explored at $\lambda_0 = 1.55$ μm using the output pulses from an AFS laser.

5.2 Design of Structures

5.2.1 Curve and straight waveguides fabricated in SU-8

Digaum *et al*. fabricated the first SVPC as a proof concept and showed that the device could bend light through a 90-degree turn with radius as small as $6.4\lambda_0$.[23] To benchmark the beam bending observed in SVPCs, we fabricated curved and straight waveguides in SU-8. The waveguides were fabricated on top of two 10 μm tall pillars for support. To enable direct comparison to the SVPC, one curved waveguide was fabricated with the same bend radius of R_{bend} = 19 μm. Waveguides were also fabricated with $R_{bend} = 38$ μm and $R_{bend} = \infty$ (unbent waveguide) to investigate the trend in bending efficiency versus R_{bend}, as well as the losses due to input and output coupling alone. The waveguides were designed with a cross-section of 10 μm in width and 10 μm in height, to match the mode profile of the input beam. The straight waveguide was used as a reference so that the bending efficiency of the devices could be normalized against that of the

straight waveguide, and to account for input- and output-coupling losses and scattering losses that should be similar for all devices in the series.

5.2.2 Uniform-lattice photonic crystals fabricated in IP-Dip

The lattice spacing of the SVPCs and ULPCs for λ_0 = 1.55 μm was calculated from the normalized frequency of the flat IFC (a/λ_0 = 0.706) as a = 1.05 μm, because 0.706 is the value of normalized frequency at which the IFC are flat for this unit cell.[73] The IP-Dip has a refractive index of 1.52, which makes it an ideal substitute for index matching oil in fabrication. IP-Dip also provides better resolution because it polymerizes with low shrinkage and low proximity effect due to the absence of solvent in the monomer mixture. These properties made IP-Dip an ideal photoresist for fabricating SVPCs and ULPCs with scaled-down lattice spacing of 1.05 μm. The self-collimation results were compared with the beam bending observed in the SVPCs fabricated in IP-Dip by MPL and characterized at λ_0 = 1.55 μm.[37] SVPCs lattice with 23 μm × 23 μm × 23 μm was generated by Rumpf *et al.*[73] Digaum and coworkers fabricated and characterized the SVPC.[37] The connecting lines of the ULPCs were fabricated with the same rectangular shape and aspect ratio as that of the SVPCs, so both structures had the same unit cell. The ULPCs were fabricated with a range of fill factors and characterized for polarization dependent self-collimation at λ_0 = 1.55 μm.

5.3 Structural Characterization

5.3.1 Curved and straight waveguides

The waveguides in Fig. 44 were optically characterized using the output of a pulsed Er:YAG laser having λ_0 = 2.94 μm. The sample was sputter-coated with Au/Pd and optically characterized by SEM. The waveguides were fabricated on top of a 100 μm tall pillar with two 10 μm pillars supporting the ends of the waveguides. The image shows a pair of stable self-supporting robust curved and straight waveguides. Figure 44 is a compilation of the SEM images of the waveguides. These images were used to assess the smoothness and robustness of the entry and exit face of the beam. In order to acquire SEM images, the structures must be sputter-coated first with Au/Pd. However, sputter-coating makes the waveguides unsuitable for optical characterization. Therefore, the structures were first optically characterized using the Er:YAG laser and then imaged via SEM.

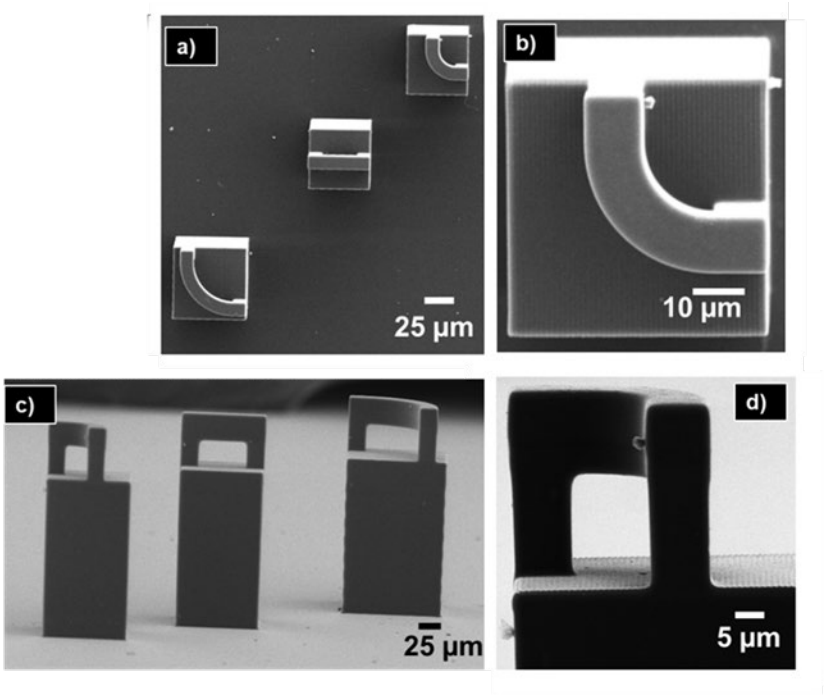

Figure 44. SEM images of the curved and straight waveguides fabricated in SU-8. (a & c) Top- and side-view of the waveguides showing two curved (R_{bend} = 19 µm and 38 µm) and a straight (length = 50 µm, $R_{bend} = \infty$) waveguides. (b & d) Magnified top- and side-views of the curved waveguide having R_{bend} = 19 µm. The waveguides were fabricated on a 100 µm tall pillar for free movement of the optical fibers.

5.3.2 Uniform-lattice photonic crystal (ULPC)

The ULPCs were fabricated to function at λ_0 = 1.55 µm, with the same *final* lattice spacing (a = 1.05 µm) as the SVPCs created in IP-Dip photoresist by Digaum *et al*.[37] In his work, Digaum observed a volumetric shrinkage of 30% and linear shrinkage of 10% - 15%. Therefore, to account for shrinkage while fabricating ULPCs, the *targeted* structures were fabricated with a lattice spacing at a = 1.10 µm. After exposure and developing, the *final* structures were found to have shrunk by 12% - 15%, with volumetric shrinkage of 31%, giving a final lattice spacing of a = 1.05 ± 0.023. The devices were also fabricated on the top a small pillar allows them to shrink isotropically during post-exposure processing.

The SEM images of the ULPCs are shown in Fig. 45. The image shows a well formed, stable, and a self-supporting ULPC. The dimensions of rods comprising the lattice range from 220 nm to 650 nm in width and 350 nm to 780 nm in thickness. In addition, the SEM images were also used to measure the fill factor and the aspect ratio of the ULPCs.

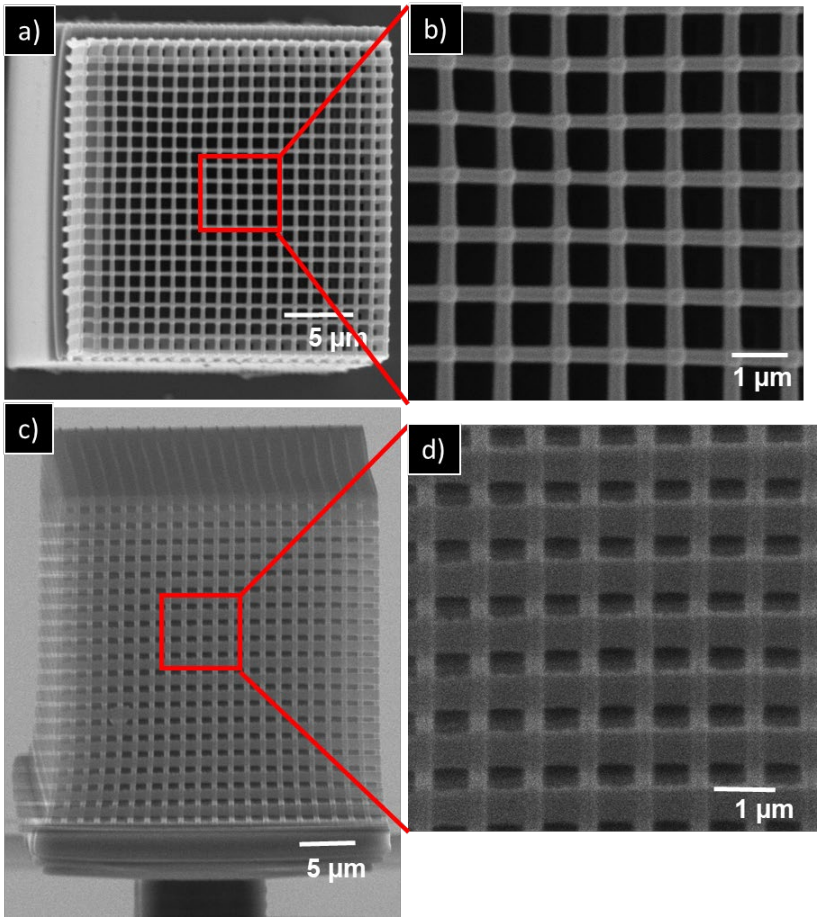

Figure 45. SEM images of the ULPC fabricated in IP-Dip at an average laser power of 2 mW and a lattice spacing of a = 1.05 µm. (a & c) Top- and side-views of the overall lattice. (b & d) Magnified view of the top and sides of the UPLC, marked in red squares.

5.4 Optical characterization of waveguides using an Er:YAG laser at 2.94 μm

The optical performance of the waveguides was used as a standard to benchmark the beam bending efficiency of the SVPCs fabricated with the same material (SU-8) with R_{bend} = 19 μm. The profile of light exiting the source fiber was characterized by butt-coupling it with the straight-through fiber and measuring the relative power exchanged between them as the straight-through fiber was scanned transverse to the source fiber. To characterize the divergence of light exiting the source fiber, the source- and straight-through fibers were separated axially by fixed distances and the transverse beam-scans were repeated. The 50 μm straight waveguide was then positioned in between the two fibers and the straight-through fiber was scanned to obtain a measurement of the transverse irradiance distribution of light exiting the waveguide. The straight waveguides were then replaced with curved waveguides and another detector-coupled fiber was used to measure the output of "bent beams" exiting these devices.

Figure 46 shows the comparison between the light guiding efficiency of the straight and curved waveguides. The low efficiency of the straight waveguide compared to propagation in free space is attributed to the fact that SU-8 2075 is highly absorbing at λ_0 = 2.94 μm, so it transmits only 25% of the incident light. The efficiency is also decreased by losses from insertion and output coupling at the device faces.[37] The bending efficiency of the curved waveguide increases by a factor of 1.5 as R_{bend} doubles from 19 μm to 38 μm. The increase in peak intensity with the increase in bend radius confirms that the waveguides are functioning via total internal reflection (TIR). The beam bending efficiency of the waveguide with R_{bend} = 19 μm was also compared to that of the spatially variant photonic crystal (SVPC) having the same R_{bend}. The SVPC was found to bend light through the turn with an efficiency that was 90% greater than the waveguide.[23]

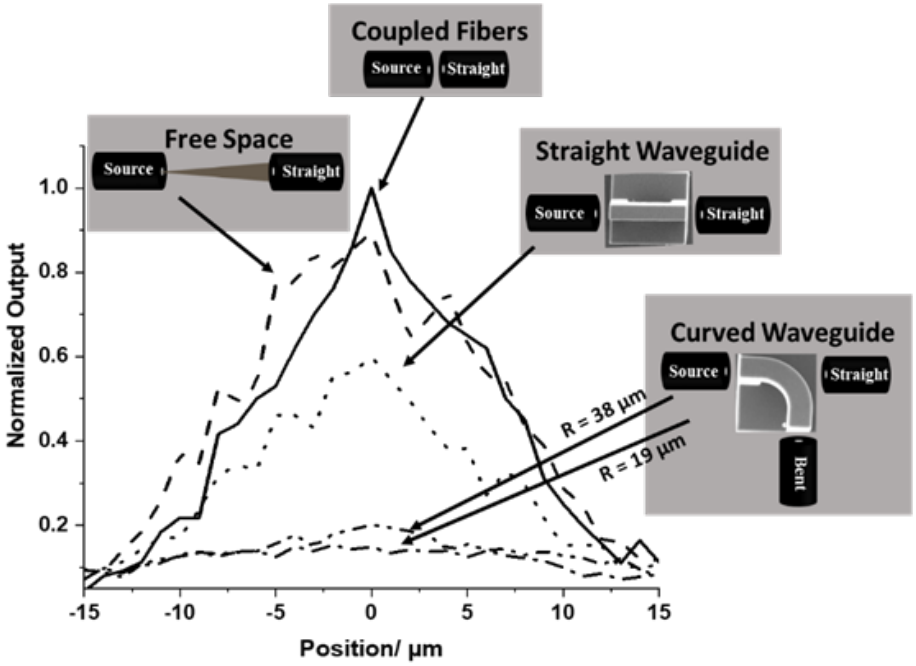

Figure 46. Line-scans of the normalized signal recorded versus position of a detector-coupled optical fiber translated laterally at either the output-end of a source-fiber or the waveguides coupled to the source-fiber. Measurements at the source-fiber reveal the spatial distribution of light coupled into the waveguides and how the emerging mode freely diverges in air. Measurements at the output-end of the waveguides reveal how efficiently light couples into the devices and is guided through tight turns as a function of turn-radius, R_{bend}.

5.5 Optical characterization of uniform-lattice photonic crystals at 1.55 µm

5.5.1 Self-collimation in the ULPCs

The optical behavior of the ULPCs was explored with respect to the bandwidth and polarization of the source beam. The original beam coming from the AFS laser was vertically polarized. The zero-order beam of high bandwidth (150 nm) and the first order beam of low bandwidth (10 nm) from the AFS laser were routed to the sample through a source fiber. The

polarization of the beam was adjusted by the half waveplate/polarizer combination before the beam entered the coupling objective.

The width of the source beam was measured by coupling the source and the straight fiber and scanning the straight fiber across the full width of the lattice, from +15 μm to -15 μm in both the *y*- and *z*- axes. The divergence of the beam in free space was also measured by moving the straight fiber 35 μm from the source fiber along the *x*-axis, re-measuring the intensity profile in the *yz*-plane, and comparing the intensity profiles measured at the two positions along the *x*-axis.

The divergence of the beam emanating from the fiber can be estimated by approximating it as a Gaussian beam, with an initial beam diameter ($1/e^2$) set as the mode-field diameter (MFD) of the fiber.[78] The MFD (9.5 ± 0.5 μm) of the optical fiber was used to get initial beam radius (w_0) as 4.25 μm The beam radius of the diverging beam along the propagation axis at a distance z was measured as $w(z)$, and $z_R(w_0)$ is the Rayleigh range of the beam calculated using Equations 23 and 24.

$$w(z) = w_0 \sqrt{1 + \left[\frac{z}{z_{R\,(w_0)}}\right]^2}, \tag{23}$$

$$z_R(w_0) = \frac{\pi}{\lambda_0} w_0^2 \tag{24}$$

$$I = I_0 e^{-2r^2/w^2} \tag{25}$$

$$w = 0.8493218 * FWHM \tag{26}$$

In a normalized Gaussian beam, the FWHM is the point where the intensity of the beam reaches half of its peak intensity. Therefore, a relationship between beam radius and FWHM was

derived from Equation 25 by substituting $I = I_0/2$, as shown in Equation 26. The theoretical FWHM was calculated by using Equation 26.

Figure 47 shows the line scans of the beam exiting the source fiber as a function of the straight fiber position. The position dependent FWHM of the diverging beam (Fig. 46) was de-convoluted by dividing the measured FWHM with square root of 2. The de-convoluted FWHM was then compared with the theoretically calculated FWHM, which was calculated by using Equation 26. Figure 48 shows the comparison between the experimental and the theoretical beam divergence. The theoretical and the experimental values are in agreement with each other, especially at 35 µm, which is the point of measurement for all the future experiments.

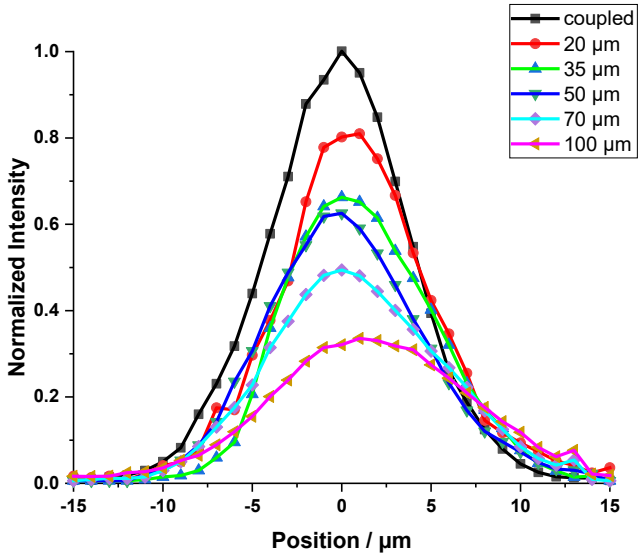

Figure 47. Line scans showing the divergence of the beam exiting the source fiber as a function of distance from the end of the fiber.

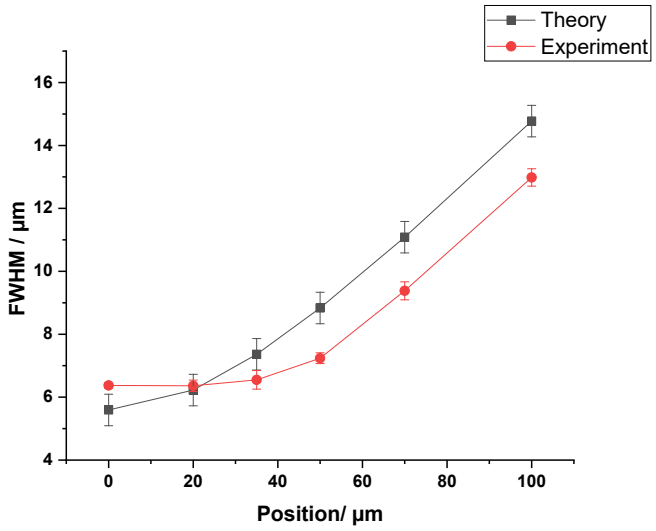

Figure 48. The experimental and the theoretical beam divergence results compared with each other. The MFD of the fiber is considered as the initial FWHM of the theoretical measurements. The experimental divergence was measured by moving the straight fiber from 0 µm – 100 µm along *x*-axis.

To assess the degree of self-collimation as a function of polarization, measurements were performed separately using both vertically and horizontally polarized source beams. The FWHM of the output beam was measured by scanning the straight-fiber from +15 µm to -15 µm in both *y*- and *z*-axes on the output face of the lattice. Figure 49 and Table 6 shows the line scans of the normalized intensity plots of the bandwidth-dependent self-collimation in a ULPC with a 53% fill factor and FWHM of the respective line-scans. For both the high- and low-bandwidth beams, the lattice was self-collimating for vertically polarized light. The high-bandwidth, horizontally-polarized beam diverged slightly, but the low-bandwidth horizontally-polarized beam diverged significantly.

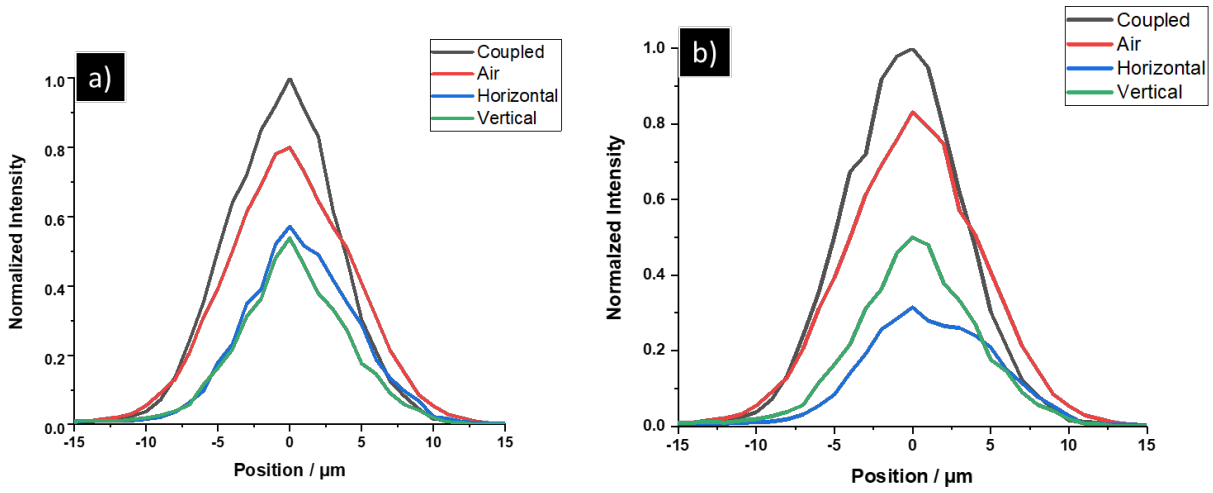

Figure 49. The normalized intensity plots of the line scans on the output face of a ULPC with a volumetric fill factor of 53%. (a) High-bandwidth source beam with self-collimating vertically polarized beam and slightly diverged horizontal polarized beam. (b) Low-bandwidth source beam with self-collimating vertically polarized beam and highly diverged horizontal polarized beam.

Table 6. The FWHM of line-scans recorded for vertically and horizontally polarized beams, from both a low and high bandwidth source, after propagating through a 53%-fill-factor UPLC, or after propagating in air over a distance or either 0 µm or 35 µm.

	High Bandwidth (a)		**Low Bandwidth (b)**	
	Vertical (µm)	**Horizontal (µm)**	**Vertical (µm)**	**Horizontal (µm)**
Coupled fibers	8.45 ± 0.15	8.64 ± 0.22	8.22 ± 0.11	8.36 ± 0.15
Fibers separated by 35 µm	8.73 ± 0.15	8.95 ± 0.12	9.0 ± 0.25	8.92 ± 0.14
53% Fill factor lattice	8.25 ± 0.14	8.75 ± 0.28	8.21± 0.15	9.26 ± 0.14

ULPCs with a range of fill factors were further explored to investigate the characteristic disparity in the behavior of the low bandwidth vertical and the horizontal polarized source beam. The ULPCs with fill factor ranging from 41% to 53% were characterized with the low bandwidth beam to test self-collimation. A plot of the FWHM of the line-scans versus fill-factor of the ULPC is shown in Figure 51. An example of the experimental setup with the source and the straight fiber on the input and output faces of the crystal, and the relative intensity of the line scans of the diverging horizontally polarized and the self-collimating vertically polarized beams is shown in Fig. 50. The FWHM of the horizontally polarized beam was consistently higher than the FWHM of the vertically polarized beam. This finding is consistent with the results seen in Fig. 49.

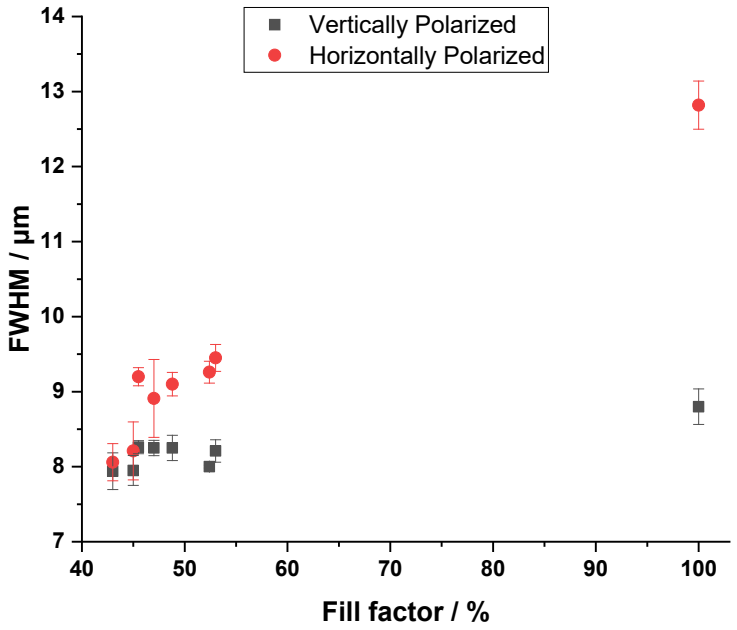

Figure 50. The FWHM of line-scans obtained for beams after travelling through a ULPC having the specified fill-factor. The beams had low-bandwidth and were either vertical- or horizontally polarized. The vertically polarized beam was self-collimated with FWHM within 8.0 ± 0.5 µm in the whole range of ULPCs. Horizontally polarized beam diverged within lattices of all fill factors.

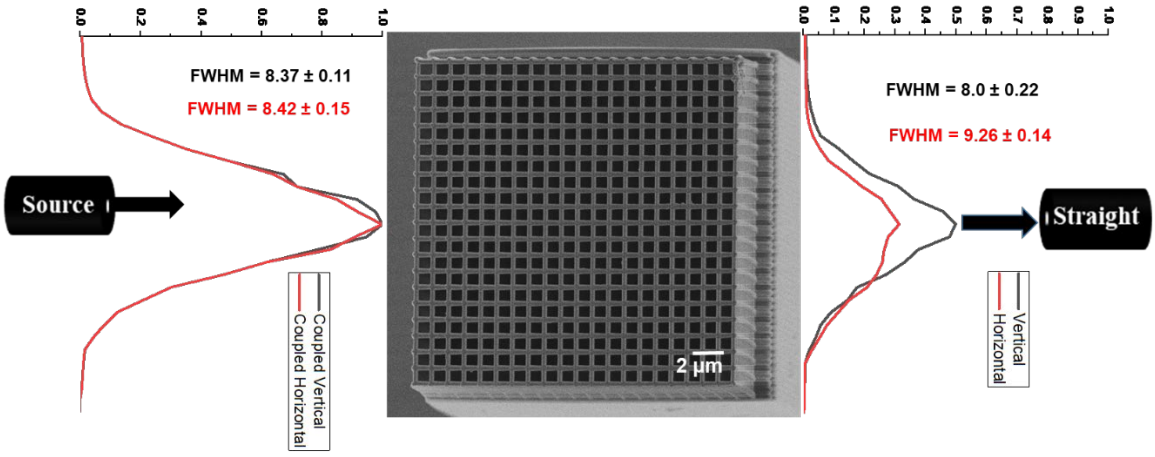

Figure 51. The relative intensity of light at λ_0 = 1.55 µm at the input and output faces of an ULPC (*top-view SEM image*) having a fill factor 45%. The low bandwidth vertically polarized beam was self-collimated through the lattice. However, the horizontally polarized beam was diverged through the lattice.

The SVPCs fabricated with the same material and lattice spacing also had polarization selective beam bending. The vertically polarized beam was steered through a 90 degree turn, but the horizontally polarized beam passes straight through the lattice. Figure 52 shows the polarization selective simulations by Rumpf *et al.*[73] and experimental results by Digaum *et al.*[23] The polarization selective self-collimation observed in ULPCs is a step forward towards understanding the phenomenon of light travel in a periodic lattice.

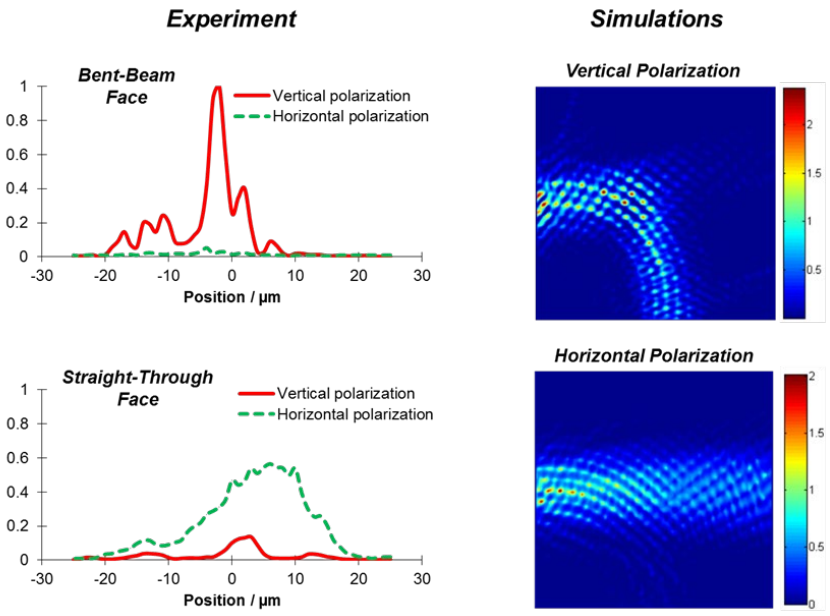

Figure 52. An SVPC with a fill-factor of 53% showing high polarization selectivity. (*Left*) Experimental line-scans of the relative intensity for both vertically and horizontally polarized light that is bent through the turn or passes straight through the SVPC. (*Right*) Simulation results of the same SVPC with both horizontally and vertically polarized light. Image taken from Digaum *et al.*[79]

5.5.2 Transmission efficiency of the ULPCs

To understand the underlying physics behind creating efficient beam bending devices, ULPCs with different fill factors and lattice spacing were fabricated. The fill factor dependent transmission efficiency of the ULPCs was explored by using the formula described in Section 4.6.3.

Figure 53 shows a plot of the transmission efficiency versus fill factor with respect to the low band width vertically and horizontally polarized beams. In the plot, the highest efficiency for the vertically polarized beam is 80% at a fill factor of 48%.

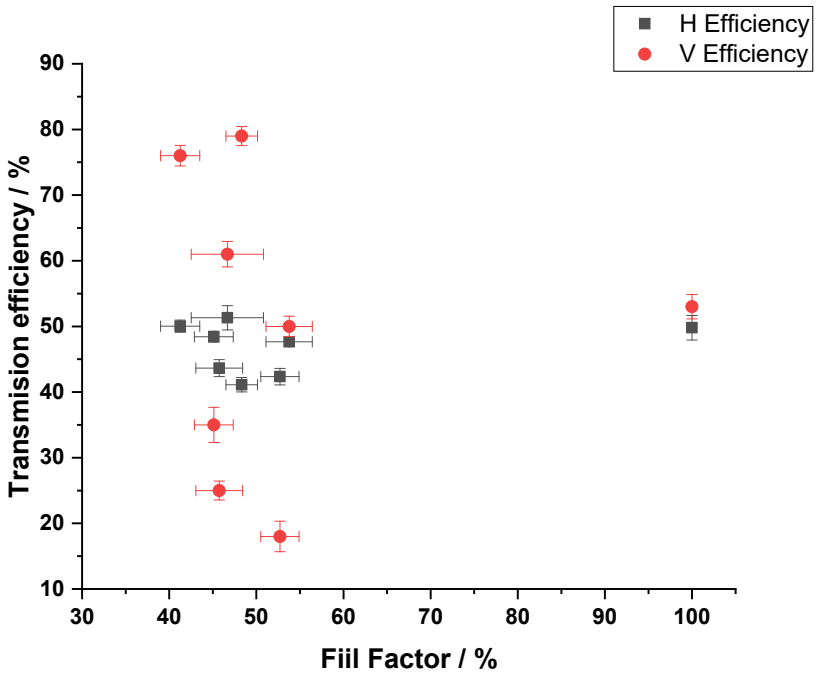

Figure 53. The ULPC transmission efficiency with the low bandwidth horizontally and vertically polarized beams with respect to the fill factor. The ULPC with 48% fill factor had maximum transmission efficiency of 80% with the vertically polarized beam. The transmission efficiency was insensitive to the horizontally polarized beam.

The plot also shows that the transmission efficiency changes very rapidly with the change in fill factor. For the ULPC with fill factor 53% the transmission efficiency was ~ 15%. However, in the case of horizontally polarized beam the fill factor did not have any effect on the transmission efficiency. The efficiency remained in the range of 45% - 55% for the entire fill factor range. The ULPC with 100% fill factor was also fabricated as a monolithic block (100% fill-factor in Fig. 53), and the transmission efficiency through this structure did not depend on the polarization of the input beams, as expected.

5.6 Conclusion

The 3D SVPCs were shown to be capable of bending light through a 90 degree turn.[23] In this section, we have fabricated curved waveguides in SU-8 2075 with a similar bending radius as the SVPCs and quantified the beam bending efficiency. The beam bending in the waveguides suffered losses due to mode leakage along the sharp turns. Therefore, the beam bending observed in the waveguide was almost 90% smaller than the SVPC with comparable radius. These results provide further evidence that the SVPCs do not operate through total internal reflection, but rather through self-collimation, as designed.

The 3D ULPCs were fabricated in IP-Dip with the lattice spacing similar to the SVPCs fabricated in the same material. The phenomenon of light travel in the ULPCs was explored to further understand the physics behind beam bending in the SVPCs. The ULPCs were exposed to the low and high bandwidth beams with vertical and horizontal polarization. The ULPCs were self-collimating for only the vertically polarized beam, whereas horizontally polarized beams diverged as they travel through the device. The fill factor dependent transmission efficiency of the ULPCs were also measured with respect to vertical and horizontal polarized beams. The ULPC with 48% fill factor had the highest transmission efficiency of 80%. The transmission efficiency of the vertically polarized beam was highly sensitive to the fill factor. However, the transmission efficiency of the horizontally polarized beam was insensitive to the fill factor. These results show that a periodic lattice with lattice spacing of 1.05 μm is capable of self-collimating light with 80% transmission efficiency. An upper limit of the transmission efficiency by a periodic lattice has been realized, and the beam bending efficiency in the SVPC can be improved by optimizing the SVPC design and fabrication process.

6. ETCHING OF GOLD/PALLADIUM COATING

6.1 Introduction

6.1.1 Scanning electron microscopy

Scanning electron microscopy (SEM) is an increasingly diverse technique, which is used to acquire 2D and 3D data of biological,[80] archeological,[81] forensic[82] and material science specimens.[83] SEM was first developed in the 1930s and in the1940s by Knoll in Germany and later by Zworykin in America. In 1948 Oatley and his students developed the first commercial SEM,[84] and now it is used as a crucial tool in imaging across many cutting-edge applications including measurements of topography, composition, and morphology of specimens.

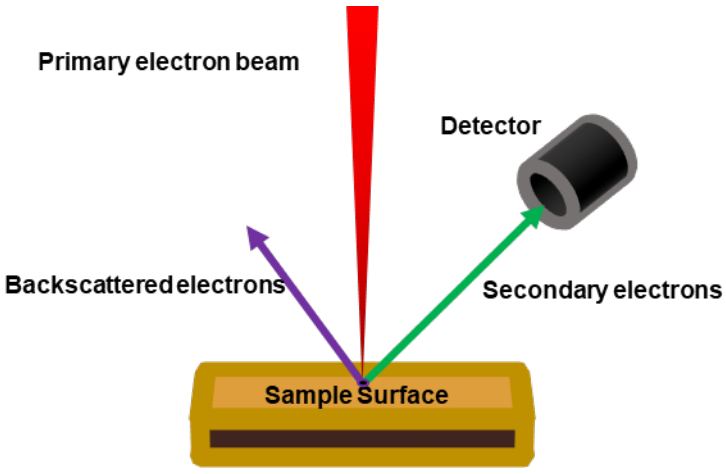

Figure 54. Schematic illustration of different types of electrons emitted from the sample surface when a high energy electron strikes the sample surface.

In SEM (Fig. 54) a highly focused electron beam is generated by using an electron gun as a source. The electrons are accelerated through a column and focused onto the sample via an objective lens. The size of the beam is controlled by many apertures present in the SEM assembly. When the accelerated electrons strike the sample, they interact with the atoms of the specimen at various depths. Different types of ejected electrons − including secondary electrons (SE), back-scattered electrons (BSE), and transmitted electrons − relay different information about the specimen. SEM is mostly used to measure SE (< 50 eV) which are ejected from the surface of the specimen thus provide a very high-resolution image of the sample.

6.1.2 Sputter coating

SEM is best suited for samples with a conducting surface. However, nonconductive specimens like organic polymers and biological specimens can be imaged when coated with a thin metal layer. The metal layer prevents accumulation of charge on the surface and provides high-resolution images. The process of coating with a thin metal layer under low vacuum is known as sputter coating. Sputter coating can be done with gold (Au), gold/palladium (Au/Pd), platinum (Pt) or chromium (Cr) metals. Coating with Au and Au/Pd is most common for SEM imaging. Sputter coating has many advantages as it prevents charging and makes it possible to image non-conductive specimens. However, its biggest drawback is that sputter coating radically alters the sample surface by changing the sample surface color and making the surface opaque, making the sample unusable for further optical characterization.

In MPL 3D free-standing structures are fabricated using non-conducting photoresists like SU-8 and IP-Dip. For optical characterization of these structures, the samples are coated with a

thin layer of Au/Pd and imaged via SEM. Coating the sample makes them unusable for optical characterization via AFS laser because sputter coating radically alters the properties of the structures.

There are some methods available in the literature to remove metal coatings from the samples.[85-87] However, these techniques require excessive handling of the specimen, which may damage essential and fragile samples. Miller *et al.* in 2004 developed a non-toxic method for Au/Pd removal using the output from a Nd:YAG (Neodymium: Yttrium aluminum garnet) laser.[88] This method does not involve too much sample handling, thus, it reduces the chances of sample damage. However, this method is expensive and time consuming to use. Leslie *et al.* in 2007 developed a non-destructive method to dissolve Au coating using potassium cyanide (KCN) solution.[89] This method is cheap, fast, and as non-damaging to the sample, but there are potential safety concerns about using highly poisonous KCN solution. Jones *et al.* in 2012 developed a non-destructive and safe method for etching of Au from archeological specimens using ionic liquids as solvent and iodine as an oxidizing agent.[90]

In this chapter, we have applied the method proposed by Jones *et al.* to etch Au/Pd coating from the 3D samples fabricated via MPL. This is the first time this method has been used to etch Au/Pd coating from organic photoresists. Modifications were made in the development process to prevent any damage to the samples. The structural and optical integrity of the etched sample was investigated by SEM imaging and optically characterizing the etched sample by AFS laser at λ_0 = 1.55 μm.

6.2 Theory

An ionic liquid is a solution which melts below 100 °C and consists of only ions in the solution. Ionic liquids have found applications in many reaction processes as solvents, reagents, catalysts or a combination of all of these.[91] Ethaline is a deep eutectic solution made by mixing choline chloride and ethylene glycol. Ethaline has a very high chloride ion concentration and good solubility for iodine (5 mM).[92] Late transition metal ions like Pd, Au, and Pt form stable chloro-complexes with chloride ions in the absence of any other ions in the solution. Since stable metal ions are present in the solution as metal-chloro complexes, even a weak oxidizing agent like iodine is capable of oxidizing the inert metals. A saturated solution of potassium iodide (KI) was used to dissolve all the unreacted iodine from the reaction mixture.

6.3 Experimental

6.3.1 Materials required

3D structures were fabricated by MPL and sputter coated (Emitech K675X) with a 20 nm Au/Pd thick layer. The ethaline solution was prepared by mixing choline chloride (Sigma-Aldrich ≥ 98%, CAS 67-48-1) and ethylene glycol (Sigma-Aldrich ≥ 98%, CAS 107-21-1). Iodine flakes (Fisher scientific ≥ 99.5%, CAS 7553-56-2) were used as an oxidizing agent, and potassium iodide (KI, Acros Organics, CAS 7681-11-0) solution was used to remove unreacted iodine from the reaction. Lastly, DI water was used to rinsing.

6.3.2 Method

The ethaline solution was prepared by mixing choline chloride and ethylene glycol in a 1:2 molar ratio. The mixture was heated to 60 °C to ensure complete solubility of choline chloride, which takes about 5 min - 10 min. This solution can be prepared in advance and kept under cool and dry conditions in a closed glass jar for future use. With time choline chloride may crystallize and settle at the bottom of the flask, so it is recommended to mix the solution well at 60 °C to dissolve any crystalized choline chloride prior to its use. Iodine flakes were dissolved in this solution at a concentration of 0.125 M at 60 °C. Although this iodine solution is stable for some time, it is recommended to make it fresh for best results. The metal coated microstructure was placed in 10 mL glass beaker, and iodine solution (2 mL) was carefully added in the beaker using the pasteur pipette without disturbing the sample. The sample was left submerged in this solution for 15 minutes at 60 °C. After 15 minutes instead of removing the sample from the solution, it is recommended to first remove the solvent from the beaker by using a pipette. The sample was then picked up from the beaker with a pair of tweezers and placed in the development assembly shown in Fig. 31. The development assembly was filled with a saturated solution of aqueous KI. The sample was left in the KI solution for 15 minutes. KI solution was used to increase the solubility of iodine in water by forming I_3^- ions. This process was repeated twice to dissolve all the unreacted iodine. Repeated washing prevents settling of any iodine crystals on the sample. In the end, the sample was submerged in DI water for 10 minutes followed by air drying.

6.4 Results and Discussion

6.4.1 Structural characterization

The difference between the sputter coated sample and the etched sample can be seen by the naked eye. The sputter coated sample was reflective and opaque due to a black metal coating as shown in Fig. 55a, in which the reflection of the camera lens taking the image can be seen. After etching, the sample was not only transparent but also colorless as seen in Fig. 55b.

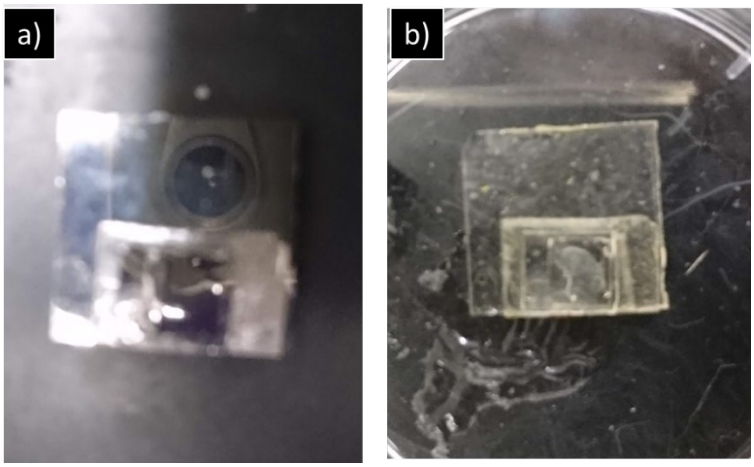

Figure 55. 3D sample fabricated by MPL (a) Au/Pd sputter coated sample which is reflective and black in color, the reflection of the camera can be noticed in the image. (b) Etched sample non-reflective and transparent.

A uniform lattice was fabricated by MPL and structurally characterized after Au/Pd sputter coating by SEM. The metal coating on the sample was etched by using ethaline-iodine solution. The etched sample was sputter coated again and reimaged via SEM. The SEM images of the top and side view of the uniform lattice before and after etching are shown in Fig. 56 and Fig. 57, respectively. The magnified view of the images shows that the structural integrity was maintained after etching. The lines were rigid and still connected to the sample. No iodine crystals were left

deposited on the structures. The defects (circled in red) are also visible in both the samples before and after etching as shown in Fig. 57(c & d). These images of the unetched and etched sample confirm that etching has negligible impact on the structural integrity of the sample.

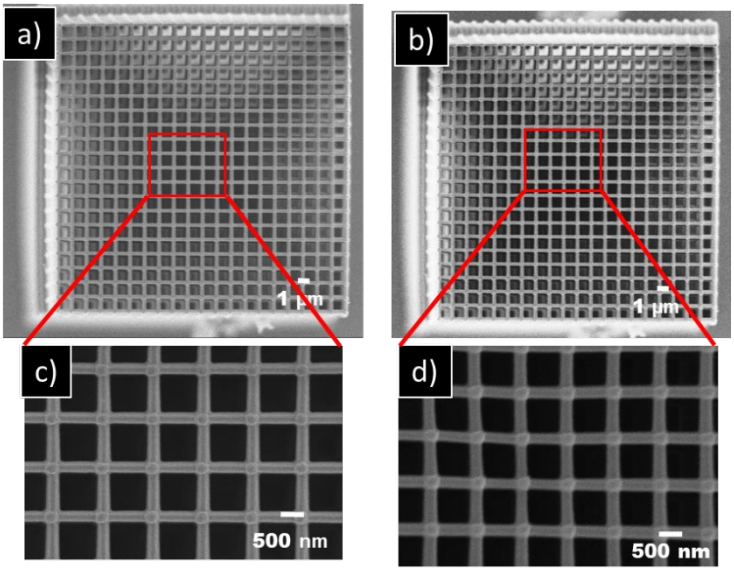

Figure 56. Top-down SEM images of (a & c) the unetched uniform lattice and (b & d) the same uniform lattice after etching.

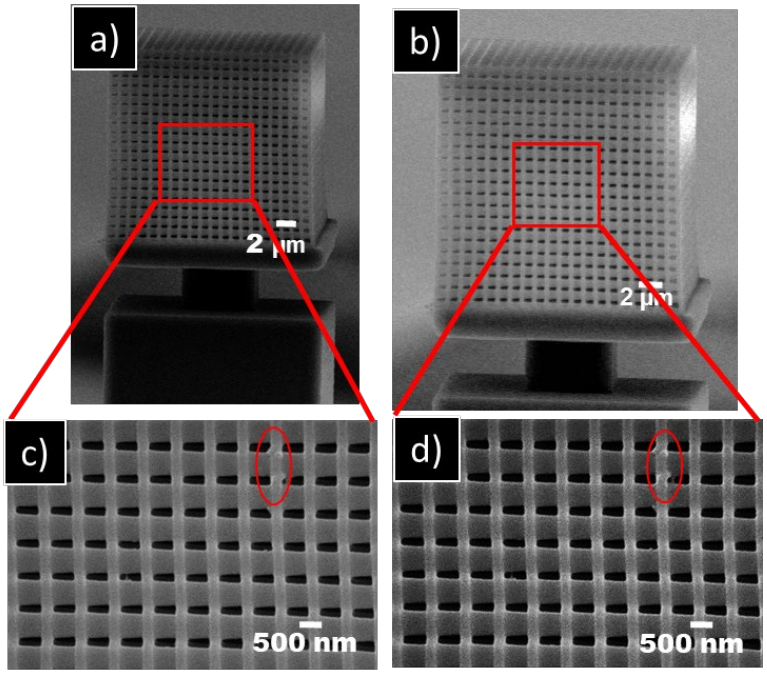

Figure 57. Side-view SEM images of (a & c) the unetched uniform lattice and (b & d) the same uniform lattice after etching.

6.4.2 Laser exposure of the sputter coated sample

Sputter coating is considered a destructive technique. Nonetheless, Digaum and co-workers[93] fabricated an SVPC in SU-8, sputter-coated it with Au/Pd, and then attempted to optically characterize the metal-coated structure at λ_0 = 2.94 µm. The sample was placed in the characterization setup and the beam was shined on the input face of SVPC with a source fiber. The laser exposure damaged the structure due to strong absorption by the metal layer.[37] Optical and SEM images of the damaged SVPC are shown in Fig. 58.

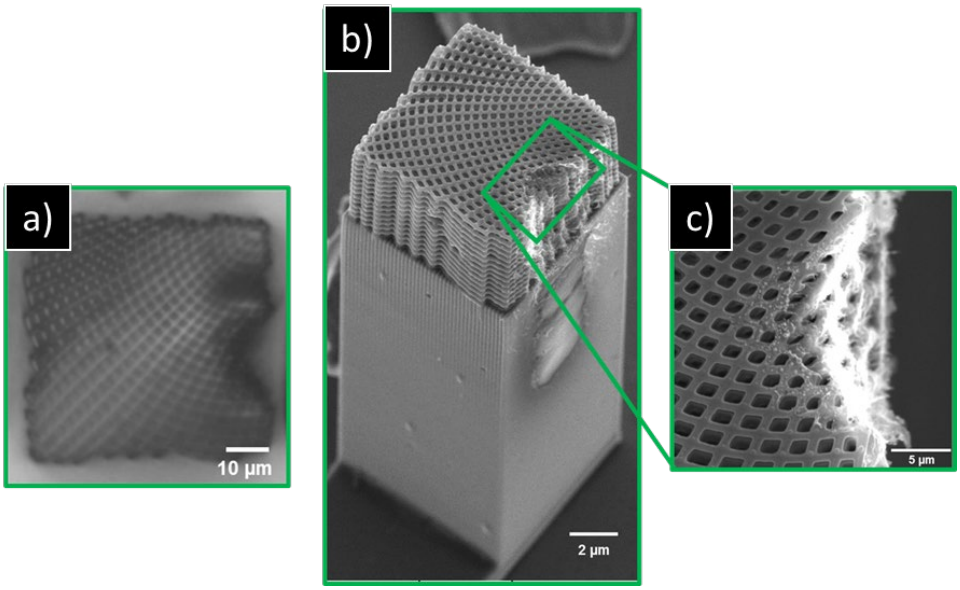

Figure 58. SVPC coated with Au/Pd thin film burned after being exposed to Er:YAG laser emitting λ_0 = 2.94 µm using the same conditions as those used to optically characterize the beam-bending performance of all-dielectric SVPCs. (a) Transmission optical microscope image taken using a Nikon 60x objective and (b & c) SEM perspective and magnified images of a burned SVPC.

We hypothesized that presence of trace metal on the sample surface after etching will burn the sample when exposed to the laser beam. But first, we have to show that a metal coated structure fabricated in IP-Dip will also sustain damage when exposed to λ_0 = 1.55 µm. A 25 µm x 25 µm x 150 µm monolithic block was fabricated in IP-Dip for this experiment. The metal coated sample was placed in front of the source fiber and exposed to the vertically polarized laser beam (λ_0 = 1.55 µm). The laser exposure conditions were kept similar to those described above for optical characterization of lattices. The SEM images of the monolithic block before and after the laser exposure are shown in Fig. 59. No damage to the metal coated block was observed due to laser exposure. Several other samples with a thick coating of metal (~80 nm) were also exposed with a range of laser power (3 mW - 15 mW), but no damage was observed. These observations can be explained by the fact that Au/Pd nanoparticles comprising the sputter-coated surface are non-absorptive at 1.55 µm. Instead of absorption, the laser beam must be reflecting from the sample

surface.[94-95] The results described in this section indicate that the structural integrity of the Au/Pd coated sample was preserved after laser exposure at λ_0 = 1.55 µm. Moreover, this method cannot be used to prove the absence or presence of trace metal on the etched structure.

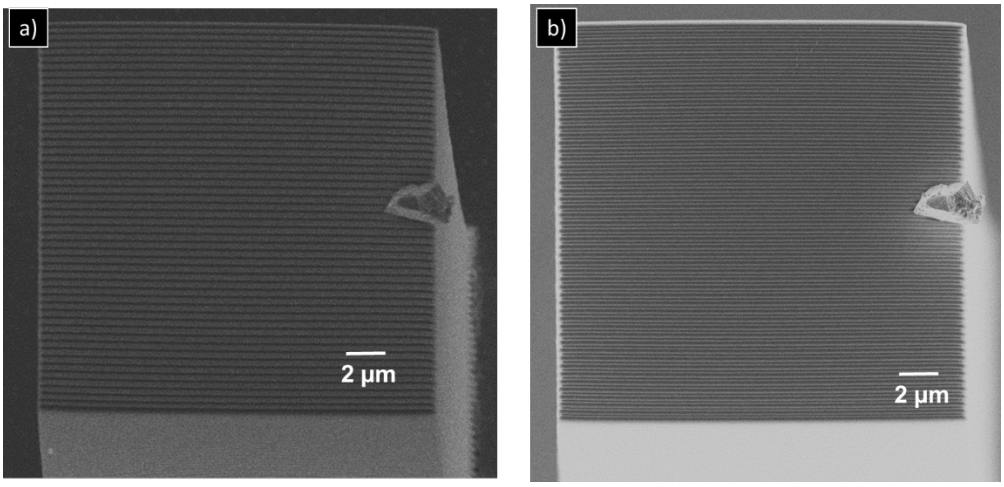

Figure 59. Monolithic block fabricated in IP-Dip and exposed to AFS laser emitting λ_0 = 1.55 µm. a) SEM image of the unetched structure b) SEM image of the laser exposed structure.

6.4.3 Optical characterization of an etched uniform-lattice photonic crystal

A comparison between the optical behavior of the unetched and the etched sample was used to confirm if etching had any effect on the optical properties of the structures. The uniform lattice in Fig. 56 was optically characterized using the AFS laser beam at λ_0 = 1.55 µm with the characterization setup shown in Fig. 33. The laser beam was shined on the face of the lattice using a source optical fiber, whose input end was etched to match the size of the lattice. The optical characterization was performed with both horizontally and vertically polarized beam. Light

emanating from the output face was collected by straight optical fiber and transferred to a PbSe detector. The procedure for optical characterization is explained in detail in Section 4.5.3.

The source and the straight fibers were butt coupled with each other, and the straight fiber was scanned in *y*- and *z*- axes from +15 µm to -15 µm. The straight fiber was moved to 35 µm in *x*- axis in air and the fiber was scanned again in *y*- and *z*-axis from +15 µm to -15 µm. At the end, the sample was placed in between the source and straight fiber and the straight fiber was scanned in *y*- and *z*- axes from +15 µm to -15 µm. Each scan was performed three times. The FWHM of the output beam and transmission efficiency of the sample were calculated with a vertically polarized input beam. The FWHM was calculated by, (i) normalizing the signal from +15 µm to -15 µm in the *y*- and *z*- axes with the reference signal for shot to shot fluctuations, (ii) averaging the individual scans in *y*- and *z*- axes to obtain an average signal along both the axes, (iii) averaging the *y*- and *z*- axes signals, to obtain an average signal at the specific fiber position. Table 7 shows the FWHM and the transmission efficiency of the unetched and etched sample for vertically polarized beam. The FWHM of the vertically polarized beam originating from the etched structure was self-collimating and within one standard deviation of the FWHM of the unetched structure. These results confirm that metal etching did not affect the optical behavior of the sample.

Table 7. The FWHM and the transmission efficiency of the uniform lattice shown in Figure 56 measured by the straight fiber at the output face of the uniform lattice using AFS vertically polarized $\lambda_0 = 1.55$ μm beam.

	FWHM / μm	**Transmission efficiency/ %**
Original Sample	**8.0 ± 0.02**	**76.0 ± 1.89**
Etched Sample	**8.21 ± 0.15**	**74.3 ± 1.45**

6.4.4 Optical properties of a meal coated monolithic block

In an attempt to show that etched structure is free from all trace metal, we decided to explore the effect of the metal coating on the optical behavior of the structure. We hypothesized that in the presence of Au/Pd coating the input face of the structure will be highly reflective which will result in low transmission efficiency. We fabricated a 25 μm × 25 μm × 150 μm monolithic block in IP-Dip photoresist and optically characterized the sputter coated sample at $\lambda_0 = 1.55$ μm and compared the transmission efficiency of the unetched sample and the metal coated sample. Figure 60 shows the SEM images of the unetched monolithic block and the metal coated monolithic block. The SEM images confirm that the structural integrity of the sample was maintained after laser exposure.

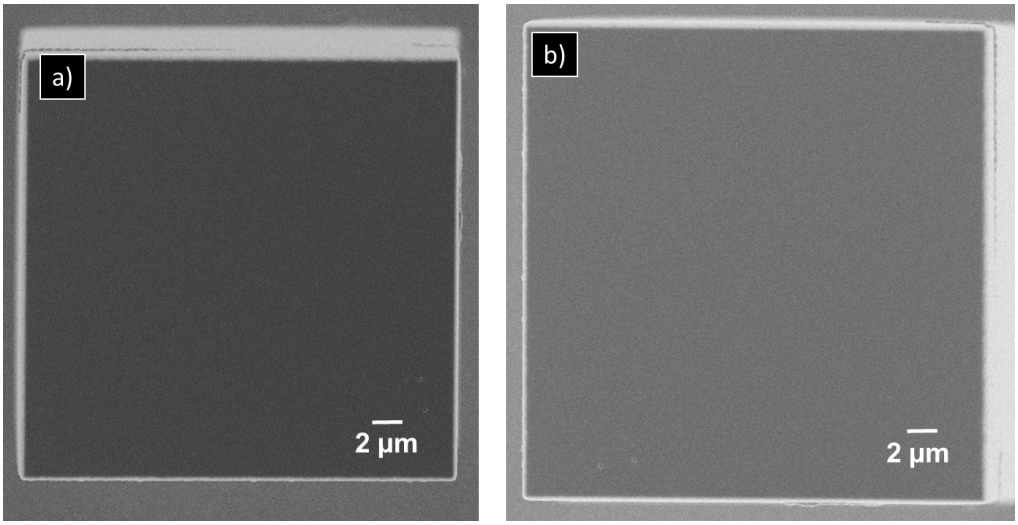

Figure 60. SEM images of the monolithic block fabricated in IP-Dip photoresist (a) unetched sample imaged after optical characterization, (b) sputter coated sample imaged after optical characterization.

The optical characterization was performed using the method described in section 4.5.3 and the optical setup shown in Fig. 38. A profile of the beam emanating from the output face was obtained from line scans. The line scans were measured by keeping the straight fiber ~5 µm from the sample in *x*- axis and moving the straight fiber in *y*- axis from +6 µm to -6 µm and scanning in *z*- axis from +15 µm to -15 µm at each point. Beyond +6 µm to -6 µm the signal diminished below the detection limit. Similar line scans were also measured for the metal coated sample. However, the metal coated sample was only scanned from +3 µm to -3 µm in the *y*- axis because beyond this range the signal reached the detection limit of the detector. Figure 61 shows the line scans of the light emanating from the unetched monolithic block and the metal coated monolithic block. Although the metal coated block was scanned from +3 µm to -3 µm in the *y*- axis, the contour plot in Fig. 61b was drawn from +6 µm to -6 µm to enable a direct comparison with the line scans of the unetched sample in Fig. 61a.

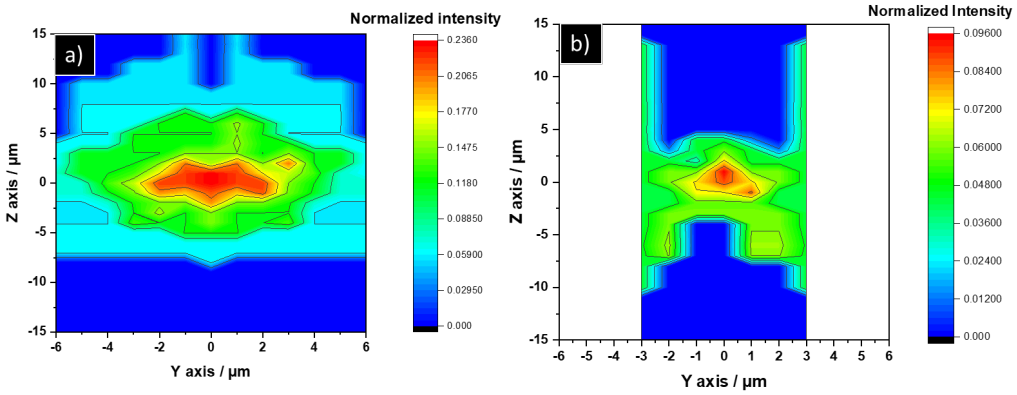

Figure 61. Line scans of the light emanating from the output face of the monolithic block measured by using AFS laser emitting λ_0 = 1.55 µm, a) line scans of the unetched structure measured by scanning the straight fiber from +6 µm to -6 µm in *y*-axis, b) line scans of the sputter coated sample measured by scanning the straight fiber from +3 µm to -3 µm in *y*- axis.

Table 8. Comparison between the FWHM and transmission efficiency of the beam exiting from the unetched and metal-coated sample shown in Figure 61 measured by using the output from an AFS laser, vertically polarized at λ_0 = 1.55 µm.

	FWHM / µm	**Transmission efficiency/ %**
Unetched sample	**8.43 ± 0.12**	**53.1 ± 1.46**
Metal-coated Sample	**4.82 ± 1.68**	**18.02 ± 1.90**

The FWHM and the transmission efficiency of the unetched and metal coated sample are shown in Table 8. The FWHM of the metal coated sample was reduced to half in magnitude when compared to the FWHM of the unetched sample. The change in the FWHM can be explained by comparing the line scans shown in Fig. 61. For the metal coated sample (Fig. 61b), the signal intensity was reduced to zero beyond the 3 µm range which resulted in smaller FWHM than the

unetched structure. The transmission efficiency of the unetched monolithic block and the metal coated monolithic block were also compared. The transmission efficiency of the unetched sample was 53%, which accounts for insertion and scattering losses at the input surface as well as absorption by the material. However, in the case of a metal coated sample, the transmission efficiency was reduced to 18%, which can be explained by enhanced losses due to high reflectivity of the source beam by the metal layer present at the entry face of the sample. Because, there was no change observed in the FWHM and transmission efficiency of the unetched and etched sample (Table 7), we can conclude that the ethaline-iodine solution is capable of completely etching the metal coating from the sample.

6.5 Conclusion

Au/Pd sputter-coated 3D microstructures were successfully etched using ethaline as the solvent and iodine as the oxidizing agent. The etched structure was re-imaged by SEM and characterized using the output beam from an AFS laser. The structural and optical properties of the etched sample were comparable to the unetched sample, which proved that etching did not affect the structural and optical integrity of the structure. The sputter-coated sample was exposed to the laser beam to detect if the sample will burn with laser exposure. But, due to the weak absorption of the laser beam by the metal coating at λ_0 = 1.55 μm, the metal coated structure sustained no damage. The optical characterization of the sputter coated sample with the AFS laser confirmed that due to strong reflection of the laser beam by the metal layer, the transmission efficiency was reduced to 18% compared to the 53% transmission efficiency of the unetched sample. These results confirmed that ethaline-iodine solvent is capable of completely etching a

sputter coated samples. Therefore, it is now possible to structurally characterize a sample, followed by optical characterization.

7. SUMMARY AND OUTLOOK

This dissertation explores possible sources of distortions that are possible in an in-house MPL system, and the steps involved in eliminating the distortions by creating a new MPL system. The structures fabricated in the new MPL system were not only free from distortions, they were fabricated with improved resolution, with an aspect ratio of 2.62, and improved repeatability in day-to-day fabrications.

3D SVPCs reported earlier[79] were designed to bend light through a 90 degree turn. The unit cells in the SVPC were spatially varied at an angle with each to bend the light via self-collimation. In this work, we fabricated curved waveguides and optically characterized to benchmark the performance of the SVPCs against conventional waveguides having a similar turn-radius. The bending radius of one of the waveguides similar to the 3D SVPC. The bending radius of the second waveguide was twice that of the first waveguide. A straight waveguide was also fabricated to account for insertion losses and absorption losses due to the material. The beam bending efficiency of the waveguides was measured using an Er:YAG laser at $\lambda_0 = 2.94$ μm. The beam bending in the waveguides suffered losses due to mode leakage along the sharp turns. Therefore, the beam bending observed in the waveguide was almost 90% smaller than the SVPC with comparable radius. These results provide further evidence that the SVPCs do not operate through total internal reflection, but rather through self-collimation, as designed.

SVPCs, which are capable of working in the telecommunication band, were fabricated in IP-Dip photoresist, and by scaling down the lattice spacing of $a = 1.05$ μm. Beam bending with almost 52% efficiency was measured in the SVPC having a 46% fill factor. To further explore the physics behind the beam bending, 3D ULPCs with lattice spacing similar to that of the SVPC were

fabricated in IP-Dip. The ULPCs were optically characterized by introducing a 1.55 μm beam onto the input face. The ULPCs were self-collimating only for vertically polarized light, and diverging for horizontally polarized light. These results were consistent with the polarization sensitive beam bending observed in the SVPCs. The self-collimation of the vertically polarized beam was independent of the fill factor. The fill factor dependent transmission efficiency of the ULPCs was also measured with respect to the vertically- and horizontally-polarized beams. The ULPC with 48% fill factor had the highest transmission efficiency of 80%. The transmission efficiency of the vertically polarized beam was highly sensitive to the fill factor. However, the transmission efficiency of the horizontally polarized beam was insensitive to the fill factor. These results show that a periodic lattice with lattice spacing of 1.05 μm is capable of self-collimating light with 80% transmission efficiency. An upper limit of the transmission efficiency by a periodic lattice has been realized, and the beam bending efficiency in the SVPC can be improved by optimizing the SVPC design and fabrication process.

The Au/Pd sputter coated samples were etched successfully using a deep eutectic solution of 1:2 (by moles) mixture of choline-chloride, and ethylene glycol with iodine was used as an oxidizing agent. The structures were successfully etched by using a 0.125 M iodine concentration. The structural and the optical integrity of the etched sample was maintained after the etching. The sputter coated sample was exposed to a laser beam to observe possible damage due to the strong absorption by the metals. However, the Au/Pd metal layer does not absorb sufficiently at 1.55 μm to result in damage to the structure. The optical characterization of the sputter coated sample with the AFS laser confirmed that due to strong reflection of the laser beam by the metal layer, the transmission efficiency was reduced to 18% compared to the 53% transmission efficiency of the

unetched sample. These results confirmed that ethaline-iodine solvent is capable of completely etching a sputter coated samples.

The results observed in this dissertation can be leveraged to extend studies into fabricating complex 3D structures with improved resolution and repeatability. The self-collimation of the vertically polarized beam in the ULPCs with a transmission efficiency of 80% indicate that by making required improvements in the design, SVPCs with beam bending efficiency > 52% can be fabricated.

The etching of Au/Pd sputter coated sample opens a new window into the experimental process. By using this method, a structure can be imaged by SEM first, and if the structure is made according to the desired specification, it will be characterized. Imaging the structures before characterization is not only an economic decision but it will also save time.

REFERENCES

1. Global data center IP traffic from 2012 to 2017, by data center type. http://www.statista.com/statistics/227268/global-data-center-ip-traffic-growth-by-data-center-type.
2. Top 500 list of supercomputer 2017. https://www.top500.org/statistics/perfdevel/.
3. Miller, D. A. B.; Ozaktas, H. M., Limit to the bit-rate capacity of electrical interconnects from the aspect ratio of the system architecture. *J Parallel Distrib Comput* **1997,** *41* (1), 42.
4. H. Ma; A. K. Y. Jen; Dalton, L. R., Polymer-based optical waveguides: Material processing and devices. *Adv. Mater.* **2002,** *14* (9), 1339.
5. Miller, D. A. B. In *Device requirements for optical interconnects to silicon chips*, Proc. IEEE, San Jose, CA, June, 10; IEEE: San Jose, CA, **2009**; pp 1166-1185.
6. Kubby, J. A.; Kimerling, L. C.; Reed, G. T.; Ahn, D.; Apsel, A. B.; Beals, M.; Carothers, D.; Chen, Y. K.; Conway, T.; Gill, D. M.; Grove, M.; Hong, C. Y.; Lipson, M.; Liu, J.; Michel, J.; Pan, D.; Patel, S. S.; Pomerene, A. T.; Rasras, M.; Sparacin, D. K.; Tu, K. Y.; White, A. E.; Wong, C. W. In *Electronic-photonic integrated circuits on the CMOS platform*, Integrated Optoelectronic Devices, San Jose, CA, March 1 - March 3; San Jose, CA, **2006**; p 612502.
7. Zortman, W. A.; Trotter, D. C.; Watts, M. R., Silicon photonics manufacturing. *Opt. Express* **2010,** *18* (23), 23598.

8. Lee, K. In *On-chip interconnects: giga hertz and beyond*, Proceedings of the IEEE 1998 International Interconnect Technology Conference (Cat. No.98EX102), June-3; **1998**; pp 15-17.

9. Brusberg, L.; Whalley, S.; Herbst, C.; Schröder, H., Display glass for low-loss and high-density optical interconnects in electro-optical circuit boards with eight optical layers. *Opt. Express* **2015,** *23* (25), 32528.

10. Urino, Y.; Usuki, T.; Fujikata, J.; Ishizaka, M.; Yamada, K.; Horikawa, T.; Nakamura, T.; Arakawa, Y., High-density and wide-bandwidth optical interconnects with silicon optical interposers [Invited]. *Photon. Res.* **2014,** *2* (3), A1.

11. Dikken, D. J.; Spasenović, M.; Verhagen, E.; van Oosten, D.; Kuipers, L., Characterization of bending losses for curved plasmonic nanowire waveguides. *Opt. Express* **2010,** *18* (15), 16112.

12. Bakir, B. B.; Gyves, A. V. d.; Orobtchouk, R.; Lyan, P.; Porzier, C.; Roman, A.; Fedeli, J. M., Low-Loss (<1 dB) and polarization-insensitive edge fiber couplers fabricated on 200-mm silicon-on-insulator wafers. *IEEE Photonics Technol. Lett.* **2010,** *22* (11), 739.

13. Goodman, J. W., Fan-in and fan-out with optical interconnections. *OPTICA ACTA* **1985,** *32* (12), 1489.

14. Rho, B. S.; Hwang, S. H.; Lim, J. W.; Kim, G. W.; Cho, C. H.; Lee, W. J., Intra-system optical interconnection module directly integrated on a polymeric optical waveguide. *Opt. Express* **2009,** *17* (3), 1215.

15. Monat, C.; Domachuk, P.; Eggleton, B. J., Integrated optofluidics: A new river of light. *Nat. Photonics* **2007,** *1*, 106.

16. Wojciechowski, J. R.; Shriver-Lake, L. C.; Yamaguchi, M. Y.; Füreder, E.; Pieler, R.; Schamesberger, M.; Winder, C.; Prall, H. J.; Sonnleitner, M.; Ligler, F. S., Organic photodiodes for biosensor miniaturization. *Anal. Chem.* **2009,** *81* (9), 3455.

17. Ligler, F. S.; Breimer, M.; Golden, J. P.; Nivens, D. A.; Dodson, J. P.; Green, T. M.; Haders, D. P.; Sadik, O. A., Integrating waveguide biosensor. *Anal. Chem.* **2002,** *74* (3), 713.

18. Rue, R. M. D. L.; Lahiri, B.; McMeekin, S. G.; Johnson, N. P. In *Nanophotonic structures for sensing: Exploiting photonic crystal and metamaterial concepts*, International Conference on Fiber Optics and Photonics (PHOTONICS), 9-12 Dec.; **2012**; pp 1-3.

19. Zhou, G., Lee, C. , *Optical MEMS, Nanophotonics, and their applications*. CRC Press.: Boca Raton, **2018**.

20. Naruse, M.; Miyazaki, T.; Kawazoe, T.; Sangu, S.; Kobayashi, K.; Kubota, F.; Ohtsu, M., Nanophotonic Computing Based on Optical Near-Field Interactions between Quantum Dots. *IEICE Trans. Electron.* **2005,** *E88C* (9), 1817.

21. Lu, Z.; Yin, P.; Shi, K. In *Bent Metal-Clad Waveguides for Fiber-to-Waveguide and 3D Chip-to-Chip Light Coupling Applications*, Frontiers in Optics Rochester, New York, Oct, 17; Optical Society of America: Rochester, New York, **2016**; p JTh2A.161.

22. Hattori, H. T.; Jagadish, C.; Seassal, C.; Boutami, S.; BenBhakir, B.; Drouard, E.; Letartre, X.; Viktorovitch, P. In *Integrated Photonic Crystal Devices for Optical Interconnect Applications (invited paper)*, International Conference on Mathematical Methods in Electromagnetic Theory, June, 26-29; **2006**; pp 35-40.

23. Digaum, J. L.; Pazos, J. J.; Chiles, J.; D'Archangel, J.; Padilla, G.; Tatulian, A.; Rumpf, R. C.; Fathpour, S.; Boreman, G. D.; Kuebler, S. M., Tight control of light beams in photonic crystals with spatially-variant lattice orientation. *Opt. Express* **2014,** *22* (21), 25788.

24. Madden, J. D.; Hunter, I. W., Three-dimensional microfabrication by localized electrochemical deposition. *J Microelectromech Syst* **1996,** *5* (1), 24.

25. Xia, Y.; Whitesides, G. M., Soft Lithography. *Angew. Chem. Int. Ed.* **1998,** *37* (5), 550.

26. Pease, R. F. W., Nanolithography and its prospects as a manufacturing technology. *J Vac Sci Technol B Microelectron Nanometer Struct Process Meas Phenom* **1992,** *10* (1), 278.

27. Nien, C.; Chang, L.-C.; Ye, J.-H.; Su, V.-C.; Wu, C.-H.; Kuan, C.-H., Proximity effect correction in electron-beam lithography based on computation of critical-development time with swarm intelligence. *J. Vac. Sci. Technol., B* **2017,** *35* (5), 051603.

28. Farsari, M. In *Multiphoton Lithography: Principles, Materials and Applications*, Conference on Lasers and Electro-Optics, San Jose, California, June-5; Optical Society of America: San Jose, California, **2016**; p SW4L.1.

29. Kodama, H., Automatic method for fabricating a three-dimensional plastic model with photo-hardening polymer. *Rev. Sci. Instrum.* **1981,** *52* (11), 1770.

30. Juodkazis, S.; Mizeikis, V.; Misawa, H., Three-dimensional microfabrication of materials by femtosecond lasers for photonics applications. *J. Appl. Phys.* **2009,** *106* (5), 051101.

31. Kawata, S.; Sun, H.-B.; Tanaka, T.; Takada, K., Finer features for functional microdevices. *Nature* **2001,** *412*, 697.

32. Shaw, J. M.; Gelorme, J. D.; LaBianca, N. C.; Conley, W. E.; Holmes, S. J., Negative photoresists for optical lithography. *IBM Journal of Research and Development* **1997,** *41* (1.2), 81.

33. Reichmanis, E.; Thompson, L. F., Polymer materials for microlithography. *Chem. Rev.* **1989,** *89* (6), 1273.

34. Dill, F. H.; Hornberger, W. P.; Hauge, P. S.; Shaw, J. M., Characterization of positive photoresist. IEEE Trans. Electron Devices **1975,** *22* (7), 445.

35. Elsner, C.; Dienelt, J.; Hirsch, D., 3D-microstructure replication processes using UV-curable acrylates. *Microelectron. Eng.* **2003,** *65* (1), 163.

36. Roy, D.; Basu, P. K.; Raghunathan, P.; Eswaran, S. V., DNQ–novolac photoresists revisited: 1H and 13C NMR evidence for a novel photoreaction mechanism. *Magn. Reson. Chem.* **2003,** *41* (2), 84.

37. Digaum, J. L. Fabrication and characterization of self-collimating spatially variant photonic crystals. University of Central Florida, 2016.

38. Göppert-Mayer, M., Über Elementarakte mit zwei Quantensprüngen. *Annalen der Physik* **1931,** *401* (3), 273.

39. Kaiser, W.; Garrett, C. G. B., Two-photoon excitaion in CaF_2: Eu^{2+}. *Phys. Rev. Lett.* **1961,** *7* (6), 229.

40. Williams, H. E.; Diaz, C.; Padilla, G.; Hernandez, F. E.; Kuebler, S. M., Order of multiphoton excitation of sulfonium photo-acid generators used in photoresists based on SU-8. *J. Appl. Phys.* **2017,** *121* (22), 223104.

41. Xiong, W.; Jiang, L. J.; Baldacchini, T.; Lu, Y. F., 9 - Laser additive manufacturing using nanofabrication by integrated two-photon polymerization and multiphoton ablation. In *Laser Additive Manufacturing*, Brandt, M., Ed. Woodhead Publishing: **2017;** pp 237-256.

42. Krause, S., Polymer Chemistry: An Introduction, 3rd Edition (Stevens, Malcolm P.). *J. Chem. Educ.* **2000,** *77* (1), 35.

43. Jenkins, A. D., *Contemporary polymer chemistry*. Third ed.; Pearson Education, Inc(Pearson/Prentice Hall): Upper Saddle River, NJ, USA, 2003., **2004**; Vol. 53, p 1395-1395.

44. P.C. Hiemenz, T. P. L., *Polymer Chemistry,*. second ed. ed.; CRC Press, New York: **2007**.

45. Hillmyer, M. A., *Polymer chemistry: An introduction*. Third ed.; Wiley-Blackwell: **2004**; Vol. 46, p 1900-1900.

46. Klikovits, N.; Knaack, P.; Bomze, D.; Krossing, I.; Liska, R., Novel photoacid generator for cationic photopolymerization. *Polym. Chem.* **2017,** *8*, 4414

47. Fischer, J.; von Freymann, G.; Wegener, M., The materials challenge in diffraction-unlimited direct-laser-writing optical lithography. *Adv. Mater.* **2010,** *22* (32), 3578.

48. Farsari, M.; Filippidis, G.; Sambani, K.; Drakakis, T. S.; Fotakis, C., Two-photon polymerization of an Eosin Y-sensitized acrylate composite. *J. Photochem. Photobiol., A* **2006,** *181* (1), 132.

49. Terzaki, K.; Vasilantonakis, N.; Gaidukeviciute, A.; Reinhardt, C.; Fotakis, C.; Vamvakaki, M.; Farsari, M., 3D conducting nanostructures fabricated using direct laser writing. *Opt. Mater. Express* **2011,** *1* (4), 586.

50. Obata, K.; El-Tamer, A.; Koch, L.; Hinze, U.; Chichkov, B. N., High-aspect 3D two-photon polymerization structuring with widened objective working range (WOW-2PP). *Light Sci. Appl.* **2013,** *2*, e116.

51. Lu, D.-X.; Zhang, Y.-L.; Han, D.-D.; Wang, H.; Xia, H.; Chen, Q.-D.; Ding, H.; Sun, H.-B., Solvent-tunable PDMS microlens fabricated by femtosecond laser direct writing. *J. Mater. Chem. C* **2015,** *3* (8), 1751.

52. Depre, L.; Ingram, M.; Poinsignon, C.; Popall, M., Proton conducting sulfon/sulfonamide functionalized materials based on inorganic–organic matrices. *Electrochim. Acta* **2000,** *45* (8), 1377.

53. 3D structuring in nanotechhnology. physikinstrumente.com/en/pdf_extra/Nano_Manufacturing_with_Piezo_Nanopositoning_System.

54. Mattei, T.; A Rehman, A., Technological developments and future perspectives on graphene-based metamaterials: A primer for neurosurgeons. *Neurosurgergy* **2014,** *74* (5), 499

55. Liu, R.; Ji, C.; Zhao, Z.; Zhou, T., Metamaterials: Reshape and Rethink. *Engineering* **2015,** *1* (2), 179.

56. Vladimir, P. B., Spontaneous emission from a medium with a band spectrum. *SJQE* **1975,** *4* (7), 861.

57. Yablonovitch, E., Inhibited Spontaneous Emission in Solid-State Physics and Electronics. *Phys. Rev. Lett.* **1987,** *58* (20), 2059.

58. Kawashima, S.; Ishizaki, K.; Noda, S., Light propagation in three-dimensional photonic crystals. *Opt. Express* **2010,** *18* (1), 386.

59. John D. Joannopoulos, S. G. J., Joshua N. Winn, Rober D. Measde, *Photonic Crystals Molding the flow of light*. Princeton University Press: **2007**.

60. Hecht, E.; Zając, A., *Optics*. Addison-Wesley Pub. Co.: **1974**.

61. Solli, D. R.; Hickmann, J. M., Photonic crystal based polarization control devices. *J. Phys. D* **2004,** *37* (24), R263.

62. Cregan, R. F.; Mangan, B. J.; Knight, J. C.; Birks, T. A.; Russell, P. S. J.; Roberts, P. J.; Allan, D. C., Single-Mode Photonic Band Gap Guidance of Light in Air. *Science* **1999,** *285* (5433), 1537.

63. Joannopoulos, J. D.; Villeneuve, P. R.; Fan, S., Photonic crystals: putting a new twist on light. *Nature* **1997,** *386*, 143.

64. Khan, K.; Mnaymneh, K.; Awad, H.; Hasan, I.; Hall, T., Optical wave propagation in photonic crystal metamaterials. *Applied Phys. A* **2014,** *117* (2), 629.

65. Yablonovitch, E., Photonic Crystals: Semiconductors of Light. *Scientific American* 2002, pp 47-51, 54.

66. Ozbay, E.; Michel, E.; Tuttle, G.; Biswas, R.; Sigalas, M.; Ho, K. M., Micromachined Millimeter Wave Photonic Band Gap Crystals. *Applied Phys. Lett.* **1994,** *64* (16), 2059.

67. Mark. S, *Quantum field theory*. Cambridge University Press: Cambridge, **2007**.

68. Gralak, B.; Enoch, S.; Tayeb, G., Anomalous refractive properties of photonic crystals. *J. Opt. Soc. Am. A* **2000,** *17* (6), 1012.

69. Kosaka, H.; Kawashima, T.; Tomita, A.; Notomi, M.; Tamamura, T.; Sato, T.; Kawakami, S., Self-collimating phenomena in photonic crystals. *Appl. Phys. Lett.* **1999,** *74* (9), 1212.

70. Witzens, J.; Loncar, M.; Scherer, A., Self-collimation in planar photonic crystals. In *IEEE J. Sel. Top. Quantum Electron.*, San Jose, California, Vol. 8, pp 1246-1257.

71. Rumpf, R., Engineering the Dispersion and Anisotropy of Periodic Electromagnetic Structures. In *Solid State Physics*, **2015;** Vol. 66, pp 213-300.

72. R. C. Rumpf, J. P., C. R. Garcia, L. Ochoa, and R. Wicker, 3D Printed Lattices with Spatially Variant Self-Collimation. *Prog. Electromagn. Res.* **2013,** *139*, 1.

73. Rumpf, R. C.; Pazos, J., Synthesis of spatially variant lattices. *Opt. Express* **2012,** *20* (14), 15263.

74. Rumpf, R. C.; Pazos, J., Synthesis of spatially variant lattices. *Opt. Express* **2012,** *20* (14), 15263.

75. Marcatili, E. A. J., Bends in Optical Dielectric Guides. *Bell System Technical Journal* **1969,** *48* (7), 2103.

76. Iliew, R.; Etrich, C.; Lederer, F., Self-collimation of light in three-dimensional photonic crystals. *Opt. Express* **2005,** *13* (18), 7076.

77. Datasheet; Nanoscribe photoresists. www.nanoscribe.de/files/1814/0662/4393/IP-Resist_IP-Dip_web.pdf.

78. Kowalevicz, M. A.; Bucholtz, F., Beam divergence from an SMF-28 optical fiber. Center, D. T. I., Ed. Washington DC, **2006**.

79. Digaum, J. L.; Pazos, J. J.; Chiles, J.; Archangel, J. D.; Padilla, G.; Tatulian, A.; Rumpf, R. C.; Fathpour, S.; Boreman, G. D.; Kuebler, S. M., Tight control of light beams in photonic crystals with spatially-variant lattice orientation. *Opt. Express* **2014,** *22* (21), 25788.

80. Zhang, Y.; Huang, T.; Jorgens, D. M.; Nickerson, A.; Lin, L.-J.; Pelz, J.; Gray, J. W.; López, C. S.; Nan, X., Quantitating morphological changes in biological samples during scanning electron microscopy sample preparation with correlative super-resolution microscopy. *PLOS ONE* **2017,** *12* (5), e0176839.

81. Velraj, G.; Tamilarasu, S.; Ramya, R., FTIR, XRD and SEM-EDS Studies of archaeological pottery samples from recently excavated site in Tamil Nadu, India. *Materials Today: Proceedings* **2015,** *2* (3), 934.

82. Taylor, M. E., Scanning Electron Microscopy in Forensic Science. *J Forensic Sci Soc* **1973,** *13* (4), 269.

83. Sim, K. S.; Tan, Y. Y.; Lai, M. A.; Tso, C. P.; Lim, W. K., Reducing scanning electron microscope charging by using exponential contrast stretching technique on post-processing images. *J. Microsc* **2010,** *238* (1), 44.

84. Oatley, C. W., The early history of the scanning electron microscope. *J. Appl. Phys.* **1982,** *53* (2), R1.

85. Hansen, H.; Jorgen Hansen, H., *A Technique for Removing Gold from Plated Calcareous Microfossils*. **1968**; Vol. 14, p 499.

86. Sela, J.; Boyde, A., Cyanide removal of gold from SEM specimens. *J. Microsc* **1977,** *111* (2), 229.

87. Crissman, R. S.; McCann, P., A technique to remove gold-palladium from SEM samples. *Micron (1969)* **1979,** *10* (1), 37.

88. Miller, C. G.; Cornish, L.; Jones, C.; Jones, C. G.; Henderson, A. S., A new laser method for cleaning micropalaeontological specimens. *MICROPALEONTOLOGY* **2004,** *23* (2), 165.

89. Leslie, S.; Mitchell, J., Removing gold coating from SEM samples. *Paleontology* **2007,** *50* (5), 1459.

90. Jones, D., Hartley, Jennifer, Frisch, Gero, Purnell, Mark, and Darras, Laurent, Non-destructive, safe removal of conductive metal coatings from fossils: a new solution. *Palaeontol Electronica* **2012,** *15* (2).

91. Zhang, Z.; Song, J.; Han, B., Catalytic Transformation of Lignocellulose into Chemicals and Fuel Products in Ionic Liquids. *Chem. Rev.* **2017,** *117* (10), 6834.

92. Abbott, A. P.; Frisch, G.; Hartley, J.; Ryder, K. S., Processing of metals and metal oxides using ionic liquids. *Green Chem.* **2011,** *13* (3), 471.

93. J. Digaum, S. M. K., **2016**.

94. Raut, R.; Sana, A.; Malghe, Y.; T Nikam, B.; Sahebrao, K., Rapid biosynthesis of platinum and palladium metal nanoparticles using root extract of Asparagus racemosus Linn. *Adv. Mater. Lett.* **2013,** *4* (8), 650.

95. Reznickova, A.; Novotna, Z.; Kasalkova, N. S.; Svorcik, V., Gold nanoparticles deposited on glass: physicochemical characterization and cytocompatibility. *Nanoscale Res. Lett.* **2013,** *8* (1), 252.